J. Phys. Chem. A

Gas-Phase Binding Energies and Dissociation Dynamics of 1-Alkyl-3-Methylimidazolium Tetrafluoroborate Ionic Liquid Clusters

H. A. Roy, L. A. Hamlow, and M. T. Rodgers*

Department of Chemistry, Wayne State University, Detroit, MI, 48202, USA

ABSTRACT:

Ionic liquids (ILs) have become increasingly popular due to their useful and unique properties, yet there are still many unanswered questions regarding their fundamental interactions. In particular, details regarding the nature and strength of the intrinsic cation-anion interactions, and how they influence the macroscopic properties of ILs are still largely unknown. Elucidating the molecular-level details of these interactions is essential to the development of better models for describing ILs and enabling the purposeful design of ILs with properties tailored for specific applications. Current uses of ILs are widespread and diverse, and include applications for energy storage, electrochemistry, designer/green solvents, separations, and space propulsion. To advance the understanding of the energetics, conformations, and dynamics of gas-phase IL clustering relevant to space propulsion, threshold collision-induced dissociation approaches are used to measure the bond dissociation energies (BDEs) of the 2:1 clusters of 1-alkyl-3-methylimidazolium cations and tetrafluoroborate, $[2C_nmim{:}BF_4]^+$. The cation, $[C_nmim]^+$, is varied across the series, 1-ethyl-3-methylimidazolium $[C_2mim]^+$, 1-butyl-3-methylimidazolium $[C_4mim]^+$, 1-hexyl-3-methylimidazolium $[C_6mim]^+$, and 1-octyl-3-methylimidazolium $[C_8mim]^+$, to examine the structural and energetics effects of the size of the 1-alkyl substituent on the binding. Complementary electronic structure calculations are performed to determine the structures and energetics of the $[C_nmim]^+$ and $[BF_4]^-$ ions and their binding preferences in the $(C_nmim{:}BF_4)$ ion pairs and $[2C_nmim{:}BF_4]^+$ clusters. Several levels of theory, B3LYP, B3LYP-GD3BJ, and M06-2X, using the 6-311+G(d,p) basis set for geometry optimizations and frequency analyses and the 6-311+G(2d,2p) basis set for energetics, are benchmarked to examine their abilities to properly describe the nature of the binding interactions and to reproduce the measured BDEs. The modest structural variation among these $[C_nmim]^+$ cations produces only minor structural changes and variation in the measured BDEs of the $[2C_nmim{:}BF_4]^+$ clusters. Present findings indicate that the dominant cation-anion interactions involve the 3-methylimidazolium moieties and that these clusters are sufficiently small that differences in packing effects associated with the variable length of the 1-alkyl substituents are not yet significant.

Corresponding author: M. T. Rodgers, mrodgers@chem.wayne.edu, Tel. (313)577-2431

INTRODUCTION

Traditional salts such as sodium chloride have high melting points due to strong intermolecular interactions (ionic bonding) and their ability to form highly-ordered lattice structures. An alternative type of salt was discovered in 1914 by Walden[1] with the production of ethylammonium nitrate, $C_2H_5NH_3$-NO_3. These alternative salts have been described as ionic liquids (ILs) as they exhibit low melting point (mp) temperatures, with an arbitrary cutoff of being near or below 100°C. The low melting temperatures of ILs arise from several factors including: ion asymmetry, charge delocalization, ion interaction strength, conformational degrees of freedom, ion size, and ion packing.[2]

Another major factor that determines the melting point of a salt is the lattice energy of the solid, where the more stable the lattice the higher the mp. A variety of intermolecular forces contribute to lattice stability including: electrostatic interactions, dipole-dipole interactions, hydrogen-bonding interactions, and London-type (dispersion) interactions. Optimization of these forces results in lowering of the overall potential energy of the lattice structure. The addition of cations and anions to a simple ion pair may result in rearrangement of the binding structure, i.e., packing effects. Such structural rearrangements may sacrifice a strong interaction for multiple weaker interactions that cumulatively reduce the overall lattice energy of the material.

The observable properties of ILs are tunable due to the vast diversity of cations and anions from which they are comprised. The cations of interest in this work include a series of 1-alkyl-3-methylimidazolium cations, $[C_nmim]^+$ as shown in **Figure 1**. The planar 3-methylimidazolium moiety is common to all four cations, whereas the 1-alkyl chain varies in length. The aromaticity of imidazolium ring facilitates delocalization of the positive charge thereby weakening the Lewis acid character of the cation, which contributes to the low mps of alkylimidazolium-based salts. In the work performed here, the length of the 1-alkyl substituent is systematically varied from an ethyl to an octyl substituent such that the cations examined include: 1-ethyl-3-methylimidazolium, $[C_2mim]^+$, 1-butyl-3-methylimidazolium, $[C_4mim]^+$, 1-hexyl-3-methylimidazolium, $[C_6mim]^+$, and 1-octyl-3-methylimidazolium, $[C_8mim]^+$. Melting

temperatures reported by López-Martin et al.[3] for the 1-alkyl-3-methylimidazolium tetrafluoroborate ILs examined in this work are as follows: C_2mim-BF_4 (11 °C), C_4mim-BF_4 (−71 °C), C_6mim-BF_4 (−82 °C), and C_8mim-BF_4 (−88 °C). The length of the 1-alkyl substituent clearly impacts the mps of these $C_n$mim-BF_4 ionic liquids. The overall trends in the mps of the $C_n$mim-BF_4 ILs exhibit interesting packing effects. The mps of $C_n$mim-BF_4 ILs involving both long and short chain species are significantly greater (≥ −25 °C when n = 1–3 and 10–18) than those involving intermediate chain species (~ −85 °C when n = 4–9). The trend in the mps of these ILs is attributed to the specific nature of the cation-anion packing. The cations and anions of the C_1mim-BF_4 IL are best size matched such that more highly ordered packing can be achieved, and as a result, this IL exhibits the greatest mp among the $C_n$mim-BF_4 ILs. The mp initially falls off with increasing length of the 1-alkyl substituent, i.e., with increasing n, due to the increase in cation-anion size mismatch. However as the size of the 1-alkyl substituent continues to increase, dispersion interactions between the 1-alkyl chains of the cations provide additional stabilization. As a result, the mps level off for intermediate values of n, and then increase with further increases in n as a result of these competing effects.

ILs are widely applicable to energy storage,[4-6] electrochemistry,[7,8] designer/green solvents,[9-11] separations,[12-15] and space propulsion.[16-18] Applications of ILs as propellants for spacecraft involve multiple types of propulsion: electrical, chemical/thermal, and dual mode. The electric propulsion mode is generally of high efficiency at the cost of thrust, chemical/thermal propulsion generally produces greater thrust at lower efficiency, whereas dual mode propulsion enables operation in either mode depending on conditions. Chemical space propulsion by ILs involves the replacement of traditional fuels or oxidizers with an energetic IL for the use in monopropellant or bipropellant systems.[19,20] Electric propulsion uses ion thrusters where the ions are generated via a mechanism very much like electrospray ionization (ESI). Being composed of ions makes ion generation from ILs rather facile versus that in a neutral propellant. Moreover, the low vapor pressures of ILs increase propulsion efficiency by preventing excess sample losses in the low-pressure environment of outer space. Ion generation and thrust are controlled via the

application of high voltage to the IL emitters, which can be bipolar or of a single polarity. In the bipolar mode, the polarity of the high voltage is alternated between negative and positive values to alternately induce emission of positive and negative ions/clusters to maintain charge neutrality of the spacecraft, while minimizing charging effects at the ESI emitters.[21] The high voltage applied can also be of a single polarity such as that used for the NASA/ESA LISA Pathfinder mission in which the IL fuel,1-ethyl-3-methylimidazolium bis(trifluoromethylsulfonyl)imide, C_2mim-Tf_2N, was employed under conditions that emit only cations.[22] Propulsion is achieved via acceleration of charged particles away from the spacecraft by the application of an electric field.

Both the thermochemical and electrochemical properties of an IL impact its performance as a propellant, particularly the efficiency and thrust.[18,23] Thermochemical properties that are of particular importance include the melting temperature, density, viscosity, and heat of formation. Electrochemical properties of importance include surface tension and electrical conductivity. Low melting temperatures minimize the amount of energy required to keep the propellant in the liquid state. High densities minimize the space required for storage, or conversely, the payload of the propellant that can be stored on a given spacecraft. Low viscosity allows the propellant to experience minimal drag as it flows to the ESI emitter. A large heat of formation increases combustion temperatures and provides higher thrust for dual-mode propellants. Surface tension and electrical conductivity influence the efficiency of ESI ionization and the generation of charged IL clusters for a high efficiency thrust versus submicron-sized droplets resulting in higher thrust at the sacrifice of efficiency.

Although ILs have been widely studied, our current understanding of the details regarding the fundamental interactions that occur in ILs leave many unanswered questions such as: How do the ion-pairs interact? How strong are the intrinsic ion-pairing interactions? How are the intrinsic ion-pairing interactions influenced by nearby ions? How does the balance of the local and longer-range ion-ion interactions affect the structure and observable properties? The answers to these questions must clearly depend on the identities of the cations and anions that comprise the IL. In regard to space propulsion in particular, how are thrust and efficiency

affected by the selection of the specific cations and anions that comprise the IL? Answering these questions is essential to the development of better models to describe ILs and the design of improved task-specific ILs. To begin to answer these questions, fundamental studies have probed ILs and provided experimental data to aid in modeling ILs. Databases that compile thermodynamic information about ILs such as the ILThermo database[24] have been established, but still contain very limited information. Therefore, additional thermodynamic data for ILs is both desired and necessary. IR spectroscopy of solvated clusters of the $[C_4mim]^+$ cation has also been performed to elucidate the effects of solvation of ionic liquid cations in water.[25] Mass spectrometry (MS) and ion mobility spectrometry (IMS) have been powerful tools for elucidating structure and examining the reactivity and reaction dynamics of IL clusters.[26] Energy-resolved collision-induced dissociation (ER-CID) experiments have been performed to elucidate the gas-phase energetics and dissociation mechanisms of aprotic and protic ionic liquids for applications in space propulsion[27-29] and to elucidate relative affinities of various cations and anions that comprise common ILs.[30-33] IMS experiments have investigated the formation of IL clusters, IL cluster distributions and magic number clusters, and ion evaporation processes that occur during the ESI process.[34-36] For example, IL clusters of the $[5C:4A]^+$ stoichiometry exhibit high stability, i.e., are magic number clusters, for at least two ILs.[31,34] Further, in addition to single ion-pair losses (C:A) upon dissociation, simultaneous loss of clusters involving multiple ion pairs, $(C:A)_n$, have been reported for select IL clusters.[35,37]

Structural insight into imidazolium-based ionic liquids has been obtained through spectroscopic measurements combined with computational methods.[25,38-46] Computational work has primarily focused on characterization of the cation-anion interactions in isolated ion pairs, whereas experimental studies have examined clusters of various size as well as liquids. Computational studies of ($C_2mim:BF_4$) and ($C_4mim:BF_4$) ion pairs have found a preference for front-side binding and established the importance of the C2 hydrogen atom in the binding.[43-46] The C1′ and C1″ hydrogen atoms have also been suggested to enhance the binding, but their contribution has not been a significant focus.[43-44] Infrared (IR) and Raman spectroscopy studies

have been performed for various clusters of C_2mim-BF_4, C_3mim-BF_4, and C_4mim-BF_4 ILs indicating the importance of the C2 hydrogen atom to the binding and revealing minimal structural change among the smaller ILs.[29,38,39,42-44,46] Johnson and coworkers investigated the isolated cations and 2:1 clusters of C_2mim-BF_4 and C_2dmim-BF_4 (C_2dmim = 1-ethyl-2,3-dimethylimidazolium) using cryogenic ion vibrational spectroscopy.[38,39] Both deuteration and methylation at the C2 position were employed to definitively establish the importance of the C2 hydrogen atom in the binding of $C_n$mim-BF_4 ILs. The observed vibrational frequency of the C2-H stretch provides a signature for noncovalent interactions such as hydrogen bonding or an electrostatic interaction. Seemingly small changes in the cation or anion can lead to large changes in the observable properties of ILs. For example, methylation at the C2 position of the imidazolium ring leads to large changes in viscosity and mps,[47-50] likewise variation in the length of the 1-alkyl substituent of $C_n$mim-BF_4 ILs also produces large changes in the mps.[3]

This work seeks to understand how variation of the $[C_n\text{mim}]^+$ cation affects the structures and the strength of binding in $[2C_n\text{mim:}BF_4]^+$ IL clusters in the gas phase. The bond dissociation energies (BDEs) of $[2C_n\text{mim:}BF_4]^+$ clusters, where $[C_n\text{mim}]^+$ and n = 2, 4, 6, and 8, are determined from threshold analyses of experimentally measured cross sections for collision-induced dissociation (CID) of these complexes performed under nominally single collision conditions and as a function of collision energy, generally referred to as the threshold collision-induced dissociation (TCID) technique. Electronic structure calculations are performed to provide molecular-level details regarding the structures and energetics of the $[C_n\text{mim}]^+$ and $[BF_4]^-$ ions and their binding preferences in the ($C_n$mim:BF_4) ion pairs and $[2C_n\text{mim:}BF_4]^+$ clusters. Further, these calculations provide the molecular parameters needed for threshold analyses of the CID cross sections. Several density functional theories (DFT) are explored including B3LYP,[51,52] B3LYP-GD3BJ including empirical dispersion,[53] and the Minnesota functional, M06-2X, a highly parameterized approximate exchange-correlation energy functional that has been developed by the Truhlar group.[54] The BDEs extracted from the threshold analyses

are compared to those derived from the theoretical models examined to determine which levels of theory are able to provide robust and practical energetic predictions for these systems.

EXPERIMENTAL AND COMPUTATIONAL METHODS

Sample Preparation. Materials were purchased from commercial vendors and used as received. HPLC grade methanol was purchased from Fisher Scientific (Waltham, MA, USA). HPLC grade water, 1-ethyl-3-methylimidazolium tetrafluoroborate C_2mim-BF_4, and 1-hexyl-3-methylimidazolium bis(trifluoromethylsulfonyl)imide, C_6mim-Tf_2N, were purchased from Sigma Aldrich (St. Louis, MO, USA). 1-Butyl-3-methylimidazolium tetrafluoroborate, C_4mim-BF_4, and 1-octyl-3-methylimidazolium bis(trifluoromethylsulfonyl)imide, C_8mim-Tf_2N, were purchased from Alfa Aesar (Haverhill, MA, USA). Solutions of the desired ILs were prepared via dilution of the pure IL or by mixing two ILs, one containing the desired cation, and the other the anion. C_2mim-BF_4 and C_4mim-BF_4 were simply diluted to working concentration to generate the $[2C_2mim{:}BF_4]^+$ and $[2C_4mim{:}BF_4]^+$ clusters, respectively. C_2mim-BF_4 was mixed with C_6mim-Tf_2N or C_8mim-Tf_2N and diluted to working concentration to generate the $[2C_6mim{:}BF_4]^+$ and $[2C_8mim{:}BF_4]^+$ clusters, respectively. The working solutions of the ILs were prepared at concentrations of ~ 0.5 mM in 50/50 methanol/water (v/v) for introduction to the ESI interface of the instrument.

Experimental Procedures. TCID experiments were performed for four $[2C_nmim{:}BF_4]^+$ IL clusters using a custom-built guided ion beam tandem mass spectrometer (GIBMS)[55] of the BoQ geometry (magnetic sector - rf octopole ion guide - quadrupole mass filter) equipped with an ESI source,[56,57] that has been described in detail previously. Briefly, IL solutions were infused via a mechanical syringe pump at a flow rate of ~ 1.2 μL/min through a 35 gauge stainless steel ESI emitter held at ~ +2 kV. Ions were transferred to the first stage of differential pumping via a heated capillary inlet operated at ~ 100 °C and biased at ~ 25 V_{dc}, generating pressures in the source region of ~ 100 mTorr. The ions exiting the heated capillary enter an rf ion funnel operated at ~ 530 kHz and ~ 25 V_{pp}, with a dc gradient of ~ 25 V_{dc}. Ions emanating from the rf ion funnel were injected into a 6”-long rf hexapole ion guide operated at ~ 1.58 MHz and

~ 90 V_{pp} that spans a differentially pumped chamber where the precursor IL clusters were thermalized by > 10^4 collisions with the background gases. Ions were extracted from the hexapole ion guide using dc focusing lenses and shaped and accelerated for momentum analysis by a magnetic sector for mass selection of the precursor ion. The mass-selected ion beam was reshaped and then slowed to a nominal kinetic energy using an exponential retarder. The precursor ions were then focused into an rf octopole ion guide[58,59] that traps the ions in the radial direction. The octopole ion guide[58,59] passes through a collision cell containing xenon at sufficiently low pressure (i.e., ~ 0.05–0.20 mTorr) that CID occurs under nominally single-collision conditions. Remaining precursor ions and resulting product ions drift to the end of the octopole ion guide, are focused into a quadrupole mass filter for mass analysis, and then detected using a Daly detector[60] with standard pulse-counting electronics.

Theoretical Calculations. Theoretical calculations were performed to elucidate molecular-level details regarding the structures and energetics of the $[C_nmim]^+$ and $[BF_4]^-$ ions and their binding preferences in the ($C_nmim:BF_4$) ion pairs and $[2C_nmim:BF_4]^+$ clusters. Initially, molecular mechanics simulations were performed in HyperChem[63] using the Amber 3 force field and a simulated annealing procedure[64] to generate candidate structures for high-level electronic structure calculations. The Amber force field partitions the energy of the system into covalent terms including: bond stretching, angle bending, and torsions, and noncovalent terms including: van der Waals and electrostatic interactions.[65,66] The default parameterization and atom types available in the HyperChem suite of programs were used.[63] For the simulations involving the ($C_nmim:BF_4$) ion pairs and $[2C_nmim:BF_4]^+$ clusters, the cations and anions were constrained to the coordinate origin to prevent dissociation from occurring during the annealing process. The value of the constraint used was empirically derived and kept to a minimum while providing adequate sampling of conformational space. The specific value chosen (0.01 kcal/mol·Å^2) enabled the cation(s) and anion to undergo vibrational oscillations during the simulated annealing procedure that increased the cation-anion intermolecular distances by as much as a factor of five, which enabled the cation(s) to unfold as the ions moved apart and refold around

the anion as they were drawn back together. During the simulated annealing procedures, 300 cycles of heating, molecular dynamics sampling of conformational space, and cooling, were performed. In each cycle, the temperature was linearly ramped up from 0 K to 1000 K over a period of 0.3 ps, the temperature was maintained at 1000 K for 0.2 ps during sampling of conformational space, and the temperature was linearly ramped down from 1000 K to 0 K over another 0.3 ps. It should be noted that the asymmetry of the $[C_nmim]^+$ cations leads to enantiomeric structures for the isolated cations as well as their ion pairs and 2:1 clusters to $[BF_4]^-$. We did not concern ourselves with this issue as the 1000 K simulated annealing temperature provided sufficient internal energy to the systems to enable interconversion of enantiomeric structures. Candidate structures were sorted by energy (and geometry) and a combination of low-energy structures, along with additional manually-selected structures exhibiting complementary geometries (to ensure comprehensive sampling of conformational space), were submitted to further quantum mechanics calculations. Initially 20–40 unique conformations were included in the high-level calculations for each $[C_nmim]^+$ cation, ($C_nmim:BF_4$) ion pair and $[2C_nmim:BF_4]^+$ cluster examined. However, to ensure reasonable sampling of the possible binding modes and 1-alkyl conformations available to these systems the simulated annealing procedures were repeated multiple times using different initial structures and 20–40 unique conformations were included in the high-level calculations for each cycle performed.

The Gaussian 09 suite of programs[67] was used for the electronic structure calculations. Geometry optimizations and frequency analyses were performed for the $[C_nmim]^+$ and $[BF_4]^-$ ions, ($C_nmim:BF_4$) ion pairs, and $[2C_nmim:BF_4]^+$ clusters using several density functional theory methods including: B3LYP, B3LYP-GD3BJ, and M06-2X each with a 6-311+G(d,p) basis set. B3LYP was chosen as it is the most commonly employed density functional and its strengths and limitations are probably best known.[51,52,68,69] B3LYP-GD3BJ was also included as B3LYP does not include dispersion,[53] and dispersion interactions are likely important contributors to the folding of the 1-alkyl substituent of the $[C_nmim]^+$ cations, and the binding in the ($C_nmim:BF_4$)

ion pairs and $[2C_nmim:BF_4]^+$ clusters. The M06-2X functional was chosen as it has been found to describe noncovalent interactions well, particularly for ionic species comprised of main group elements.[54] Single point energies were calculated using the same theoretical model/density functional but with a larger basis set, 6-311+G(2d,2p), to improve energetic predictions. Basis set superposition error (BSSE)[70,71] and zero point energy (ZPE) corrections were included for all levels of theory. Thermal corrections to 298 K enthalpies and relative Gibbs energies were also performed using the computed frequencies.

Approximately ~ 3500 high-level calculations in total were performed that produced ~2450 "unique" stable conformations of the $[C_nmim]^+$ cations, ($C_nmim:BF_4$) ion pairs, and $[2C_nmim:BF_4]^+$ clusters. B3LYP was most comprehensively investigated accounting for ~1500 of the calculations and ~900 of the "unique" conformers found. B3LYP-GD3BJ was next most comprehensively examined accounting for ~1100 of the calculations and ~900 of the "unique" structures determined. As the most time consuming of the three approaches, M06-2X calculations were limited to ~900 in total and produced ~650 of the "unique" conformers found. Most of the structures subjected to high-level optimization were taken directly from the simulated annealing procedures. However, in cases where a given type of structure was not found across the entire cation series, structures were manually manipulated in an attempt to find parallel structures across the cation series. Candidate structures were typically optimized at the B3LYP level of theory first, and then a selection of the "unique" structures found was re-optimized at the B3LYP-GD3BJ and M06-2X levels. Note that if more than one of the density functionals found the "same" structure, that conformer was counted more than once in the number of "unique" structures reported above. To minimize bias in the results arising from the functional chosen for initial optimization, some of the candidate structures were optimized via B3LYP-GD3BJ first and then re-optimized at the B3LYP and M06-2X levels. The latter approach was more effective for finding "unique" M06-2X structures than from structures initially optimized via B3LYP such that roughly three quarters of the M06-2X calculations used the latter approach. To further limit the number of M06-2X calculations, only structures within

20 kJ/mol of the ground conformer (at the initial level of optimization) were examined for systems involving the two largest cations. To overcome convergence problems encountered during geometry optimization and frequency analyses of some of the M06-2X calculations, an ultrafine integration grid was used. In cases where such an ultrafine integration grid was necessary, the values are reported with an asterisk.

Isotropic molecular polarizabilities of the B3LYP/6-311+G(d,p) ground conformers of the ($C_n$mim:BF_4) ion pairs were calculated at the PBE1PBE/6-311+G(2d,2p) level of theory as they are needed for the thermochemical analysis of the CID cross sections, and this level of theory has previously been shown to accurately predict molecular polarizabilities of neutral polyatomic molecules and their cations.[72] As polarizabilities can also be extracted directly from the geometry optimizations without the additional PBE1PBE/6-311+G(2d,2p) step, the B3LYP/6-311+G(d,p) polarizabilities of the ground conformers of the $[C_n\text{mim}]^+$ cations, $[BF_4]^-$ anion, ($C_n$mim:BF_4) ion pairs and $[2C_n\text{mim}:BF_4]^+$ clusters as well as polarizability values for all stable conformers of the ($C_n$mim:BF_4) ion pairs were also examined to evaluate the ability of this level of theory to accurately predict the molecular polarizabilities of these systems, and to examined the sensitivity of our thermochemical analyses to the exact polarizability values used in the analysis.

Electrostatic potential (ESP) maps were also computed for the B3LYP and M06-2X optimized geometries of the ground conformers of the $[C_n\text{mim}]^+$ and $[BF_4]^-$ ions, ($C_n$mim:BF_4) ion pairs, and $[2C_n\text{mim}:BF_4]^+$ clusters. These ESP maps are used to visualize the favorable interaction sites of the $[C_n\text{mim}]^+$ cations and $[BF_4]^-$ anion, and how they are influenced by the intrinsic binding interactions in the 1:1 neutral ion pairs and 2:1 cationic clusters. All ESP maps were generated using the associated density functional with a 6-311+G(2d,2p) basis set. ESP maps of the B3LYP ground conformers were also computed at the PBE1PBE /6-311+G(2d,2p) level of theory. The ESP maps visualized in this work are shown at an isosurface of 0.01 a.u. of the total SCF electron density. The Mülliken charges on the hydrogen atoms of the $[C_n\text{mim}]^+$ cations and the fluorine atoms of the $[BF_4]^-$ anion are labeled. The most electropositive regions

are color-coded in blue, whereas the most electronegative regions are color-coded in red, as shown in the colorbar of the figures in which the ESP maps are displayed.

Noncovalent interactions (i.e., hydrogen bonding, H-π interactions, dipole-dipole interactions, London dispersion, and steric repulsions) within the B3LYP and M06-2X ground conformers of the $[C_nmim]^+$ cations, $[BF_4]^-$ anion, ($C_nmim:BF_4$) ion pairs, and $[2C_nmim:BF_4]^+$ clusters were visualized as electron density gradient isosurfaces or noncovalent interaction (NCI) maps using the NCIPLOT method described previously by Yang and coworkers[73,74] and Visual Molecular Dynamics software.[75]All NCI maps are shown at an isosurface of 0.20 au of the reduced electron density gradient computed using the B3LYP or M06-2X density functional with a 6-311+G(2d,2p) basis set and color-coded based on the strength of the noncovalent interactions. The regions exhibiting strong attractive interactions such as hydrogen-bonding interactions are shaded in blue, weaker attractive interactions such as those associated with dispersion are shaded in green, and highly repulsive interactions are shaded in red.

Thermochemical Analysis. Precursor and product ion intensities are monitored as a function of collision energy and pressure, and converted to energy-dependent CID cross sections using the Beer's law relationship described by eq 1,

$$I = I_0 \exp(-\sigma_{tot}\, \rho l) \quad (1)$$

where the variables are defined as the measured intensity of the precursor ion (I), the measured total ion intensity i.e., the sum of the precursor and product ion intensities (I_0), total CID cross section (σ_{tot}), neutral collision gas density (ρ), and effective interaction path length (l). The collision energy in the reaction cell is determined by the dc offset applied to the octopole ion guide. The zero of the ion kinetic energy is determined from a retarding analysis performed in the octopole ion guide, where the dc offset in the octopole is scanned and the resulting precursor ion kinetic energy distribution is measured and fitted with a Gaussian distribution, as described previously.[76] The full width at half-maximum (fwhm) of the ion kinetic energy distribution is 0.3–0.4 eV in the laboratory frame for the $[2C_nmim:BF_4]^+$ IL clusters measured here. Energies in

the laboratory frame (E_{lab}) are converted to the center-of-mass frame energies (E_{cm}) using the relationship of eq 2,

$$E_{cm} = E_{lab}\{m/(m+M)\} \quad (2)$$

where m is the mass of Xe the neutral collision gas and M is the mass of the $[2C_nmim{:}BF_4]^+$ precursor ion. Pressure-dependent studies were performed because the effects of multiple collisions can impact the shape of CID cross sections and shift the apparent threshold to lower collision energies.[77] Cross sections were measured at three nominal pressures of ~ 0.20, 0.10, and 0.05 mTorr and pressure extrapolated to zero pressure, corresponding to rigorously single-collision conditions.

The procedures employed for fitting the pressure-extrapolated CID cross sections have been discussed in detail previously.[55,62,78] Briefly, thresholds were determined via fitting with an empirical threshold law of the form shown in eq 3,

$$\sigma(E) = \sigma_0 \sum_i g_i(E+E_i-E_0)^n/E \quad (3)$$

where σ_0 is an energy-independent scaling factor, E is the relative translational energy of the $[2C_nmim{:}BF_4]^+$ and Xe reactants, E_0 is the threshold for dissociation of the ground electronic and ro-vibrational state of $[2C_nmim{:}BF_4]^+$, and n is an adjustable parameter that describes the efficiency of kinetic-to-internal energy transfer in the collision. The summation is over the ro-vibrational states of the reactants i, where E_i is the excitation energy of each state and g_i are the populations of those states ($\Sigma_i\, g_i = 1$). The Beyer-Swinehart algorithm[79] is used to evaluate the density of the ro-vibrational states. The relative populations, g_i, were calculated for a Maxwell-Boltzmann distribution at 298 K of the precursor $[2C_nmim{:}BF_4]^+$ IL cluster, which should be appropriate given the gentle sampling into the rf ion funnel and thermalization of the ions in the hexapole ion guide. When used for fitting procedures, the vibrational frequencies computed at the B3LYP/6-311+G(d,p) level of theory were first scaled by a factor of 0.9887.[80] Vibrational frequencies computed at the B3LYP-GD3BJ/6-311+G(d,p) and M06-2X/6-311+G(d,p) levels of theory were used without scaling. Lifetime effects were incorporated into eq 3 using Rice-Ramsperger-Kassel-Marcus (RRKM) theory. RRKM theory

allows dissociation not occurring on the timescale of the experiment (~ 10^{-4} s) to be accounted and corrected for and has been discussed in depth previously.[61,62] The model is convoluted with the kinetic and internal energy distributions of the $[2C_nmim{:}BF_4]^+$ and Xe reactants, and values of σ_0, E_0, and n are optimized via nonlinear least-squares regression.

The error in the threshold energy determined includes variances associated with analyses of multiple datasets and uncertainties related to the calculated frequencies, RRKM lifetime effects, and the error in the absolute energy scale. Uncertainties in the calculated frequencies were estimated by scaling the predicted frequencies by ±10%. We also examined the effects of additional scaling of the low-frequency modes as these modes are often not predicted as accurately, but found that the best fits were achieved for the $[2C_nmim{:}BF_4]^+$ clusters when all frequencies were treated in the same fashion. Uncertainties associated with RRKM lifetime effects were estimated by increasing and decreasing the time assumed available for dissociation by a factor of two. The absolute energy scale has an uncertainty of ±0.05 eV in the laboratory frame (as limited by the root mean square deviation in the voltage output by the octopole dc power supply, V_{rms}), corresponding to an uncertainty of approximately ±0.02 eV in center-of-mass frame for the systems examined here.[76] Uncertainties in the absolute CID cross section magnitudes have been previously estimated to be ±20%, whereas uncertainties in the relative cross section magnitudes are smaller, ~ ±5%.[76]

RESULTS

Cross Sections for Collision-Induced Dissociation. Experimental cross sections were obtained for the interaction of four $[2C_nmim{:}BF_4]^+$ IL clusters with Xe, where n = 2, 4, 6, and 8. The energy-dependent CID cross section for the $[2C_4mim{:}BF_4]^+$ cluster is shown for example in **Figure 2**. The energy-dependent CID behavior observed for the other $[2C_nmim{:}BF_4]^+$ clusters is highly parallel to that seen here for $[2C_4mim{:}BF_4]^+$, and results for all four clusters are compared in **Figure S1** of the Supporting Information. The dominant fragmentation pathway observed for all four $[2C_nmim{:}BF_4]^+$ clusters, over the entire collision energy range examined (E_{cm} typically

varies from ~ 0 to > 8 eV), is the loss of a neutral ion pair, ($C_n$mim:BF_4), with detection of the ejected cation, $[C_n\text{mim}]^+$, as shown in **reaction 4**.

$$[2C_n\text{mim:}BF_4]^+ + Xe \rightarrow [C_n\text{mim}]^+ + (C_n\text{mim:}BF_4) + Xe \quad (4)$$

Sequential dissociation of the $[C_n\text{mim}]^+$ primary product cation is observed at collision energies greater than ~ 4 eV (cm). In all cases, formation of the 3-methylimidazolium cation ($C_4H_7N_2^+$), via neutral loss of the 1-alkyl substituent is observed as the dominant sequential dissociation pathway. The $[C_n\text{mim}]^+$ cations also exhibit $[C_nH_{2n+1}]^+$ cation series, products arising from cleavage along the 1-alkyl substituent. As these high-energy sequential CID pathways are not of primary interest here, they will not be discussed further. All of the CID pathways observed for the $[2C_n\text{mim:}BF_4]^+$ clusters are described in **Table S1** of the Supporting Information.

As noted above, the energy-dependent CID behavior observed for all four $[2C_n\text{mim:}BF_4]^+$ clusters is highly parallel (see **Figure S1**). The cross section shapes, magnitudes, and apparent onsets are all very similar. As both the absolute binding energies and trends in the binding of these clusters are of great interest, the $[C_n\text{mim}]^+$ primary product cross sections are compared in greater detail in **Figure 3**. As can be seen in the expanded overlay shown in the figure, the apparent thresholds increase in the order: $[C_2\text{mim}]^+ < [C_4\text{mim}]^+ < [C_6\text{mim}]^+ < [C_8\text{mim}]^+$, suggesting that the binding is the weakest for the cluster involving the smallest cation and increases slightly with increasing size of the cation, or equivalently with increasing length of the 1-alkyl substituent. However, extracting meaningful trends from such simple analyses of the apparent CID thresholds can be problematic, especially for systems that exhibit very minor differences in their energy dependences. This is particularly true for the $[2C_n\text{mim:}BF_4]^+$ clusters examined here as the effects of the size of the $[C_n\text{mim}]^+$ cation on the internal energy and lifetime for dissociation should shift the observed CID cross sections in opposite directions, and the magnitudes of these effects may differ. Thus, it is unclear without detailed thermochemical analysis which of these effects might dominate such that determination of definitive trends in the binding of the $[2C_n\text{mim:}BF_4]^+$ clusters awaits detailed statistical analysis of the CID thresholds (see below).

Electronic Structure Calculations. Stable structures of the $[C_nmim]^+$ and $[BF_4]^-$ ions, ($C_nmim:BF_4$) ion pairs, and $[2C_nmim:BF_4]^+$ clusters were calculated as described in the Theoretical Calculations section. A summary detailing the number of initial structures submitted for B3LYP, B3LYP-GD3BJ, and M06-2X geometry optimization along with the resulting number of "unique" conformers found for each of these levels of theory for each of the $[C_nmim]^+$ cations, ($C_nmim:BF_4$) ion pairs, and $[2C_nmim:BF_4]^+$ clusters is provided in **Table S2**. Histograms of the relative Gibbs energies of all stable conformers computed for each of the $[C_nmim]^+$ cations, ($C_nmim:BF_4$) ion pairs, and $[2C_nmim:BF_4]^+$ clusters are compared in **Figures S3**-**S14**. Details of the B3LYP, B3LYP-GD3BJ, and M06-2X geometry-optimized structures of the ground conformers of the $[C_nmim]^+$ and $[BF_4]^-$ ions, ($C_nmim:BF_4$) ion pairs, and $[2C_nmim:BF_4]^+$ clusters are compared in **Tables S3**-**S6**.

Nomenclature for the $[C_nmim]^+$ cations. To differentiate the stable conformations of the $[C_nmim]^+$ cations, a nomenclature based solely on the dihedral angles that describe the conformation of the 1-alkyl substituent is used as the 3-methylimidizolium moiety takes on essentially the same conformation in all of the stable structures found, see **Figure S2** of the Supporting Information. For the $[C_2mim]^+$ cation only a single dihedral angle, a1 = ∠C2N1C1′C2′, is needed to describe the 1-alkyl conformation. The larger $[C_nmim]^+$ cations require two additional dihedral angles to describe each additional ethyl moiety: a2 = ∠N1C1′C2′C3′ and a3 = ∠C1′C2′C3′C4′ for $[C_4mim]^+$, and a4 = ∠C2′C3′C4′C5′ and a5 = ∠C3′C4′C5′C6′ for $[C_6mim]^+$, and a6 = ∠C4′C5′C6′C7′ and a7 = ∠C5′C6′C7′C8′ for $[C_8mim]^+$. The dihedral angles are designated with a **c** for cis for angles in the range between –45° and 45°, $\mathbf{g}_+$ for gauche(+) for angles between 45° and 135°, $\mathbf{g}_-$ for gauche(-) for angles between −135° and –45°, and **t** for trans for angles between 135° and 225°. Importantly, the $\mathbf{g}_+$ and $\mathbf{g}_-$ designations for the a1 dihedral angle provide a facile means of differentiating enantiomeric structures (see for example the $[g_-t_6]^+$ and $[g_+t_6]^+$ conformers of $[C_8mim]^+$ shown in **Figure S2**). The $[C_nmim]^+$ conformer designations are accompanied by square brackets and the charge to indicate that these are conformers of cations.

Stable Conformations of $[C_nmim]^+$. The B3LYP and M06-2X ground conformers of the $[C_nmim]^+$ cations with NCI plots superimposed on the structures are compared in **Figure 4**. The B3LYP-GD3BJ ground conformers are not shown as their geometries appear virtually identical to the M06-2X structures. The optimized geometries of the ground, low-energy and select stable conformations computed for the $[C_nmim]^+$ cations along with their relative Gibbs energies at 298 K are compared in **Figures S15**-**S18** of the Supporting Information.

The $[C_nmim]^+$ cations possess two major structural motifs, an essentially planar 3-methylimidazolium moiety common to all four cations, and a 1-alkyl chain of variable length. In the B3LYP ground conformers, the 1-alkyl chains of the $[C_nmim]^+$ cations adopt anti-staggered geometries to minimize steric repulsion, and the 3-methyl substituents are rotated such that the hydrogen atom oriented toward the C2H moiety lies in the plane of the imidazolium ring. Notably, the NCI surfaces visible in the B3LYP optimized structures exhibit no stabilizing interactions. Using the nomenclature of **Figure S2**, the B3LYP 298 K ground conformations of the $[C_nmim]^+$ cations are described as g_+ or g-, g_+t_2 or g_-t_2, g_+t_4 or g_-t_4, and g_+t_6 or g_-t_6, respectively. The B3LYP-GD3BJ and M06-2X ground conformers of the $[C_nmim]^+$ cations are fairly similar to those determined via B3LYP optimization. However, the incorporation of dispersion in the former, and the extensive parameterization in the latter, model leads to some twisting of the 1-alkyl substituent to enable stabilizing noncovalent interactions along the chain, and in particular, between the C3′ hydrogen atom and the π cloud of the 3-methylimidazolium moiety as can be readily seen for the M06-2X ground conformers of the three largest $[C_nmim]^+$ cations in **Figure 4**. A much weaker noncovalent interaction between the C2′ hydrogen atom and C5 carbon of the imidazolium ring is evident for all four $[C_nmim]^+$ cations.

ESP maps of the B3LYP and M06-2X ground conformers of the $[C_nmim]^+$ cations are compared in **Figure 5**. As can be seen from the Mülliken charges on the hydrogen atoms shown on the ESP maps, the excess charge is delocalized along the entire surface of the $[C_nmim]^+$ cation. The charge of the imidazolium ring hydrogen atoms exceeds that of the alkyl chain hydrogen atoms, with the C2 hydrogen atom exhibiting the greatest Mülliken charge. The electrostatic

potential computed using M06-2X slightly exceeds that determined by B3LYP over the entire ESP map for all four cations. Notably, the computed Mülliken charge on the C2′ hydrogen atom exceeds that of the C3′ hydrogen atom indicating that the stronger NCI between the C3′ hydrogen atom and the π-cloud seen in the M06-2X ground structures is the result of geometric constraints rather than electrostatic potential.

Additional stable low-energy conformations of the $[C_nmim]^+$ cations are found in which the 1-alkyl chain is twisted such that one of more gauche interactions occurs while generally maintaining staggered interactions. The number of possible low-energy excited conformers arising from such twisting of the 1-alkyl chain increases with length, and leads to a greater number of stable conformers being found for the larger cations. The folding of the 1-alkyl substituent is the dominant difference found among the stable $[C_nmim]^+$ conformers computed; the structure of the 3-methylimidazolium moiety is essentially preserved including the orientation of the 3-methyl substituent.

Examination of the stable structures found for the $[C_nmim]^+$ cations (see **Figures S15-S18**) shows that the a1 = ∠C2N1C1′C2′ dihedral angle is almost always gauche. Indeed only a single stable structure with a cis a1 dihedral angle is found for $[C_2mim]^+$ and $[C_4mim]^+$; none were found for $[C_6mim]^+$ or $[C_8mim]^+$. B3LYP prefers all trans dihedral angles along the alkyl chain, whereas a gauche a2 = ∠N1C1′C2′C3′ dihedral angle enhances the stability of the $[C_nmim]^+$ conformers for B3LYP-GD3BJ and M06-2X. The energetic cost associated with each additional gauche interaction along the 1-alkyl substituent is quite small (~1–4 kJ/mol) for B3LYP and generally much smaller (< 1 kJ/mol) for B3LYP-GD3BJ and M06-2X.

$[BF_4]^-$. NCI plots and ESP maps of the B3LYP and M06-2X ground conformers of $[BF_4]^-$ are also included in **Figures 4** and **5** and discussed in the Supporting Information.

Nomenclature for ($C_n$mim:BF_4) Ion Pairs. To differentiate the stable conformations of the ($C_n$mim:BF_4) ion pairs, a nomenclature based on a description of the binding site (**b1BS**) and the dihedral angles that describe the conformation of the 1-alkyl substituent (an) is used, i.e., (**b1BS**;a1…an) as described in **Figure S2** of the Supporting Information. Several stable

low-energy modes of binding of $[BF_4]^-$ to the $[C_nmim]^+$ cations are found. Binding in which the boron atom lies on the C2 side of the cation is designated as front-side binding (**F**) versus binding along the opposite side is designated as back-side binding (**B**). These binding site designations are further differentiated depending on whether the boron atom lies near the center of the imidazolium ring (i.e., oriented along the direction of the C2–H bond) **F** and **B**, or lies closer to the 1-alkyl ($\mathbf{F_a}$ or $\mathbf{B_a}$) or 3-methyl ($\mathbf{F_m}$ or $\mathbf{B_m}$) substituents. These designations are readily determined from the dihedral angle defined by **b** = ∠C2©(©+CP)B, where © denotes the centroid of the imidazolium ring, CP denotes the point describing the cross product of the C2–N1 and C2–N3 bond vectors, and (©+CP) their vector sum. The specific ranges of dihedral angles that define each of these binding site designations are given in **Figure S2**. The binding site is further designated based on the relative orientations of the imidazolium ring and the boron atom using the dihedral angle **b1** = ∠C1′′N3C2B, where **b1** designates binding as above, below, in front of, and behind the imidazolium ring as **c**, $\mathbf{g_+}$, **t** and $\mathbf{g_-}$. The ($C_nmim:BF_4$) conformer designations are accompanied by parentheses and no charge to indicate that these are conformers of neutral ion pairs, e.g., the B3LYP ground conformer of ($C_2mim:BF_4$) is designated as ($\mathbf{g_+F}$;g_-), see **Figure S2** of the Supporting Information.

Stable Conformations of the ($C_nmim:BF_4$) Ion Pairs. The B3LYP and M06-2X ground conformers of the ($C_nmim:BF_4$) ion pairs with NCI plots superimposed on the structures are compared in **Figure 6**. The B3LYP-GD3BJ ground conformers are not shown in the figure as their geometries appear virtually identical to either the B3LYP or M06-2X structures. The optimized geometries of the ground, low-energy and select stable conformations computed for the ($C_nmim:BF_4$) ion pairs along with their relative Gibbs energies at 298K are compared in **Figures S19-S22**.

Front-side binding along the direction of the C2H moiety (**F**) is found among the ground conformers of the ($C_nmim:BF_4$) ion pairs regardless of which theoretical model is employed, consistent with earlier computational work.[43-46] The preferred relative orientations of the imidazolium ring and the boron atom as defined by the **b1** = ∠C1′′N3C2B dihedral angle are

generally gauche, although cis conformations (with **b1** near 45º) are of very similar stability (see **Table S5** and **Figures S19-S22**). The intrinsic cation-anion binding interactions are preserved among the ground conformers of all four ion pairs and involve noncanonical hydrogen-bonding interactions between the C1′, C2, and C1″ hydrogen atoms of the $[C_nmim]^+$ cation and two of the F atoms of the $[BF_4]^-$ anion. Additional stabilization is achieved via anion-π interaction between a third F atom and the π-cloud of the imidazolium ring. These binding interactions are readily seen in the NCI surfaces of **Figure 6** clearly show that the C2, C1′ and C1″ hydrogen atoms all play key roles in the binding. The NCI surfaces computed for B3LYP are less extensive than those predicted by M06-2X. The cation-anion interaction length (as measured by the C2–B distance) is highly conserved throughout the ground conformers of the ($C_nmim:BF_4$) ion pair series for each level of theory. However, B3LYP predicts a longer C2–B distance (~ 3.15 Å) than B3LYP-GD3BJ (~3.09 Å) and M06-2X (~2.94 Å), see **Table S5**, consistent with the NCI surfaces computed. An anti-staggered geometry of the 1-alkyl substituent is generally preferred, but folding to achieve additional interactions with $[BF_4]^-$ is observed, particularly for the ($C_6mim:BF_4$) and ($C_8mim:BF_4$) ion pairs for B3LYP-GD3BJ and M06-2X.

ESP maps of the B3LYP and M06-2X ground conformers of the ($C_nmim:BF_4$) ion pairs are compared in **Figure S23**. The excess positive charge is delocalized along the entire surface of the $[C_nmim]^+$ cation and the electrostatic potential of the imidazolium ring hydrogen atoms exceeds that of the alkyl chain hydrogen atoms, with the C2 hydrogen atom again exhibiting the greatest electrostatic potential. The presence of the $[BF_4]^-$ anion in the ($C_nmim:BF_4$) ion pair induces additional polarization such that the electrostatic potential on the C1′, C2, and C1″ hydrogen atoms is enhanced versus that of the isolated cations. The presence of the $[C_nmim]^+$ cation also induces additional polarization of the electron density of the $[BF_4]^-$ anion such that the electrostatic potential on the three F atoms directed toward the cation increases, while that of the F atom directed away from the cation decreases, versus that of the isolated anion. The electrostatic potential computed using M06-2X again exceeds that determined by B3LYP over the entire cation, and is lower on the F atoms for all four ($C_nmim:BF_4$) ion pairs. The very minor

differences in the ESP maps across the ($C_n$mim:BF_4) ion pair series indicate that the intrinsic cation-anion binding interactions in these ion pairs are only weakly influenced by the length of the 1-alkyl chain.

Additional stable low-energy conformations of the ($C_n$mim:BF_4) ion pairs are found. As can be seen in the ($C_n$mim:BF_4) binding site distribution plots of **Figures S24-27**, all four ion pairs exhibit a very strong preference for front-side binding, consistent with early computational work.[43-46]. The range of the binding site dihedral angles **b** among the low-energy conformers becomes somewhat broader as the size of the cation increases and is also broader for B3LYP-GD3BJ and M06-2X than B3LYP. No $\mathbf{F_m}$ binding conformers are found for (C_2mim:BF_4) at any level of theory. However, $\mathbf{F_m}$ binding is found among the stable conformers of the three largest ($C_n$mim:BF_4) ion pairs, and becomes increasingly favorable as the size of the cation increases and for B3LYP-GD3BJ and M06-2X structures. $\mathbf{F_m}$ binding conformers are ~7–15 kJ/mol less favorable than the ground **F** binding conformers. Only a single $\mathbf{B_a}$ conformer is found for (C_2mim:BF_4) with B3LYP, but none are found for B3LYP-GD3BJ or M06-2X. $\mathbf{B_a}$ binding conformers become somewhat more favorable as the size of the cation increases and are found for the three largest ($C_n$mim:BF_4) ion pairs at all three levels of theory, and are ~29–40 kJ/mol less favorable than the ground **F** binding conformers. No $\mathbf{B_m}$ binding conformers are found for (C_2mim:BF_4) at any level of theory, but are found among the stable conformers of the three largest ($C_n$mim:BF_4) ion pairs, become slightly more favorable as the size of the cation increases, and are ~27–45 kJ/mol less stable than the ground **F** binding conformers. No $\mathbf{F_a}$ or **B** binding conformers are found for any of the ($C_n$mim:BF_4) ion pairs for any of the theoretical models. Twisting of the 1-alkyl substituent can lead to additional favorable noncovalent interactions between the cation and anion and enhance the stability of the ion-pairing interaction. Conformers in which the 1-alkyl substituent wraps around the $[BF_4]^-$ anion are particularly favorable for B3LYP-GD3BJ and M06-2X. As the length of the 1-alkyl substituent increases, stable structures tend to become more globular in nature.

Nomenclature for $[2C_nmim:BF_4]^+$ Clusters. To differentiate the stable conformations of the $[2C_nmim:BF_4]^+$ clusters, a nomenclature based on a description of the binding sites and the dihedral angles that describe the conformations of the 1-alkyl substituents (an) is used, i.e., [a1…an;**b2b1BS(1)b1BS(2)**;a1…an]$^+$ as described in **Figure S2** of the Supporting Information. Although in principle the same modes of binding of $[BF_4]^-$ to the $[C_nmim]^+$ cations are possible, only **FF** binding is observed in the most stable structures found except for the $[2C_nmim:BF_4]^+$ cluster where one low-energy conformer involving an $\mathbf{F_mF}$ binding mode is found (see **Figures S28-S31**). The binding mode is further designated based on the relative orientations of the imidazolium rings of the two $[C_nmim]^+$ cations as defined by the dihedral angle **b2** = ∠C1′(1)N1(1)N1(2)C1′(2), where the numbers in parentheses designate the first and second $[C_nmim]^+$ cations. Similar to the an and **b1** dihedral angles, **b2** is designated as **c**, $\mathbf{g_+}$, **t** and $\mathbf{g_-}$. The $[2C_nmim:BF_4]^+$ conformer designations are accompanied by square brackets and the charge to indicate that these are conformers of cations. See for example the $[g\_t_6;\mathbf{g\_FF};g\_t_6]^+$ conformer of $[2C_8mim:BF_4]^+$ displayed in **Figure S2** of the Supporting Information.

Stable Conformations of the $[2C_nmim:BF_4]^+$ Clusters. The B3LYP and M06-2X ground conformers of the $[2C_nmim:BF_4]^+$ clusters with NCI plots superimposed on the structures are compared in **Figure 7.** The B3LYP-GD3BJ ground conformers are not shown in the figure as their geometries again appear virtually identical to either the B3LYP or M06-2X structures. The optimized geometries of the ground, low-energy and select stable conformations computed for the $[2C_nmim:BF_4]^+$ clusters along with their relative Gibbs energies at 298 K are compared in **Figures S28-S31**.

Front-side binding along the direction of the C2H moiety is found for both binding interactions in the ground **FF** conformers of the $[2C_nmim:BF_4]^+$ clusters regardless of which theoretical model is employed except for the $[2C_6mim:BF_4]^+$ cluster where $\mathbf{F_mF}$ binding is found to be the most stable at the M06-2X level. The intrinsic cation-anion binding interactions again involve noncanonical hydrogen-bonding interactions between the C1′, C2, and C1″ hydrogen atoms of each of the $[C_nmim]^+$ cations with two of the F atoms of the $[BF_4]^-$ anion. These

binding interactions are seen in the NCI surfaces of **Figure 7**. Coulombic and steric repulsion between the two $[C_nmim]^+$ cations eliminates the anion-π interaction with a third F atom present in the ($C_nmim:BF_4$) ion pairs in the B3LYP and B3LYP-GD3BJ structures such that the **b1** dihedral angles are generally cis. In contrast, differences in exchange correlation for M06-2X optimized structures further stabilize anion-π and dispersion interactions resulting in a smaller ∠C2HB binding angle and more globular structures. For the longer 1-alkyl chains of $[2C_6mim:BF_4]^+$ and $[2C_8mim:BF_4]^+$, dispersion interactions stabilize globular structures for B3LYP-GD3BJ and M06-2X vs. the anti-staggered geometries preferred by B3LYP. The $[2C_6mim:BF_4]^+$ structures are globular and nearly identical at B3LYP-GD3BJ and M06-2X, whereas $[2C_8mim:BF_4]^+$ adopts globular structures at B3LYP-GD3BJ and somewhat flatter π-π stacking structures at M06-2X. Ligand-ligand repulsion also results in an increase in the cation-anion interaction length from ~ 3.14 Å to ~ 3.67 Å (as defined by the C2–B distance(s), see **Tables S5** and **S6**). The increase in the cation-anion interaction length indicates that the intrinsic cation-anion binding interactions in the 2:1 cluster are weaker than in the isolated ion pair as expected for binding based on noncovalent interactions. This is easily understood based on the polarization of the $[BF_4]^-$ anion in the ($C_nmim:BF_4$) ion pair, where the binding of the first $[C_nmim]^+$ cation reduces the electrostatic potential of the F atoms oriented toward the second cation (see **Figure S23**). Further, this behavior is typical of ligation/solvation processes, where a decrease in the Coulombic attraction for additional ligands is observed upon binding of each additional ligand, and dipole-dipole repulsive interactions between ligands increase with the extent of ligation.[81-83] An anti-staggered geometry of the 1-alkyl substituents is again preferred, with the alkyl chains aligned in a parallel fashion. The preferred relative orientations of the imidazolium rings as defined by the **b2** dihedral angle are generally gauche, although trans (with **b2** near 150º) are of very similar stability for M06-2X (see **Table S6** and **Figures S24-S27**).

The NCI surfaces computed for B3LYP are again less extensive than those predicted by M06-2X. The cation-anion interaction length (as measured by the C2–B distance) is highly conserved throughout the ground conformers of the $[2C_nmim:BF_4]^+$ cluster series for B3LYP,

whereas both B3LYP-GD3BJ and M06-2X exhibit more variability. B3LYP again predicts a longer C2–B distance (~ 3.67 Å) than B3LYP-GD3BJ (~3.5–3.6 Å) and M06-2X (~3.0–3.6 Å), see **Table S6**, consistent with the NCI surfaces computed. An anti-staggered geometry of the 1-alkyl substituent is again generally preferred, but folding to achieve additional interactions with $[BF_4]^-$ is observed, particularly for the $[2C_6mim{:}BF_4]^+$ and $[2C_8mim{:}BF_4]^+$ clusters.

ESP maps of the B3LYP and M06-2X ground conformers of the $[2C_nmim{:}BF_4]^+$ clusters are compared in **Figure S32**. The C1′, C2 and C1″ hydrogen atoms of the imidazolium cation remain the most favorable sites for interaction with $[BF_4]^-$. The alternating charge (+–+) of the cluster induces additional polarization such that the electrostatic potential on the C1′, C2, and C1″ hydrogen atoms is enhanced versus that of the isolated cations and ion pairs. The presence of the second cation redistributes the polarization of the anion such that the Mülliken charges on all four F atoms are similar in the B3LYP ground conformers. In contrast, the polarization of the F atoms in the M06-2X structures is less symmetric, with lower Mülliken charges on the F atoms closer to the 1-alkyl than 3-methyl substituents, particularly for the $[2C_2mim{:}BF_4]^+$ cluster. Notably, the electrostatic potential on the hydrogen atoms of the 1-alkyl chain is enhanced when it participates in the binding (see in particular the $[2C_6mim{:}BF_4]^+$ and $[2C_8mim{:}BF_4]^+$ clusters of **Figure S32**). The electrostatic potential computed using M06-2X again exceeds that determined by B3LYP. The modest differences in the ESP maps across the $[2C_nmim{:}BF_4]^+$ cluster series indicate that the intrinsic cation-anion binding interactions in these clusters are only weakly influenced by the length of the 1-alkyl chain.

Additional stable low-energy conformations of the $[2C_nmim{:}BF_4]^+$ clusters are found. As can be seen in the $[2C_nmim{:}BF_4]^+$ binding site distribution plots of **Figures S33-36**, all four clusters exhibit a very strong preference for front-side binding such that the very low-energy conformers exhibit primarily **FF** binding sites. The range of the binding site dihedral angles **b** among the low-energy conformers is broadest for the $[2C_2mim{:}BF_4]^+$ cluster, and while it remains moderately broad, it becomes somewhat narrower for the larger cations. The range of **b** is also broader for B3LYP-GD3BJ and M06-2X than found for B3LYP. $\mathbf{F_m}$ binding is the next

most represented in the binding site distribution plots. Indeed, the M06-2X ground conformer of $[2C_6mim:BF_4]^+$ exhibits $\mathbf{F_mF}$ binding. Conformers with $\mathbf{F_mF}$ binding modes are most favorable for M06-2X, followed by B3LYP-GD3BJ, and least favorable for B3LYP with the most stable $\mathbf{F_mF}$ conformers 4-23 kJ/mol less stable than the ground conformers (again excepting the $[2C_6mim:BF_4]^+$ cluster). $\mathbf{F_a}$ binding is also observed, but very few conformers exhibiting $\mathbf{F_aF}$ binding modes are found. Among those found, $\mathbf{F_aF}$ binding becomes increasingly unfavorable for B3LYP and more favorable for B3LYP-GD3BJ and M06-2X as the length of the 1-alkyl substituent increases. $\mathbf{B_a}$ and $\mathbf{B_m}$ binding are roughly equally represented in the stable conformers determined and also exhibit similar strength of binding as $\mathbf{B_aF}$ and $\mathbf{B_mF}$ conformers are typically 14–43 kJ/mol less favorable than the ground conformers. **B** binding is found among a handful of the stable conformers found, but is 19–46 kJ/mol less favorable than the ground conformers and is often accompanied with $\mathbf{F_a}$ or $\mathbf{F_m}$ binding of the second cation. Twisting of the 1-alkyl substituents again leads to additional favorable noncovalent interactions between the cation and anion (see for example the ground conformer of $[2C_6mim:BF_4]^+$, **Figure 7**) and between the two cations (see for example the ground conformer of $[2C_8mim:BF_4]^+$, **Figure 7**) and enhances the stability of the binding interactions. These additional stabilizing interactions are particularly favorable for B3LYP-GD3BJ and M06-2X such that stable structures tend to become more globular in nature as the length of the 1-alkyl substituent increases.

Isotopic Molecular Polarizabilities. Isotropic molecular polarizabilities of the $[C_nmim]^+$ cations, $[BF_4]^-$ anion, $(C_nmim:BF_4)$ ion pairs and $[2C_nmim:BF_4]^+$ clusters were calculated as described in the theoretical calculations section. As expected, the polarizability of the $[C_nmim]^+$ cations, $(C_nmim:BF_4)$ ion pairs and $[2C_nmim:BF_4]^+$ clusters increase linearly with the size of the 1-alkyl substituent as shown in **Figure S37**. The B3LYP/6-311+G(d,p) polarizabilities of the $[C_nmim]^+$ cations are 11.4, 15.2, 18.9, and 22.6 $Å^3$, $(C_nmim:BF_4)$ ion pairs are 14.7, 18.2, 22.1, 25.5 $Å^3$, and $[C_nmim:BF_4]^+$ clusters are 26.4, 33.6, 41.2, and 48.6 $Å^3$, for n = 2, 4, 6 and 8, respectively. The computed PBE1PBE/6-311+G(2d,2p) polarizabilities of the $(C_nmim:BF_4)$ ion pairs differ very little from the B3LYP values (by ~ 2%) and are 15.0, 18.6, 22.1, 25.5 $Å^3$,

respectively. We have historically used polarizabilities computed at the PBE1PBE/6-311+G(2d,2p) level of theory for thermochemical analysis of the CID cross sections, but these small differences indicate that the additional polarizability calculations are not necessary as B3LYP/6-311+G(d,p) also accurately predicts molecular polarizabilities of the ($C_n$mim:BF_4) ion pairs. The distribution of ($C_n$mim:BF_4) B3LYP/6-311+G(d,p) polarizabilities for all conformers are included in **Figure S38**. As can be seen in the figure, the polarizability distributions are rather narrow regardless of the binding geometry, indicating that conformational changes do not significantly influence the polarizability of these ion pairs.

Threshold Analysis of CID Cross Sections. The empirical threshold law described by **eq 3** was used to model the threshold regions of the zero-pressure-extrapolated cross sections for the primary CID pathway, **reaction 4**, observed for four $[2C_n\text{mim:}BF_4]^+$ IL clusters using procedures detailed in the **Thermochemical Analysis** section. The recommended scaling factor for vibrational frequencies computed at the B3LYP/6-311+G(2d,2p) level of theory (0.9887) was used, whereas the scaling factors used for the B3LYP-GD3BJ and M06-2X vibrational frequencies was determined by comparison to the B3LYP values. Excellent correlation is found when the B3LYP-GD3BJ and M06-2X vibrational frequencies are used without scaling (scale factor = 1.000) as shown in **Figures S39** and **S40** of the Supporting Information. A representative analysis for the $[2C_4\text{mim:}BF_4]^+$ cluster is shown in **Figure 8**; results for all four $[2C_n\text{mim:}BF_4]^+$ clusters are compared in **Figure S41**. As a result of the noncovalent nature of the cation-anion interactions responsible for the binding in these IL clusters, and thus the resultant dissociation behavior, cross sections for **reaction 4** were analyzed using a loose phase space limit transition state (PSL TS) model.[62] The PSL TS model has been shown to provide the most accurate correction of kinetic shifts observed for CID reactions of noncovalently bound complexes.[81,82,84-89] As can be seen in the figures, the CID data are well reproduced using the PSL TS model over energy ranges exceeding 4 eV and cross section magnitudes of a factor of at least 100 for all four $[2C_n\text{mim:}BF_4]^+$ IL clusters. The CID cross sections were also modeled without including lifetime effects. Results of these thermochemical analyses using the B3LYP

vibrational frequencies for fitting are summarized in **Table 1**. The B3LYP calculated vibrational frequencies, average vibrational energies at 298 K, and rotational constants of the ground conformers, i.e., the structures used in the threshold analyses, are provided in **Tables S7** and **S8**.

The difference between the threshold values determined excluding and including lifetime effects, E_0 and E_0(PSL), provides a determination of the kinetic shift in the experimental data and is also given in **Table 1**. The kinetic shifts are significant and increase from 0.70 eV for $[2C_2mim{:}BF_4]^+$, the smallest cluster with 123 vibrational modes, to 1.55 eV for $[2C_8mim{:}BF_4]^+$, the largest cluster with 231 vibrational modes. The trends in kinetic shift are easily rationalized based on the sizes of the systems, specifically the degrees of freedom available to the energized molecule and the transition state (TS) for dissociation. Similar results are obtained when the CID cross sections are analyzed using the B3LYP-GD3BJ and M06-2X frequencies for fitting, which are summarized in **Tables S9** and **S10** of the Supporting Information. The thresholds determined differ from those for B3LYP by 0.02 to 0.09 eV across these systems, and fall within the combined uncertainties in these determinations. Notably, the thresholds determined are smaller except for the $[2C_8mim{:}BF_4]^+$ cluster when analyses are based on the B3LYP-GD3BJ ground structures, whereas the thresholds determined are larger except for the $[2C_4mim{:}BF_4]^+$ cluster when analyses are based on the M06-2X ground structures vs. those determined using B3LYP. In contrast, the kinetic shifts are the smallest for M06-2X, slightly larger for B3LYP, and the largest for B3LYP-GD3BJ except for the $[2C_8mim{:}BF_4]^+$ cluster, which exhibits a slightly smaller kinetic shift for B3LYP-GD3BJ than B3LYP.

Because multiple very low-energy conformations of the $[2C_nmim{:}BF_4]^+$ clusters may be populated in the experiments, the CID cross sections were also analyzed using the molecular parameters of other low-energy (non ground) conformers to evaluate the robustness of our threshold determinations. For all very low-energy conformers examined (front-side binding and within 20 kJ/mol of the ground conformer), the thresholds determined were well within the experimental error of the determinations based on the ground conformers. In contrast, analyses based on the molecular parameters of the relatively higher-energy conformers examined

(back-side binding and > 20 kJ/mol of the ground conformer) exhibited higher threshold values that were outside of the experimental uncertainty in the determinations (and in poorer agreement with computed values). Further, the thresholds determined exhibited very little dependency on the polarizability of the ($C_n$mim:BF_4) neutral ion pair where fits using the range of polarizability values determined for the various stable conformers produced threshold values that only differed by ~0.1 kJ/mol. These results indicate that the threshold values determined here are robust and that only very low-energy conformations are likely populated in the experiments and thus contributing to the threshold determinations.

The entropy of activation, $\Delta S^{\dagger}$, the entropy difference between the transition state and the reactants provides a measure of the looseness of the TS and the size/complexity of the system. Listed in **Table 1** are the $\Delta S^{\dagger}$(PSL) values at 1000 K, which exhibit modest variation as a function of size of the cluster and vary from 18 to 47 J mol^{-1} K^{-1} across these systems. The $\Delta S^{\dagger}$ values of all four $[2C_n\text{mim:}BF_4]^+$ clusters are consistent with those previously determined for CID of noncovalently bound complexes that have been previously measured in our laboratory[81,82,84-89] and to those compiled by Lifshitz[90] for simple bond cleavage reactions of ionic species. **Tables S9** and **S10** summarize $\Delta S^{\dagger}$ values derived from the B3LYP-GD3BJ and M06-2X analyses.

Conversion from 0 to 298 K. To facilitate comparison of the 0 K BDEs determined here to values typically reported in the literature, these values are converted to 298 K enthalpies and free energies. The enthalpy and entropy conversions are calculated using standard formulas based on harmonic oscillator and rigid rotor models and the vibrational frequencies and constants determined from the B3LYP optimized geometries, given in **Tables S7** and **S8** of the Supporting Information. **Table 2** lists 0 and 298 K B3LYP enthalpy, free energy, and entropic corrections for all four $[2C_n\text{mim:}BF_4]^+$ clusters experimentally determined. Uncertainties in the enthalpic and entropic corrections are approximated by 10% variation in the vibrational frequencies and rotational constants.

DISCUSSION

Comparison of Theory and Experiment. The B3LYP, B3LYP-GD3BJ, and M06-2X computed BDEs are compared to the TCID measured values in **Table 3** and **Figure 9**. The TCID values listed in **Table 3** and **Figure 9** are based on thermochemical analyses using the B3LYP optimized geometries. Both B3LYP and B3LYP-GD3BJ predict BDEs that are in excellent agreement with the TCID measured values. The mean absolute deviation (MAD) between the B3LYP computed and TCID measured values is 1.8 ± 1.4 kJ/mol, whereas the MAD for B3LYP-GD3BJ is quite similar, 1.9 ± 1.3 kJ/mol. In contrast, the MAD for M06-2X vs. the TCID values is much larger, 11.3 ± 5.7 kJ/mol (see **Figure S42** of the Supporting Information), but reduces to 4.0 ± 5.1 kJ/mol when BSSE corrections are not included (M06-2X*, see **Figure 9**). Similar comparisons using TCID 0 K BDEs based on thermochemical analyses using the B3LYP-GD3BJ and M06-2X optimized geometries are summarized in **Figure S43** of the Supporting Information. As can be seen in the figure, the performance of both B3LYP-GD3BJ and M06-2X degrades somewhat when the thermochemical analyses are based on structures computed using these methods; the MADs increase to 4.9 ± 2.9 kJ/mol for B3LYP-GD3BJ and 13.3 ± 5.8 kJ/mol for M06-2X, which again reduces when BSSE corrections are not included, to 5.8 ± 4.8 kJ/mol. These latter comparisons also indicate that the B3LYP values are the most reliable, but that B3LYP-GD3BJ predicts energetics reasonably well. In contrast, M06-2X predicts values that are reasonable when BSSE corrections are not included, but that are systematically low when BSSE corrections are included.

Trends in the Measured $[2C_nmim{:}BF_4]^+$ BDEs. The BDEs determined for the $[2C_nmim{:}BF_4]^+$ clusters based on thermochemical analyses using the B3LYP ground structures as reported in **Table 3** are 120.4 ± 4.2 kJ/mol, 118.2 ± 5.0 kJ/mol, 120.9 ± 6.0 kJ/mol, and 123.0 ± 6.3 kJ/mol for the n = 2, 4, 6, and 8 clusters, respectively. Remarkably, the variation in the measured BDEs across these systems is quite small, only 4.8 ± 8.0 kJ/mol, which is of similar magnitude to the average experimental uncertainty in these determinations, 5.4 ± 1.0 kJ/mol. As a result, the trends in the BDEs as a function of the $[C_nmim]^+$ cation are

indistinguishable based solely on the current experimental measurements. Considering the minimal structural change across the cation series for the relevant structures of $[2C_nmim{:}BF_4]^+$, ($C_nmim{:}BF_4$), and $[C_nmim]^+$, the minor variation among these BDEs is not too surprising.

It is challenging to a priori predict an accurate trend in the BDEs of the $[2C_nmim{:}BF_4]^+$ clusters as several competing effects influence the binding in a size-dependent manner. As the length of the 1-alkyl substituent of the $[C_nmim]^+$ cation increases, the electron density is distributed over a larger volume such that the diffusivity of the cation increases, which should result in the weakening of the BDE. However, if the 1-alkyl substituent engages in the binding this effect may be relatively insignificant. Electron donation into the imidazolium ring by the 1-alkyl substituent also increases with increasing length, making the larger cations weaker Lewis acids, which should also result in the weakening of the BDE. In contrast, the polarizability volume of the cation increases with increasing length of the 1-alkyl substituent (see **Figure S37**) resulting in increased dispersion forces, which should strengthen the BDE. These opposing effects appear to nearly cancel as the measured BDEs are all within experimental error of each another. Indeed the BDEs of the $[2C_nmim{:}BF_4]^+$ clusters measured in this work exhibit an average value of 120.6 ± 2.0 kJ/mol; this very minor variation however, does not exhibit a simple correlation with the size of the 1-alkyl substituent. TCID results suggested a relative ordering of the BDEs as $[2C_8mim{:}BF_4]^+ > [2C_6mim{:}BF_4]^+ > [2C_2mim{:}BF_4]^+ > [2C_4mim{:}BF_4]^+$ (or 8 > 6 > 2 > 4), but again the uncertainties in these measured values are larger than the differences such that the relative order of binding is not definitively established. B3LYP results suggests a relative ordering of 2 > 8 > 6 > 4, B3LYP-GD3BJ suggests a relative ordering of 8 > 2 > 6 > 4, and M06-2X suggest a relative ordering of 6 > 2 > 4 > 8. While the absolute binding energies predicted by theory using the basis sets employed in this work are probably not quite as accurately predicted as the measured values are determined, theory is often better at predicting relative trends with high fidelity. However, the binding in these systems is floppy enough, and the conformational flexibility of the 1-alkyl substituents and its potential involvement in the binding and impact on stability of the cation leads to a diversity of structures that may be

important such that we cannot conclusively establish that we have determined the true ground conformers for each level of theory examined. B3LYP results appear to be most consistent in terms of producing parallel structures across the entire cation series. Whereas increased dispersion in the B3LYP-GD3BJ functional and the high degree of parameterization of M06-2X functional lead to less consistency in the structures determined across the cation series, consistent with the energetic comparisons, and suggesting that these latter approaches are somewhat less reliable than B3LYP. However, it should be noted that none behave poorly, the uncertainty in the relative order of binding arises because the accuracy of the measurements and theoretical predictions is on the order or slightly larger than the differences in the strength of binding. To establish a definitive order of binding, competitive measurements are necessary.

Guidance with regard to the relative strength of binding in these systems may be taken from the work of Bini et al.,[30] who examined the competitive CID behavior of mixed clusters of various ILs. Most relevant to the systems examined here are the 1-alkyl-3-methylimidazolium bromide, $C_n$mim-Br, ILs where the relative order of binding to $[Br]^-$ was determined as $[C_2mim]^+ > [C_4mim]^+ > [C_6mim]^+ > [C_8mim]^+$. Given the similarities and differences in the nature of the binding interactions in the $C_n$mim-Br vs. $C_n$mim-BF_4 ILs however, the same relative ordering cannot be assumed. In particular, the larger size of the $[BF_4]^-$ anion likely enables the binding interactions to be further strengthened by interactions with the 1-alkyl chains in the clusters involving the larger cations such that the relative order of binding may change. To definitively establish a definitive order of binding, a follow-up study of the TCID behavior of mixed $[C_{n-2}mim{:}BF_4{:}C_nmim]^+$ clusters is being pursued. Importantly, the results of this follow up study will determine the absolute BDEs of these mixed clusters and the absolute relative order of binding with significantly improved precision. Further, by combining the results of the present study with those from competitive measurements, the BDEs determined for the $[2C_nmim{:}BF_4]^+$ clusters can be more accurately and precisely determined.

Packing Effects. Structural and energetic comparisons of the ($C_n$mim:BF_4) ion pairs and $[2C_nmim{:}BF_4]^+$ clusters suggest that these systems are sufficiently small that packing effects are

minimal. The nature of the binding interactions is basically conserved, with the cation binding in the plane via the C1′, C2, and C1″ hydrogen atoms of the imidazolium ring to two of the fluorine atoms of $[BF_4]^-$. Minor deviations in binding site dihedral angle occur from the ($C_n$mim:BF_4) ion pairs relative to the $[2C_n\text{mim:}BF_4]^+$ clusters. Binding in the $[2C_n\text{mim:}BF_4]^+$ IL clusters is planar with the imidazolium ring and the plane of the BF_2 moiety of the anion. Conversely binding in the ($C_n$mim:BF_4) ion-pair deviates slightly from planarity with the $[BF_4]^-$ preferentially orienting the anion above the imidazolium ring to interact with the π-cloud of the imidazolium cation and gaining additional stabilization via interaction with the 1-alkyl substituent. The latter interactions become increasingly important as the length of the 1-alkyl substituent increases and for structures computed for B3LYP-GD3BJ and M06-2X such that more compact structures of the ($C_n$mim:BF_4) ion pairs and $[2C_n\text{mim:}BF_4]^+$ clusters are important for the systems involving the two largest cations. The very minor variation in the BDEs of the $[2C_n\text{mim:}BF_4]^+$ clusters across the cation series also indicate that packing effects are not yet significantly affecting the energetics of binding.

Structural Comparisons with Previous Work. Previous studies have probed the gas-phase conformations of IL clusters. Johnson and coworkers investigated the isolated cations and 2:1 clusters of C_2mim-BF_4 and C_2dmim-BF_4 (C_2dmim = 1-ethyl-2,3-dimethylimidazolium) using cryogenic ion vibrational spectroscopy.[38,39] Both deuteration and methylation at the C2 position were employed to definitively establish the importance of the C2 hydrogen atom in the binding of $C_n$mim-BF_4 ILs. Calculations at the B3LYP/6-31+G(d,p) directly and also with the incorporation of anharmonic corrections using the VPT2 approach were performed to characterize the structures, energetics and infrared spectra of these systems. Their findings are consistent with present B3LYP results for the $[C_2\text{mim}]^+$ cation and $[2C_2\text{mim:}BF_4]^+$ cluster both in terms of the mode of binding and 1-alkyl substituent orientations. This is not surprising as the same density functional method and similar basis sets were employed. Although a slightly larger basis set was used for geometry optimization in the present work, 6-311+G(d,p) it seems clear

that the key structural features are already described reasonably well with the 6-31+G(d,p) basis set.

Previous work has also examined condensed-phase structures of ILs and found that the conformational flexibility afforded to these systems can lead to crystal polymorphs.[91,92] Two distinct crystal structures exhibiting different mps have been reported for C_2mim-BF_4.[92] The crystal structures exhibit H–F interaction distances of ~2.6 Å and also evidence of H-π and π-π stacking interactions that contribute to the binding in these structures. The H–F distances computed for the ground conformations of the $[2C_2mim{:}BF_4]^+$ cluster structure vary between 2.07–2.47 Å for B3LYP, 2.05–2.42 Å for B3LYP-GD3BJ, and 2.37–2.91 Å for M06-2X, where the C2H-F interaction distances are the shortest and the C1′H-F interaction distances the longest. These results suggest that M06-2X does a better job of describing the structure of the $[2C_2mim{:}BF_4]^+$ cluster than B3LYP and B3LYP-GD3BJ. However, comparison of the H–F distances in the ground conformer of the (C_2mim:BF4) ion pair, 2.07–2.29 Å for B3LYP, 2.05–2.49 Å for B3LYP-GD3BJ, and 2.29–2.41 Å for M06-2X, to those of the $[2C_2mim{:}BF_4]^+$ cluster, make it clear that the H–F distances should increase in larger clusters and in the condensed phases such that definitive conclusions regarding the relative abilities of these models to accurately describe the structure of IL clusters cannot really be made. Further, the intrinsic binding interactions vary somewhat between the crystal structures and the structures computed here. Packing in solid crystalline C_2mim-BF_4 alters the intrinsic binding interactions such that binding occurs between the C1′ and C4 hydrogen atoms of $[C_2mim]^+$ and two of the fluorine atoms of $[BF_4]^-$. This differs from the structures computed for the 2:1 clusters where binding involves the C1′, C1″, and C2 hydrogen atoms again with two of the fluorine atoms of $[BF_4]^-$. This suggests that structural rearrangement due to packing forces occurs during the crystallization process. Structural rearrangement may also be of importance for larger imidazolium-based tetrafluoroborate IL clusters as spectroscopic results for larger clusters have yet to be published.

Implications for Space Propulsion Applications. Molecular mechanics approaches have been used to model ILs in ESI plumes to elucidate information regarding the influence of the specific IL on efficiency and thrust.[93-96] The reliability of such modeling is highly dependent on the accuracy of the parameterization of the molecular mechanics force fields employed, which rely on thermochemistry derived from high-level quantum mechanics calculations and experimental measurements when available. An important motivating factor for the present work is to provide accurate BDEs of IL clusters for use in such modeling and simulation of space propulsion using ILs. The present results provide benchmark thermodynamic measurements that can be used to improve the molecular mechanics force field descriptions of the intrinsic binding interactions in the $[2C_nmim:BF4]^+$ IL clusters. Work is ongoing to expand these studies to include a wider variety of ILs and larger IL clusters to broaden the impact of these measurements for understanding the reaction dynamics of IL clusters for space propulsion applications. The availability of such data should facilitate the development of task-specific ILs as described above. Understanding the interplay between the cations and anions, and their combinations to create unique and desired properties are both needed to advance space propulsion. Present findings indicate that the $[2C_nmim:BF_4]^+$ clusters examined here should exhibit similar efficiencies. However, packing effects are likely to differ with the size of the 1-alkyl substituents of the cations such that this conclusion may not be true for larger clusters of these ILs. Further, ILs comprised of others cations and anions may behave somewhat differently. Thus, expansion of this present work to include larger clusters and a wider variety of ILs is highly desirable and currently being pursued.

CONCLUSIONS

Threshold collision-induced dissociation approaches are used to measure the bond dissociation energies (BDEs) of the 2:1 clusters of a series of 1-alkyl-3-methylimidazolium cations and tetrafluoroborate, $[2C_nmim:BF_4]^+$. The length of the 1-alkyl substituent of the $[C_nmim]^+$ cation is varied to examine the structural and energetics effects of the size of the

1-alkyl substituent on the binding. Complementary electronic structure calculations are performed to determine the structures and energetics of the $[C_nmim]^+$ and $[BF_4]^-$ ions and their binding preferences in the ($C_nmim:BF_4$) ion pairs and $[2C_nmim:BF_4]^+$ clusters. Several levels of theory, B3LYP, B3LYP-GD3BJ, and M06-2X, using the 6-311+G(d,p) basis set for geometry optimizations and frequency analyses and the 6-311+G(2d,2p) basis set for energetics, are benchmarked to examine their abilities to properly describe the nature of the binding interactions and to reproduce the measured BDEs. The modest structural variation among these $[C_nmim]^+$ cations produces only minor structural changes and variation in the measured BDEs of the $[2C_nmim:BF_4]^+$ clusters. The BDES of the $[2C_nmim:BF_4]^+$ are determined using TCID approaches as: 120.4 ± 4.2 kJ/mol, 118.2 ± 5.0 kJ/mol, 120.9 ± 6.0 kJ/mol, and 123.0 ± 6.3 kJ/mol for the n = 2, 4, 6, and 8 clusters, respectively. The variation in the strength of binding across these $[2C_nmim:BF_4]^+$ clusters is quite small (only 4.8 ± 8.0 kJ/mol;) and of the same magnitude as the average experimental uncertainty, 5.4 ± 1.0 kJ/mol. As a result, the trends in the BDEs as a function of the $[C_nmim]^+$ cation are indistinguishable based solely on the current experimental measurements. B3LYP appears to describe the strength of binding in these clusters very well and slightly better than B3LYP-GD3BJ even though dispersion interactions should play an important role in the binding of these IL clusters. The BDEs predicted by M06-2X are systematically low, but are reasonable when BSSE corrections are not included suggesting that the high degree of parameterization of this functional may not be describing the noncovalent interactions responsible for the binding in these systems quite appropriately.

The intrinsic binding interactions in the ($C_nmim:BF_4$) ion pairs and $[2C_nmim:BF_4]^+$ clusters involve the C1′,C2, and C1″ hydrogen atoms of $[C_nmim]^+$ interacting with the fluorine atoms of $[BF_4]^-$. Coulombic and steric repulsions between the cations are evident in the 2:1 clusters as the cation-anion distances increase and only two of the fluorine atoms interact with each cation, whereas three engage in the binding in the ion pairs. Gas-phase structures reported for $[2C_2mim:BF_4]^+$ and related clusters determined using IR spectroscopy and computational approaches are consistent with those determined here. Differences in packing effects across the

$[2C_nmim{:}BF_4]^+$ cluster series are clearly minimal as both structural preferences and the strength of binding are not significantly altered. However, both B3LYP-GD3BJ and M06-2X find that the 1-alkyl substituent can fold and participate in the binding such that packing effects in larger clusters of the $C_n$mim-BF_4 ILs may lead to larger differences in their binding. Crystal structures reported for C_2mim-BF_4 exhibit further changes in structure arising from packing effects, providing additional support for this conclusion.

To definitively establish an absolute order of binding, a follow-up study of the TCID behavior of mixed $[C_{n-2}mim{:}BF_4{:}C_nmim]^+$ clusters is being pursued. Importantly, the results of this follow-up study will simultaneously provide the absolute BDEs of these mixed clusters and the absolute relative order of the intrinsic binding interactions as a function of the cation with significantly improved precision. Further, by combining the thermochemical results of the present study with those from competitive measurements, the BDEs determined for the $[2C_nmim{:}BF_4]^+$ clusters can be more accurately and precisely determined.

ASSOCIATED CONTENT

Supporting Information. Tables of CID fragments of the $[2C_nmim{:}BF_4]^+$ cluster ions; summary of structures optimized and "unique" conformers found at the B3LYP/6-311+G(d,p), B3LYP-GD3BJ/6-311+G(d,p), and M06-2X/6-311+G(d,p) levels of theory; geometric parameters, vibrational frequencies, average vibrational energies, and rotational constants of the B3LYP/6-311+G(d,p), B3LYP-GD3BJ/6-311+G(d,p), and M06-2X/6-311+G(d,p) ground conformers of the $[C_nmim]^+$ and $[BF_4]^-$ ions, ($C_nmim{:}BF_4$) ion pairs, and $[2C_nmim{:}BF_4]^+$ cluster ions; fitting parameters of eq 3 derived from fits to the $[C_nmim]^+$ product cross sections using parameters from the B3LYP-GD3BJ/6-311+G(d,p) and M06-2X/6-311+G(d,p) optimized geometries. Figures comparing CID cross sections for the $[2C_nmim{:}BF_4]^+$ clusters; description of the nomenclature used to differentiate various stable conformations of the $[C_nmim]^+$ cations, ($C_nmim{:}BF_4$) ion pairs, and $[2C_nmim{:}BF_4]^+$ cluster ions; stable B3LYP/6-311+G(2d,2p), B3LYP-GD3BJ/6-311+G(2d,2p) and M06-2X/6-311+G(2d,2p) geometry-optimized structures

and overall relative Gibbs energy distributions of the $[C_nmim]^+$ cations; binding site distributions, stable low-energy geometry-optimized structures and their relative Gibbs energies at 298K, and overall Gibbs energy distributions of the ($C_nmim:BF_4$) ion pairs and $[2C_nmim:BF_4]^+$ clusters; ESP maps of the B3LYP and M06-2X ground conformers of the ($C_nmim:BF_4$) ion pairs and $[2C_nmim:BF_4]^+$ clusters; comparisons of B3LYP computed vibrational frequencies vs B3LYP-GD3BJ and M06-2X values; zero-pressure-extrapolated CID cross sections for the $[2C_nmim:BF_4]^+$ clusters with fits to the data using eq 3; M06-2X (with and without including BSSE corrections) vs. TCID 0 K BDEs of the $[2C_nmim:BF_4]^+$ cluster ions; and B3LYP, B3LYP-GD3BJ and M06-2X (excluding BSSE corrections) 0 K BDEs vs. TCID 0 K BDEs of the $[2C_nmim:BF_4]^+$ cluster ions.

AUTHOR INFORMATION

Notes. The authors declare no competing financial interest.

ACKNOWLEDGMENTS

Financial support for this work was provided by the National Science Foundation, CHE-1709789. Computational resources were provided by Wayne State University C&IT. The authors acknowledge support from the Wayne State University Summer Dissertation Fellowship for HAR and the Thomas C. Rumble Graduate Fellowship for LAH. The authors gratefully acknowledge Zachary J. Devereaux for great feedback and editorial comments of the first draft of the manuscript.

ORCID

Harrison A. Roy https://orcid.org/0000-0002-9128-5245

Lucas A. Hamlow https://orcid.org/0000-0002-7988-5117

Mary T. Rodgers https://orcid.org/0000-0002-5614-0948

REFERENCES

(1) Walden, P., Molecular Weights and Electrical Conductivity of Several Fused Salts. *Bull. Acad. Imper. Sci.(St. Petersburg)* **1914**, *1800*, 405-422.
(2) MacFarlane, D. R.; Kar, M.; Pringle, J. M., *Fundamentals of Ionic Liquids: From Chemistry to Applications*. John Wiley & Sons: 2017.
(3) López‐Martin, I.; Burello, E.; Davey, P. N.; Seddon, K. R.; Rothenberg, G., Anion and Cation Effects on Imidazolium Salt Melting Points: A Descriptor Modelling Study. *ChemPhysChem* **2007**, *8*, 690-695.
(4) Watanabe, M.; Thomas, M. L.; Zhang, S.; Ueno, K.; Yasuda, T.; Dokko, K., Application of Ionic Liquids to Energy Storage and Conversion Materials and Devices. *Chem. Rev.* **2017**, *117*, 7190-7239.
(5) MacFarlane, D. R.; Tachikawa, N.; Forsyth, M.; Pringle, J. M.; Howlett, P. C.; Elliott, G. D.; Davis, J. H.; Watanabe, M.; Simon, P.; Angell, C. A., Energy Applications of Ionic Liquids. *Energy Environ. Sci.* **2014**, *7*, 232-250.
(6) Liu, H.; Yu, H., Ionic Liquids for Electrochemical Energy Storage Devices Applications. *J. Mater. Sci. Technol.* **2018**, *35*, 674-686.
(7) Liu, H.; Liu, Y.; Li, J., Ionic Liquids in Surface Electrochemistry. *Phys. Chem. Chem. Phys.* **2010**, *12*, 1685-1697.
(8) MacFarlane, D. R.; Forsyth, M.; Howlett, P. C.; Pringle, J. M.; Sun, J.; Annat, G.; Neil, W.; Izgorodina, E. I., Ionic Liquids in Electrochemical Devices and Processes: Managing Interfacial Electrochemistry. *Accts. Chem. Res.* **2007**, *40*, 1165-1173.
(9) Suresh; Sandhu, J. S., Recent Advances in Ionic Liquids: Green Unconventional Solvents of this Century: Part I. *Green Chem. Lett. Rev.* **2011**, *4*, 289-310.
(10) Newington, I.; Perez-Arlandis, J. M.; Welton, T., Ionic Liquids as Designer Solvents for Nucleophilic Aromatic Substitutions. *Org. Lett.* **2007**, *9*, 5247-5250.
(11) Baker, G. A.; Baker, S. N.; Pandey, S.; Bright, F. V., An Analytical View of Ionic Liquids. *Analyst* **2005**, *130*, 800-808.
(12) Sun, P.; Armstrong, D. W., Ionic Liquids in Analytical Chemistry. *Anal. Chem. Acta* **2010**, *661*, 1-16.
(13) Brown, L.; Earle, M. J.; Gîlea, M. A.; Plechkova, N. V.; Seddon, K. R., Ionic Liquid–Liquid Chromatography: A New General Purpose Separation Methodology. In *Ionic Liquids II*, Springer: 2017; pp 85-125.
(14) Soares, B.; Passos, H.; Freire, C. S.; Coutinho, J. A.; Silvestre, A. J.; Freire, M. G., Ionic Liquids in Chromatographic and Electrophoretic Techniques: Toward Additional Improvements in the Separation of Natural Compounds. *Green Chem.* **2016**, *18*, 4582-4604.
(15) Poole, C. F.; Lenca, N., Gas Chromatography on Wall-Coated Open-Tubular Columns with Ionic Liquid Stationary Phases. *J. Chromatogr. A* **2014**, *1357*, 87-109.

(16) Prince, B.; Fritz, B.; Chiu, Y., Ionic Liquids in Electrospray Propulsion Systems. *Ionic Liquids: Science and Applications* **2012**, *1117*, 27-49.
(17) Donius, B. R.; Rovey, J. L., Ionic Liquid Dual-Mode Spacecraft Propulsion Assessment. *J. Spacecraft Rockets* **2011**, *48*, 110-123.
(18) Berg, S. P.; Rovey, J. L., Assessment of Imidazole-Based Ionic Liquids as Dual-Mode Spacecraft Propellants. *J. Propul. Power.* **2013**, *29*, 339-351.
(19) Schneider, S.; Hawkins, T.; Rosander, M.; Vaghjiani, G.; Chambreau, S.; Drake, G., Ionic Liquids as Hypergolic Fuels. *Energy Fuels* **2008**, *22*, 2871-2872.
(20) Kamal, F.; Yann, B.; Rachid, B.; Charles, K., Application of Ionic Liquids to Space Propulsion. In *Applications of Ionic Liquids in Science and Technology*, Handy, S. T., Ed. InTechOpen: 2011; pp 447-466.
(21) Mier-Hicks, F.; Lozano, P. C., Spacecraft-Charging Characteristics Induced by the Operation of Electrospray Thrusters. *J. Propul. Power.* **2017**, *33*, 456-467.
(22) Demmons, N.; Hruby, V.; Spence, D.; Roy, T.; Ehrbar, E.; Zwahlen, J.; Martin, R.; Ziemer, J.; Randolph, T. In *ST7-DRS Mission Colloid Thruster Development*, 44th AIAA/ASME/SAE/ASEE Joint Propulsion Conference & Exhibit, 2008; p 4823.
(23) Sutton, G. P.; Biblarz, O., *Rocket Propulsion Elements*. 7th ed.; John Wiley & Sons: 2000; p 160-196, 241-267.
(24) Dong, Q.; Muzny, C. D.; Kazakov, A.; Diky, V.; Magee, J. W.; Widegren, J. A.; Chirico, R. D.; Marsh, K. N.; Frenkel, M., ILThermo: A Free-Access Web Database for Thermodynamic Properties of Ionic Liquids. *J. Chem. Eng. Data* **2007**, *52*, 1151-1159.
(25) Voss, J. M.; Marsh, B. M.; Zhou, J.; Garand, E., Interaction Between Ionic Liquid Cation and Water: Infrared Predissociation Study of $[bmim]^+ \cdot (H_2O)_n$ Clusters. *Phys. Chem. Chem. Phys.* **2016**, *18*, 18905-18913.
(26) Patrick, A. L., Electrospray Ionization Enters the Final Frontier: Mass Spectrometry's Role in Understanding Electrospray Thrusters and Their Plumes. *Rapid Commun. Mass Spectrom.* **2020**, *34*, e8587.
(27) Patrick, A. L.; Vogelhuber, K. M.; Prince, B. D.; Annesley, C. J., Theoretical and Experimental Insights into the Dissociation of 2-Hydroxyethylhydrazinium Nitrate Clusters Formed via Electrospray. *J. Phys. Chem. A* **2018**, *122*, 1960-1966.
(28) De Silva, M.; Brown, A. C.; Patrick, A. L., Thermal- and Collision-Induced Dissociation Studies of Functionalized Imidazolium-Based Ionic Liquid Cations. *J. Mass Spectrom.* **2020**, *55*, e4518.
(29) Zhang, J.; Baxter, E.; Nguyen, M.-T.; Prabhakaran, V.; Rousseau, R.; Johnson, G. E.; Glezakou, V.-A., Structure and Stability of the Ionic Liquid Clusters $[EMIM]_n[BF4]_{n+1}^-$ (n = 1-9): Implications for Electrochemical Separations. *J. Phys. Chem. Lett.* **2020**.
(30) Bini, R.; Bortolini, O.; Chiappe, C.; Pieraccini, D.; Siciliano, T., Development of Cation/Anion “Interaction” Scales for Ionic Liquids Through ESI-MS Measurements. *J. Phys. Chem. B* **2007**, *111*, 598-604.

(31) Gozzo, F. C.; Santos, L. S.; Augusti, R.; Consorti, C. S.; Dupont, J.; Eberlin, M. N., Gaseous Supramolecules of Imidazolium Ionic Liquids: "Magic" Numbers and Intrinsic Strengths of Hydrogen Bonds. *Chem. Eur. J.* **2004**, *10*, 6187-6193.
(32) Vitorino, J.; Leal, J. P.; Minas da Piedade, M. E., Gas-Phase Affinity Scales for Typical Ionic Liquid Moieties Determined by using Cooks' Kinetic Method. *ChemPhysChem* **2015**, *16*, 1969-1977.
(33) Fernandes, A. M.; Coutinho, J. A.; Marrucho, I. M., Gas-Phase Dissociation of Ionic Liquid Aggregates Studied by Electrospray Ionisation Mass Spectrometry and Energy-Variable Collision Induced Dissociation. *J. Mass Spectrom.* **2009**, *44*, 144-150.
(34) Hogan, C. J.; De la Mora, J. F., Ion-Pair Evaporation from Ionic Liquid Clusters. *J. Am. Soc. Mass Spectrom.* **2010**, *21*, 1382-1386.
(35) Hogan Jr, C. J.; De La Mora, J. F., Tandem Ion Mobility-Mass Spectrometry (IMS-MS) Study of Ion Evaporation from Ionic Liquid-Acetonitrile Nanodrops. *Phys. Chem. Chem. Phys.* **2009**, *11*, 8079-8090.
(36) Ku, B. K.; Fernandez de la Mora, J., Cluster Ion Formation in Electrosprays of Acetonitrile Seeded with Ionic Liquids. *J. Phys. Chem. B* **2004**, *108*, 14915-14923.
(37) Rus, J.; Moro, D.; Sillero, J. A.; Royuela, J.; Casado, A.; Estevez-Molinero, F.; de la Mora, J. F., IMS–MS Studies Based on Coupling a Differential Mobility Analyzer (DMA) to Commercial API–MS Systems. *Int. J. Mass Spectrom.* **2010**, *298*, 30-40.
(38) Johnson, C. J.; Fournier, J. A.; Wolke, C. T.; Johnson, M. A., Ionic Liquids from the Bottom Up: Local Assembly Motifs in [EMIM][BF_4] through Cryogenic Ion Spectroscopy. *J. Chem. Phys.* **2013**, *139*, 224305.
(39) Fournier, J. A.; Wolke, C. T.; Johnson, C. J.; McCoy, A. B.; Johnson, M. A., Comparison of the Local Binding Motifs in the Imidazolium-Based Ionic Liquids [EMIM][BF_4] and [EMMIM][BF_4] Through Cryogenic Ion Vibrational Predissociation Spectroscopy: Unraveling the Roles of Anharmonicity and Intermolecular Interactions. *J. Chem. Phys.* **2015**, *142*, 064306.
(40) Cooper, R.; Zolot, A. M.; Boatz, J. A.; Sporleder, D. P.; Stearns, J. A., IR and UV Spectroscopy of Vapor-Phase Jet-Cooled Ionic Liquid $[emim]^+[Tf_2N]^-$: Ion Pair Structure and Photodissociation Dynamics. *J. Phys. Chem. A* **2013**, *117*, 12419-12428.
(41) Booth, R. S.; Annesley, C. J.; Young, J. W.; Vogelhuber, K. M.; Boatz, J. A.; Stearns, J. A., Identification of Multiple Conformers of the Ionic Liquid [EMIM][Tf_2N] in the Gas Phase Using IR/UV Action Spectroscopy. *Phys. Chem. Chem. Phys.* **2016**, *18*, 17037-17043.
(42) Yamada, T.; Tominari, Y.; Tanaka, S.; Mizuno, M., Terahertz and Infrared Spectroscopy of Room-Temperature Imidazolium-Based Ionic Liquids. *J. Phys. Chem. B* **2015**, *119*, 15696-15705.
(43) Heimer, N. E.; Del Sesto, R. E.; Meng, Z.; Wilkes, J. S.; Carper, W. R., Vibrational Spectra of Imidazolium Tetrafluoroborate Ionic Liquids. *J. Mol. Liq.* **2006**, *124*, 84-95.

(44) Holomb, R.; Martinelli, A.; Albinsson, I.; Lassegues, J.-C.; Johansson, P.; Jacobsson, P., Ionic Liquid Structure: the Conformational Isomerism in 1-Butyl-3-Methyl-Imidazolium Tetrafluoroborate ([bmim][BF4]). *J. Raman Spectrosc.* **2008**, *39*, 793-805.
(45) Tsuzuki, S.; Tokuda, H.; Hayamizu, K.; Watanabe, M., Magnitude and Directionality of Interaction in Ion Pairs of Ionic Liquids: Relationship with Ionic Conductivity. *J. Phys. Chem. B* **2005**, *109*, 16474-16481.
(46) Katsyuba, S. A.; Zvereva, E. E.; Vidiš, A.; Dyson, P. J., Application of Density Functional Theory and Vibrational Spectroscopy Toward the Rational Design of Ionic Liquids. *J. Phys. Chem. A* **2007**, *111*, 352-370.
(47) Izgorodina, E. I.; Maganti, R.; Armel, V.; Dean, P. M.; Pringle, J. M.; Seddon, K. R.; MacFarlane, D. R., Understanding the Effect of the C2 Proton in Promoting Low Viscosities and High Conductivities in Imidazolium-Based Ionic Liquids: Part I. Weakly Coordinating Anions. *J. Phys. Chem. B* **2011**, *115*, 14688-14697.
(48) Bonhote, P.; Dias, A.-P.; Papageorgiou, N.; Kalyanasundaram, K.; Grätzel, M., Hydrophobic, Highly Conductive Ambient-Temperature Molten Salts. *Inorg. Chem.* **1996**, *35*, 1168-1178.
(49) Strehmel, V.; Laschewsky, A.; Wetzel, H.; Görnitz, E., Free Radical Polymerization of n-Butyl Methacrylate in Ionic Liquids. *Macromolecules* **2006**, *39*, 923-930.
(50) Zahn, S.; Bruns, G.; Thar, J.; Kirchner, B., What Keeps Ionic Liquids in Flow? *Phys. Chem. Chem. Phys.* **2008**, *10*, 6921-6924.
(51) Becke, A. D., Density-Functional Thermochemistry. III. The Role of Exact Exchange. *J. Chem. Phys.* **1993**, *98*, 5648-5652.
(52) Lee, C.; Yang, W.; Parr, R. G., Development of the Colle-Salvetti Correlation-Energy Formula into a Functional of the Electron Density. *Phys. Rev. B* **1988**, *37*, 785-789.
(53) Grimme, S.; Ehrlich, S.; Goerigk, L., Effect of the Damping Function in Dispersion Corrected Density Functional Theory. *J. Comput. Chem.* **2011**, *32*, 1456-1465.
(54) Zhao, Y.; Truhlar, D. G., The M06 Suite of Density Functionals for Main Group Thermochemistry, Thermochemical Kinetics, Noncovalent Interactions, Excited States, and Transition Elements: Two New Functionals and Systematic Testing of Four M06-Class Functionals and 12 Other Functionals. *Theor. Chem. Acc.* **2008**, *120*, 215-241.
(55) Rodgers, M. T., Substituent Effects in the Binding of Alkali Metal Ions to Pyridines Studied by Threshold Collision-Induced Dissociation and Ab Initio Theory: The Methylpyridines. *J. Phys. Chem. A* **2001**, *105*, 2374-2383.
(56) Chen, Y.; Rodgers, M. T., Structural and Energetic Effects in the Molecular Recognition of Protonated Peptidomimetic Bases by 18-Crown-6. *J. Am. Chem. Soc.* **2012**, *134*, 2313-2324.
(57) Moision, R.; Armentrout, P., An Electrospray Ionization Source for Thermochemical Investigation with the Guided Ion Beam Mass Spectrometer. *J. Am. Soc. Mass Spectrom.* **2007**, *18*, 1124–1134.

(58) Teloy, E.; Gerlich, D., Integral Cross Sections for Ion-Molecule Reactions. 1. The Guided Beam Technique. *Chem. Phys.* **1974**, *4*, 417-427.
(59) Gerlich, D., Inhomogeneous RF Fields: A Versatile Tool for the Study of Processes with Slow Ions. *Adv. Chem. Phys.* **1992**, *82*, 1-176.
(60) Daly, N. R., Scintillation Type Mass Spectrometer Ion Detector. *Rev. Sci. Instrum.* **1960**, *31*, 264-267.
(61) Khan, F. A.; Clemmer, D. E.; Schultz, R. H.; Armentrout, P. B., Sequential Bond Energies of $Cr(CO)_x^+$, $x = 1 - 6$. *J. Phys. Chem.* **1993**, *97*, 7978-7987.
(62) Rodgers, M. T.; Ervin, K. M.; Armentrout, P. B., Statistical Modeling of Collision-Induced Dissociation Thresholds. *J. Chem. Phys.* **1997**, *106*, 4499-4508.
(63) Wolinski, K.; Hinton, J.; Wishart, D.; Sykes, B.; Richards, F.; Pastone, A.; Saudek, V.; Ellis, P.; Maciel, G.; McIver, J., HyperChem Computational Chemistry Software Package, Version 8.0. Hypercube, Inc., Gainsville, FL: 2004.
(64) Bertsimas, D.; Tsitsiklis, J., Simulated Annealing. *Stat. Sci.* **1993**, *8*, 10-15.
(65) Cramer, C. J., *Essentials of Computational Chemistry: Theories and Models*. John Wiley & Sons: 2013.
(66) Cornell, W. D.; Cieplak, P.; Bayly, C. I.; Gould, I. R.; Merz, K. M.; Ferguson, D. M.; Spellmeyer, D. C.; Fox, T.; Caldwell, J. W.; Kollman, P. A., A Second Generation Force Field for the Simulation of Proteins, Nucleic Acids, and Organic Molecules. *J. Am. Chem. Soc.* **1995**, *117*, 5179-5197.
(67) Frisch, M. J.; Trucks, G. W.; Schlegel, H. B.; Scuseria, G. E.; Robb, M. A.; Cheeseman, J. R.; Scalmani, G.; Barone, V.; Mennucci, B.; Petersson, G. A., et al., *Gaussian 09*, revision C.01; Gaussian, Inc.: Wallingford, CT, 2009.
(68) Sousa, S. F.; Fernandes, P. A.; Ramos, M. J., General Performance of Density Functionals. *J. Phys. Chem. A* **2007**, *111*, 10439-10452.
(69) Tirado-Rives, J.; Jorgensen, W. L., Performance of B3LYP Density Functional Methods for a Large Set of Organic Molecules. *J. Chem. Theory Comput.* **2008**, *4*, 297-306.
(70) Simon, S.; Duran, M.; Dannenberg, J., How Does Basis Set Superposition Error Change the Potential Surfaces for Hydrogen-Bonded Dimers? *J. Chem. Phys.* **1996**, *105*, 11024-11031.
(71) Boys, S. F.; Bernardi, R., The Calculation of Small Molecular Interactions by the Differences of Separate Total Energies. Some Procedures with Reduced Errors. *Mol. Phys.* **1970**, *19*, 553-566.
(72) Smith, S. M.; Markevitch, A. N.; Romanor, D. A.; Li, X.; Levis, R. J.; Schlegel, H. B., Static and Dynamic Polarizabilities of Conjugated Molecules and Their Cations *J. Phys. Chem. A* **2000**, *108*, 11063-11072.
(73) Contreras-García, J.; Johnson, E. R.; Keinan, S.; Chaudret, R.; Piquemal, J.-P.; Beratan, D. N.; Yang, W., NCIPLOT: A Program for Plotting Noncovalent Interaction Regions. *J. Chem. Theory Comput.* **2011**, *7*, 625-632.

(74) Johnson, E. R.; Keinan, S.; Mori-Sánchez, P.; Contreras-García, J.; Cohen, A. J.; Yang, W., Revealing Noncovalent Interactions. *J. Am. Chem. Soc.* **2010**, *132*, 6498-6506.
(75) Humphrey, W.; Dalke, A.; Schulten, K., VMD: Visual Molecular Dynamics. *J. Mol. Graph.* **1996**, *14*, 33-38.
(76) Ervin, K. M.; Armentrout, P. B., Translational Energy Dependence of $Ar^+ + XY \rightarrow ArX^+ + Y$ ($XY = H_2, D_2, HD$) from Thermal to 30 eV c.m. *J. Chem. Phys.* **1985**, *83*, 166-189.
(77) Dalleska, N. F.; Honma, K.; Armentrout, P. B., Stepwise Solvation Enthalpies of Protonated Water Clusters: Collision-Induced Dissociation as an Alternative to Equilibrium Studies. *J. Am. Chem. Soc.* **1993**, *115*, 12125-12131.
(78) Rodgers, M. T.; Armentrout, P. B., Statistical Modeling of Competitive Threshold Collision-Induced Dissociation. *J. Chem. Phys.* **1998**, *109*, 1787-1800.
(79) Beyer, T. S.; Swinehart, D. F., Number of Multiply-Restricted Partitions. *Commun. ACM* **1973**, *16*, 379.
(80) Merrick, J. P.; Moran, D.; Radom, L., An Evaluation of Harmonic Vibrational Frequency Scale Factors. *J. Phys. Chem. A* **2007**, *111*, 11683–11700.
(81) Rannulu, N. S.; Rodgers, M. T., Noncovalent Interactions of Cu^+ with N-Donor Ligands (Pyridine, 4,4-Dipyridyl, 2,2-Dipyridyl, and 1,10-Phenanthroline): Collision-Induced Dissociation and Theoretical Studies. *J. Phys. Chem. A* **2007**, *111*, 3465-3479.
(82) Hallowita, N.; Carl, D. R.; Armentrout, P. B.; Rodgers, M. T., Dipole Effects on Cation-π Interactions: Absolute Bond Dissociation Energies of Complexes of Alkali Metal Cations to N-methylaniline and N,N-dimethylaniline. *J. Phys. Chem. A* **2008**, *112*, 7996–8008.
(83) Vitale, G.; Valina, A. B.; Huang, H.; Amunugama, R.; Rodgers, M. T., Solvation of Copper Ions by Acetonitrile. Structures and Sequential Binding Energies of $Cu^+(CH_3CN)_x$, x =1-5 from Collision-Induced Dissociation and Theoretical Studies. *J. Phys. Chem. A* **2001**, *105*, 11351-11364.
(84) Ruan, C.; Yang, Z.; Rodgers, M., Influence of the d Orbital Occupation on the Nature and Strength of Copper Cation–π Interactions: Threshold Collision-Induced Dissociation and Theoretical Studies. *Phys. Chem. Chem. Phys.* **2007**, *9*, 5902-5918.
(85) Rannulu, N. S.; Amunugama, R.; Yang, Z.; Rodgers, M. T., Influence of s and d Orbital Occupation on the Binding of Metal Ions to Imidazole. *J. Phys. Chem. A* **2004**, *108*, 6385-6396.
(86) Ruan, C.; Rodgers, M. T., Cation-π Interactions: Structures and Energetics of Complexation of Na^+ and K^+ with the Aromatic Amino Acids, Phenylalanine, Tyrosine and Tryptophan. *J. Am. Chem. Soc.* **2004**, *126*, 14600-14610.
(87) Huang, H.; Rodgers, M. T., Sigma versus Pi Interactions in Alkali Metal Ion Binding Affinities of Azoles: Threshold Collision-Induced Dissociation and Ab Initio Theory Studies. *J. Phys. Chem. A* **2002**, *106*, 4277-4289.
(88) Rodgers, M. T.; Armentrout, P. B., Absolute Alkali Metal Ion Binding Affinities of Several Azoles Determined by Threshold Collision-Induced Dissociation. *Int. J. Mass Spectrom.* **1999**, *185/186/187*, 359-380.

(89) Ruan, C.; Yang, Z.; Hallowita, N.; Rodgers, M. T., Cation-π Interactions with a Model for the Side Chain of Tryptophan: Structures and Absolute Binding Energies of Alkali Metal Cation-Indole Complexes. *J. Phys. Chem. A* **2005**, *109*, 11539-11550.
(90) Lifshitz, C., Recent Developments in Applications of RRKM-QET. *Adv. Mass Spectrom.* **1989**, *11*, 713-729.
(91) Mudring, A.-V., Solidification of Ionic Liquids: Theory and Techniques. *Aust. J. Chem.* **2010**, *63*, 544-564.
(92) Choudhury, A. R.; Winterton, N.; Steiner, A.; Cooper, A. I.; Johnson, K. A., In Situ Crystallization of Low-Melting Ionic Liquids. *J. Am. Chem. Soc.* **2005**, *127*, 16792-16793.
(93) Mehta, N. A.; Levin, D. A., Molecular Dynamics Electrospray Simulations of Coarse-Grained Ethylammonium Nitrate (EAN) and 1-Ethyl-3-Methylimidazolium Tetrafluoroborate (EMIM-BF_4). *Aerospace* **2018**, *5*, 1.
(94) Borner, A.; Li, Z.; Levin, D. A., Modeling of an Ionic Liquid Electrospray Using Molecular Dynamics with Constraints. *J. Chem. Phys.* **2012**, *136*, 124507.
(95) Daily, J. W., Molecular Dynamics Simulation of Ion Emission from Nanodroplets of Ionic Liquids. *J. Propul. Power.* **2008**, *24*, 981-986.
(96) Prince, B. D.; Tiruppathi, P.; Bemish, R. J.; Chiu, Y.-H.; Maginn, E. J., Molecular Dynamics Simulations of 1-Ethyl-3-methylimidazolium Bis[(trifluoromethyl)sulfonyl]imide Clusters and Nanodrops. *J. Phys. Chem. A* **2015**, *119*, 352-368.

Table 1. Fitting Parameters of eq 3, Threshold Dissociation Energies at 0 K, and Entropies of Activation at 1000 K of $[2C_nmim:BF_4]^+$ Clusters.[a]

Cluster	σ^b	n^b	$E_0{}^c$ (eV)	$E_0(PSL)^b$ (eV)	Kinetic Shift (eV)	$\Delta S^{\ddagger}$ (PSL)^b (J mol^{-1} K^{-1})
$[2C_2mim:BF_4]^+$	104.8 (4.4)	0.93 (0.02)	1.95 (0.06)	1.25 (0.04)	0.70	21 (5)
$[2C_4mim:BF_4]^+$	81.6 (1.6)	0.95 (0.02)	2.24 (0.05)	1.23 (0.05)	1.01	18 (4)
$[2C_6mim:BF_4]^+$	93.4 (2.8)	1.2 (0.03)	2.46 (0.08)	1.25 (0.06)	1.21	40 (4)
$[2C_8mim:BF_4]^+$	99.0 (4.5)	1.3 (0.03)	2.83 (0.09)	1.27 (0.07)	1.55	47 (4)

[a]Average values obtained for fits to the $[C_nmim]^+$ product cross section based on parameters derived from the B3LYP/6-311+G(d,p) optimized structures. Uncertainties are listed in parentheses. [b]Average values for a loose PSL TS. [c]No RRKM analysis.

Table 2. Enthalpies and Free Energies of Binding of $[2C_nmim:BF_4]^+$ Clusters at 0 and 298 K in kJ/mol.[a]

Cluster	ΔH_0	$\Delta H_0{}^b$	$\Delta H_{298} - \Delta H_0{}^b$	ΔH_{298}	$\Delta H_{298}{}^b$	$T\Delta S_{298}{}^b$	ΔG_{298}	$\Delta G_{298}{}^b$
$[2C_2mim:BF_4]^+$	120.4 (4.2)	121.4	-3.7 (0.1)	116.7 (3.9)	117.8	34.5 (1.5)	82.3 (4.2)	83.5
$[2C_4mim:BF_4]^+$	118.2 (5.0)	117.8	-3.8 (0.1)	114.4 (5.0)	114.0	33.1 (1.5)	81.2 (5.2)	81.0
$[2C_6mim:BF_4]^+$	120.9 (6.0)	118.6	-3.3 (0.1)	117.6 (6.0)	115.3	39.3 (1.5)	78.3 (6.2)	76.1
$[2C_8mim:BF_4]^+$	123.0 (6.3)	119.5	-4.2 (0.1)	118.8 (6.3)	115.3	40.7 (1.5)	78.1 (6.5)	74.7

[a]Values are given in kJ/mol. Uncertainties are listed in parentheses. [b]Density functional theory values from calculations at the B3LYP/6-311+G(2d,2p)//B3LYP/6-311+G(d,p) level of theory including BSSE corrections and with frequencies scaled by 0.9887.

Table 3. Bond Dissociation Energies of the $[2C_nmim:BF_4]^+$ Clusters at 0 K.[a]

Cluster	TCID	B3LYP[b]		B3LYP-GD3BJ[c]		M06-2X[d]	
		D_0	$D_{0,BSSE}{}^e$	D_0	$D_{0,BSSE}{}^e$	D_0	$D_{0,BSSE}{}^e$
$[2C_2mim:BF_4]^+$	120.4 (4.2)	125.5	121.4	128.4	124.1	119.5	112.5
$[2C_4mim:BF_4]^+$	118.2 (5.0)	122.1	117.8	121.4	116.8	115.2[f]	108.8[f]
$[2C_6mim:BF_4]^+$	120.9 (6.0)	122.8	118.6	126.6	120.2	121.5	112.9
$[2C_8mim:BF_4]^+$	123.0 (6.3)	123.7	119.5	130.1	124.9	111.5	103.2
AEU/MAD[g]	5.4 (1.0)	2.9 (2.0)	1.8 (1.4)	6.0 (2.1)	1.9 (1.3)	4.0 (5.1)	11.3 (5.7)

[a]Values are given in kJ/mol. Uncertainties are listed in parentheses. [b]Calculated at the B3LYP/6-311+G(2d,2p) level of theory using B3LYP/6-311+G(d,p) optimized geometries including ZPE corrections. [c]Calculated at the B3LYP-GD3BJ/6-311+G(2d,2p) level of theory using B3LYP-GD3BJ/6-311+G(d,p) optimized geometries including ZPE corrections. [d]Calculated at the M06-2X/6-311+G(2d,2p) level of theory using M06-2X/6-311+G(d,p) optimized geometries including ZPE corrections. [e]Also includes BSSE corrections. [f]Calculations were performed using an ultrafine integral grid. [g]Average experimental uncertainty (AEU) and mean absolute deviation (MAD) between the measured and calculated values.

Figure Captions

Figure 1. Chemical structures of the $[C_nmim]^+$ cations and the $[BF_4]^-$ anion. The atom numbering of the cations is shown.

Figure 2. Cross sections for collision-induced dissociation of the $[2C_4mim{:}BF_4]^+$ IL cluster with Xe as a function of collision energy in the center-of-mass frame (lower *x*-axis) and laboratory frame (upper *x*-axis). The data shown was acquired at a Xe pressure of ~ 0.2 mTorr. Ionic product legend: $[C_4mim]^+$ (●), $[C_4H_7N_2]^+$ (□), $[C_4H_9]^+$ (△), $[C_3H_7]^+$ (○), and $[C_2H_5]^+$ (◇).

Figure 3. Overlay and expanded view of the $[C_nmim]^+$ primary CID product cross sections of the $[2C_nmim{:}BF_4]^+$ IL clusters, where n = 2, 4, 6, and 8 as a function of the center-of-mass collision energy. The data shown were acquired at a Xe pressure of ~ 0.2 mTorr.

Figure 4. Noncovalent interaction maps superimposed on the B3LYP/6-311+G(d,p) and M06-2X/6-311+G(d,p) optimized geometries of the ground conformers of the $[C_nmim]^+$ cations and $[BF_4]^-$ anion.

Figure 5. Electrostatic potential maps superimposed on the B3LYP/6-311+G(d,p) and M06-2X/6-311+G(d,p) ground conformers of the $[C_nmim]^+$ cations and the $[BF_4]^-$ anion.

Figure 6. Noncovalent interaction maps superimposed on the B3LYP/6-311+G(d,p) and M06-2X/6-311+G(d,p) optimized geometries of the ground conformers of the $(C_nmim{:}BF_4)$ ion pairs.

Figure 7. Noncovalent interaction maps superimposed on the B3LYP/6-311+G(d,p) and M06-2X/6-311+G(d,p) optimized geometries of the ground conformers of the $[2C_nmim:BF_4]^+$ IL clusters.

Figure 8. Zero-pressure-extrapolated cross section for collision-induced dissociation of the $[2C_4mim:BF_4]^+$ IL cluster with Xe as a function of the collision energy in the center-of-mass frame (lower *x*-axis) and laboratory frame (upper *x*-axis). The solid lines show the best fit to the data convoluted over the neutral and ion kinetic and internal energy distributions. The dashed line shows the model cross sections in the absence of experimental kinetic energy broadening for reactants with an internal energy corresponding to 0 K.

Figure 9. Comparison of B3LYP, B3LYP-GD3BJ, and M06-2X computed 0 K BDEs versus measured threshold dissociation energies of the $[2C_nmim:BF_4]^+$ IL clusters for n = 2, 4, 6, and 8. The diagonal line indicates values for which the calculated and measured values are equal.

Figure 1.

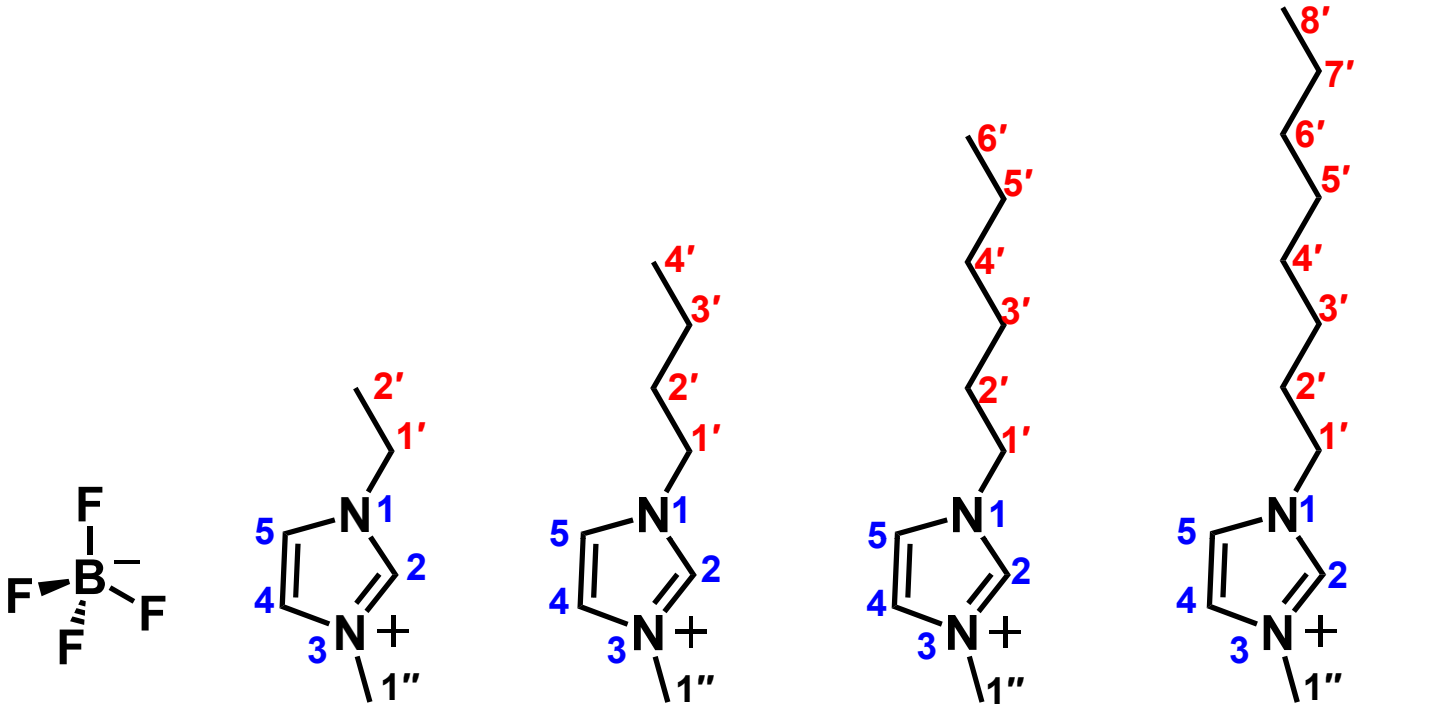

$[BF_4]^-$ $[C_2mim]^+$ $[C_4mim]^+$ $[C_6mim]^+$ $[C_8mim]^+$

Figure 2.

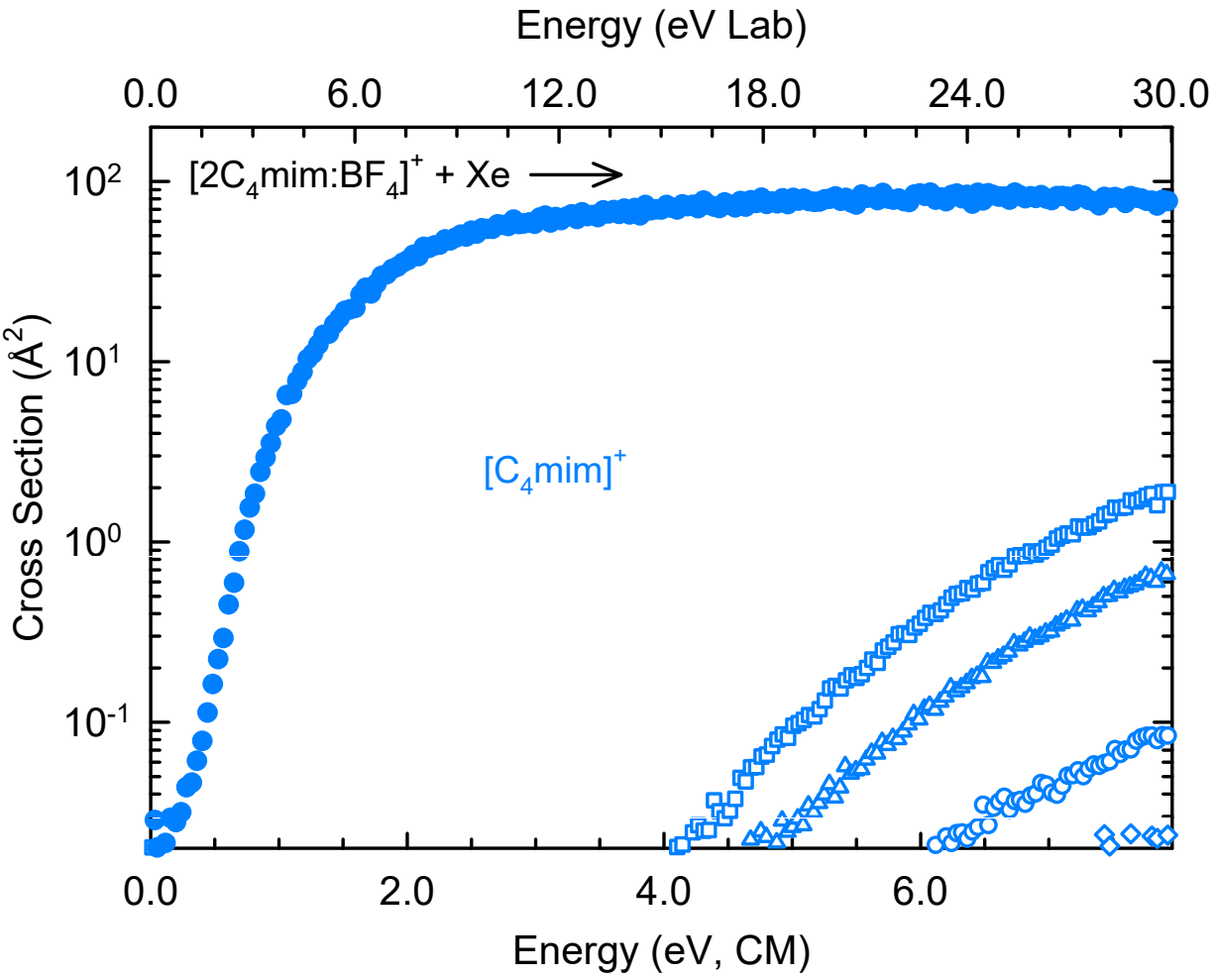
Energy (eV Lab)
0.0
6.0
12.0
18.0
24.0
30.0
[2C4mim:BF4]+ + Xe
[C4mim]+
Cross Section (Å2)
10^2
10^1
10^0
10^-1
0.0
2.0
4.0
6.0
Energy (eV, CM)

Figure 3.

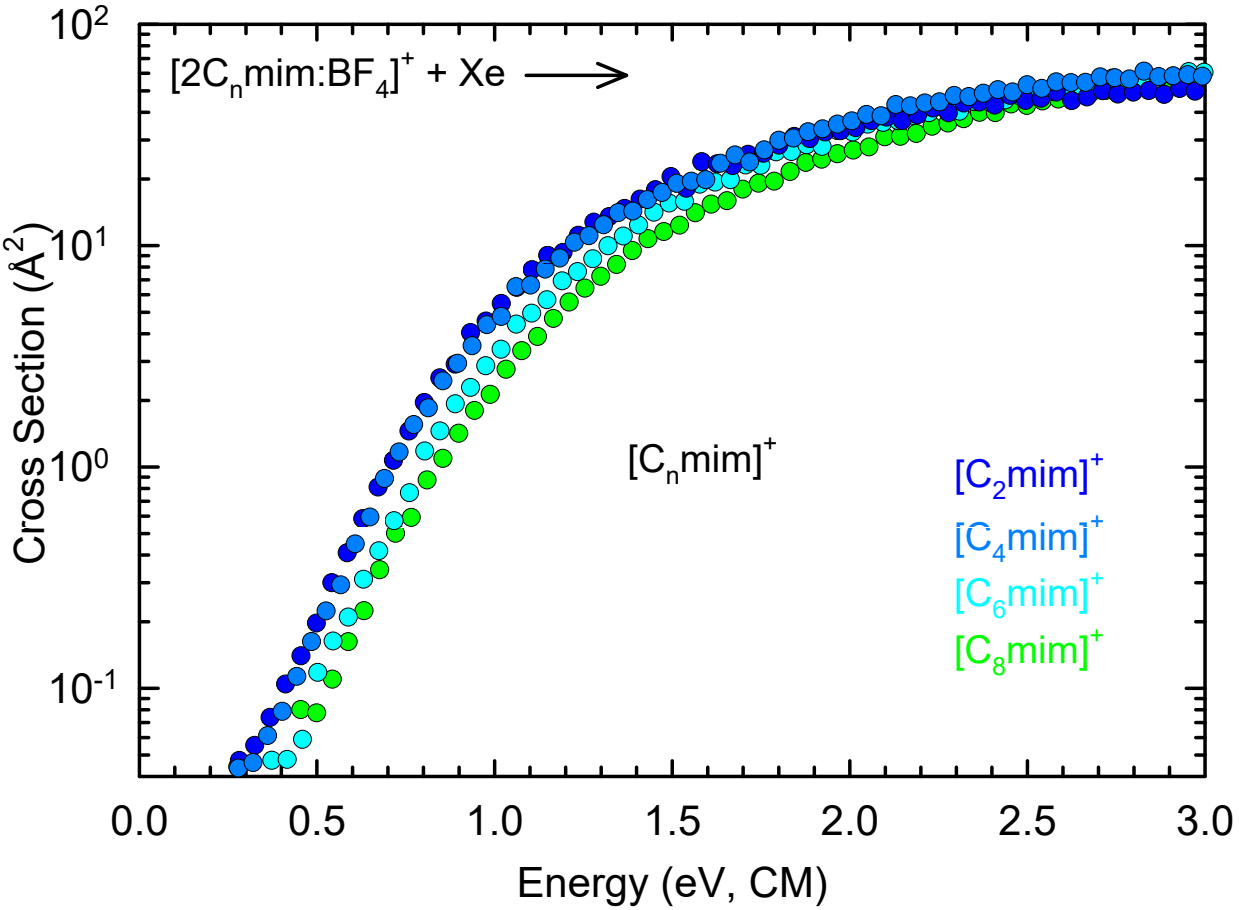
[2C$_n$mim:BF$_4$]$^+$ + Xe
[C$_n$mim]$^+$
[C$_2$mim]$^+$
[C$_4$mim]$^+$
[C$_6$mim]$^+$
[C$_8$mim]$^+$
Cross Section (Å^2)
Energy (eV, CM)
10^2
10^1
10^0
10^{-1}
0.0
0.5
1.0
1.5
2.0
2.5
3.0

Figure 4.

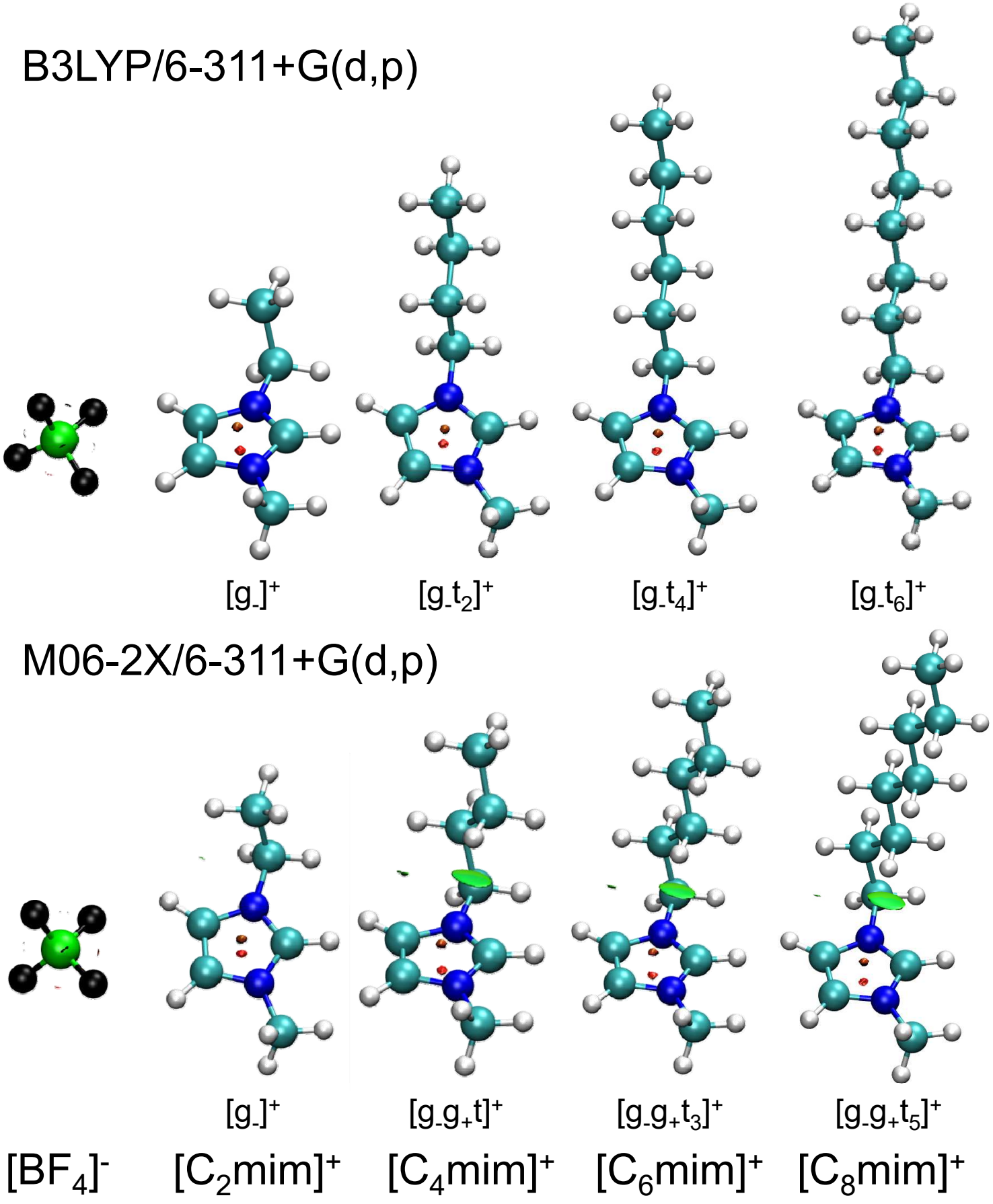
B3LYP/6-311+G(d,p)
[g-]+
[g-t2]+
[g-t4]+
[g-t6]+
M06-2X/6-311+G(d,p)
[g-]+
[g-g+t]+
[g-g+t3]+
[g-g+t5]+
[BF4]-
[C2mim]+
[C4mim]+
[C6mim]+
[C8mim]+

Figure 5.

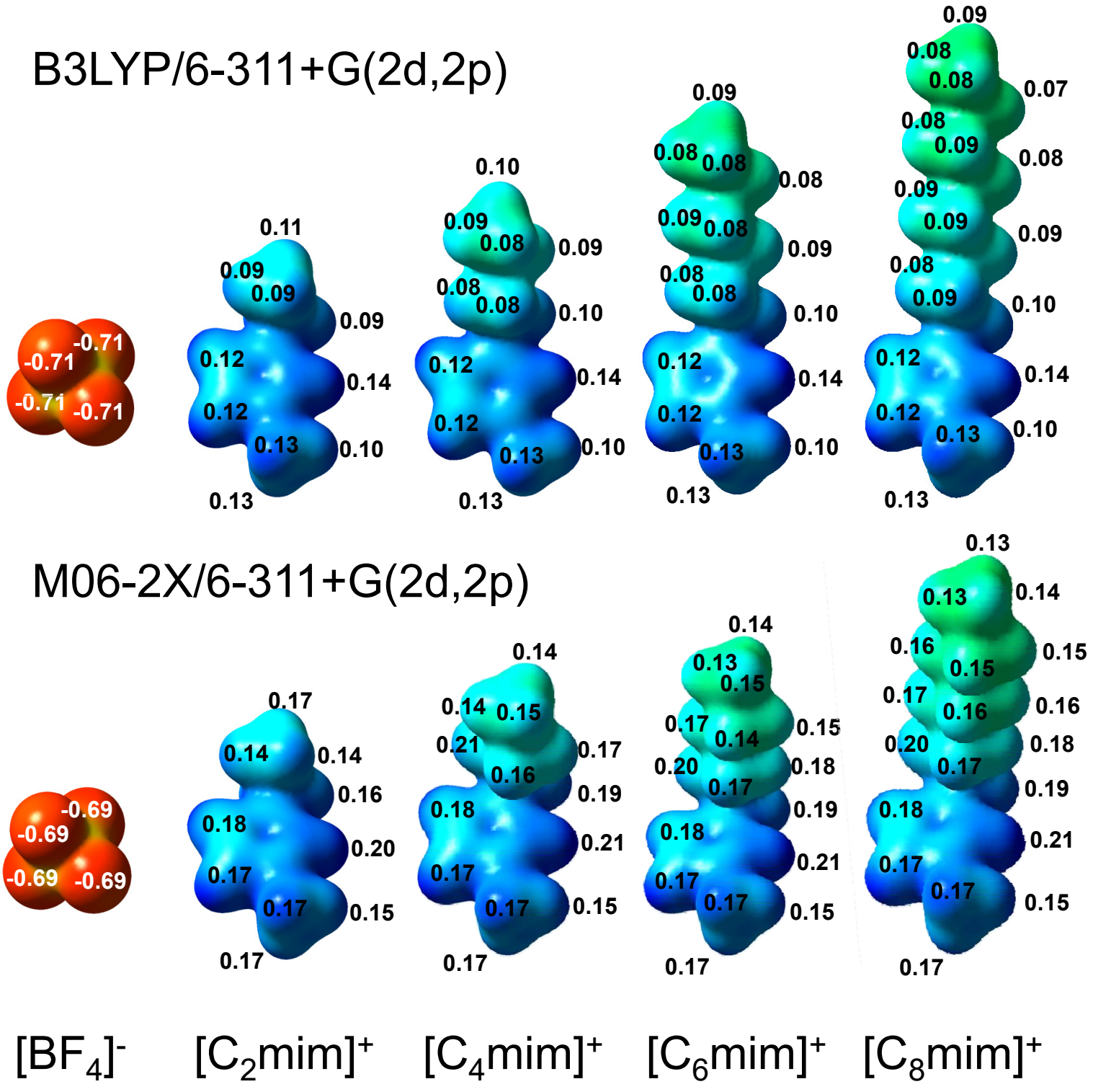
B3LYP/6-311+G(2d,2p)
-0.71
-0.71
-0.71
-0.71
0.11
0.09
0.09
0.09
0.12
0.14
0.12
0.13
0.10
0.13
0.10
0.09
0.08
0.09
0.08
0.08
0.10
0.12
0.14
0.12
0.13
0.10
0.13
0.09
0.08
0.08
0.08
0.09
0.09
0.08
0.08
0.10
0.12
0.14
0.12
0.13
0.10
0.13
0.09
0.08
0.08
0.07
0.08
0.09
0.08
0.09
0.09
0.08
0.09
0.09
0.08
0.10
0.12
0.14
0.12
0.13
0.10
0.13
M06-2X/6-311+G(2d,2p)
-0.69
-0.69
-0.69
-0.69
0.17
0.14
0.14
0.16
0.18
0.20
0.17
0.17
0.15
0.17
0.14
0.14
0.15
0.21
0.17
0.16
0.19
0.18
0.21
0.17
0.17
0.15
0.17
0.14
0.13
0.15
0.17
0.14
0.15
0.20
0.18
0.17
0.19
0.18
0.21
0.17
0.17
0.15
0.17
0.13
0.13
0.14
0.16
0.15
0.15
0.17
0.16
0.16
0.20
0.18
0.17
0.19
0.18
0.21
0.17
0.17
0.15
0.17
[BF4]-
[C2mim]+
[C4mim]+
[C6mim]+
[C8mim]+
-0.25
+0.28

Figure 6.

B3LYP/6-311+G(d,p)

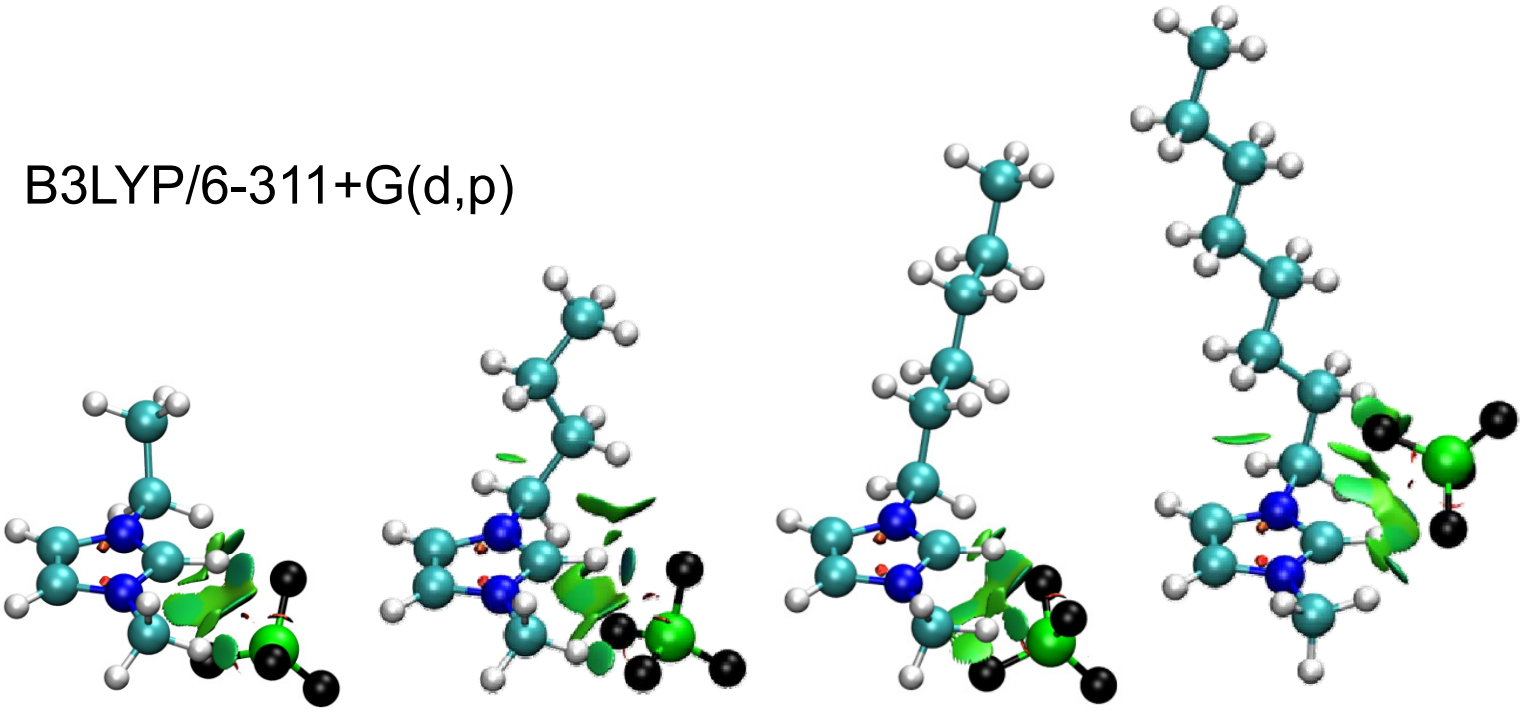

($\mathbf{g_+F}$;g_-) ($\mathbf{g_+F}$;$g_{-2}t$) ($\mathbf{cF}$;g_-t_4) ($\mathbf{cF}$;$g_{-2}t_5$)

(C_2mim:BF_4) (C_4mim:BF_4) (C_6mim:BF_4) (C_8mim:BF_4)

($\mathbf{g_-F}$;g_-) ($\mathbf{g_+F}$;cg_-t) ($\mathbf{g_-F}$;g_-t_4) ($\mathbf{g_-F}$;$g_-t_2g_{+2}t_2$)

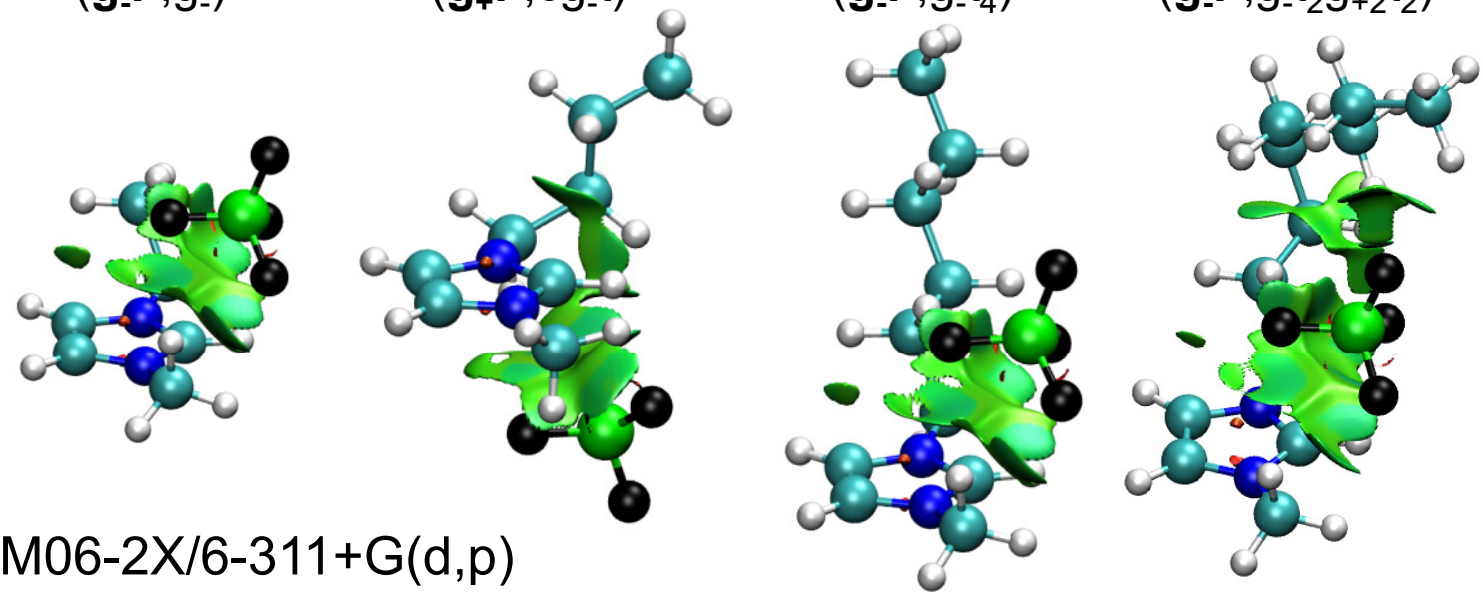

M06-2X/6-311+G(d,p)

Figure 7.

B3LYP/6-311+G(d,p)

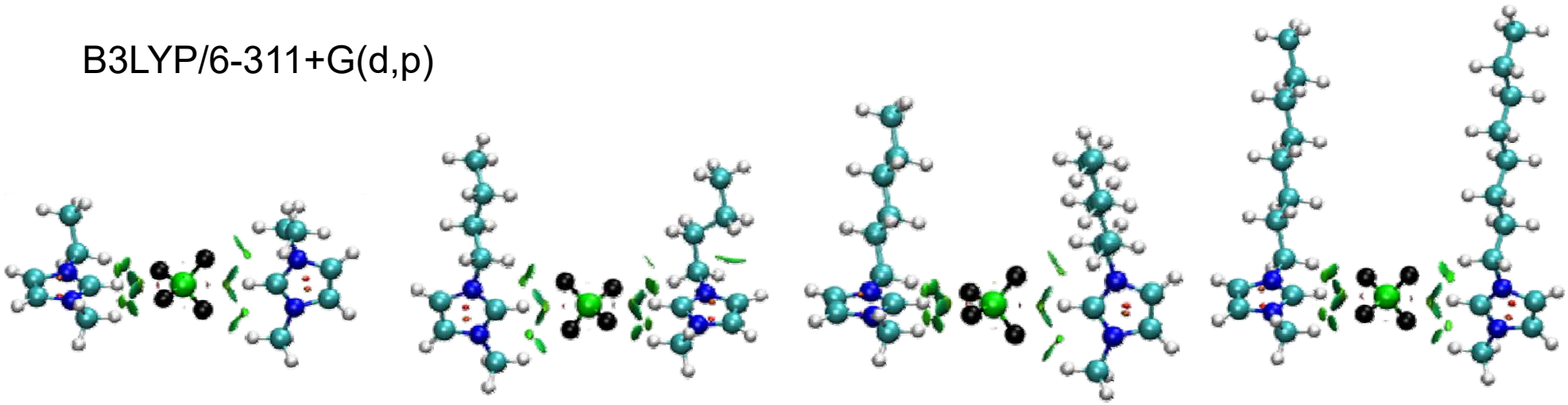

$[g_+;\mathbf{g_+cFcF};g_-]^+$ $[g_{+2}t;\mathbf{g_-cFcF};g_+t_2]^+$ $[g_+t_4;\mathbf{g_+cFcF};g_-t_4]^+$ $[g_-t_6;\mathbf{g_+cFcF};g_-t_6]^+$

$[2C_2mim{:}BF_4]^+$ $[2C_4mim{:}BF_4]^+$ $[2C_6mim{:}BF_4]^+$ $[2C_8mim{:}BF_4]^+$

$[g_+;\mathbf{tcFcF};g_-]^+$ $[g_-t_2;\mathbf{g_-cFcF};g_-t_2]^+$ $[g_+g_{-4};\mathbf{tcF_mcF};g_-g_+t_3]^+$ $[g_-t_6;\mathbf{g_+cFg_-F};g_-t_6]^+$

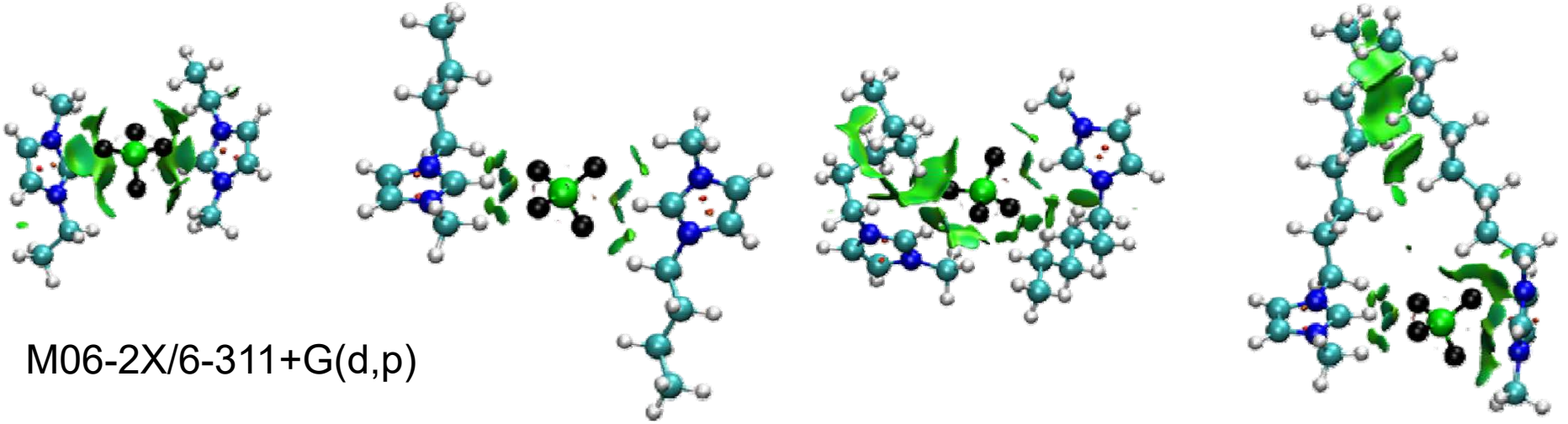

M06-2X/6-311+G(d,p)

Figure 8.

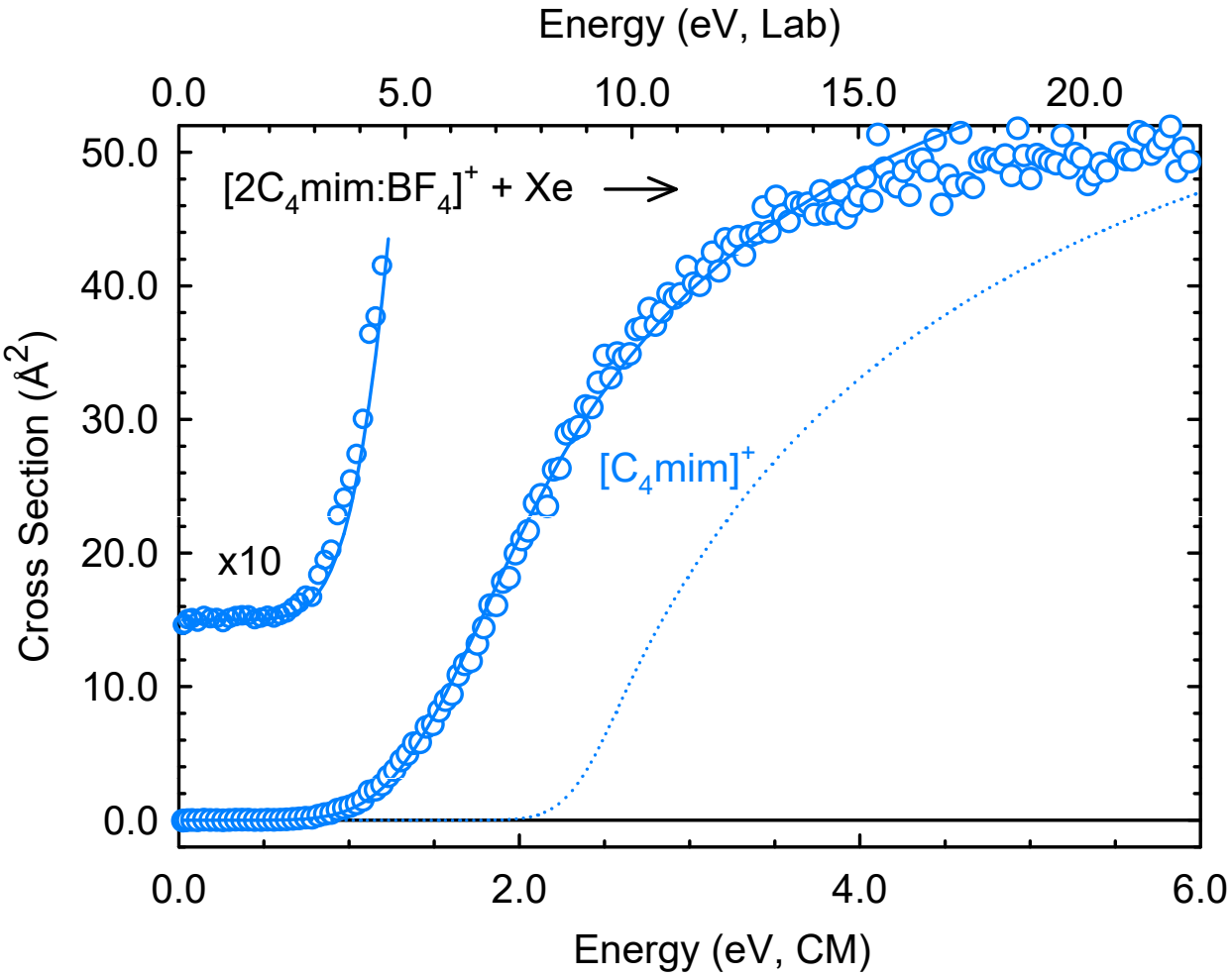
Energy (eV, Lab)
0.0
5.0
10.0
15.0
20.0
50.0
40.0
30.0
20.0
10.0
0.0
Cross Section (Å^2)
[2C$_4$mim:BF$_4$]$^+$ + Xe ⟶
[C$_4$mim]$^+$
x10
0.0
2.0
4.0
6.0
Energy (eV, CM)

Figure 9.

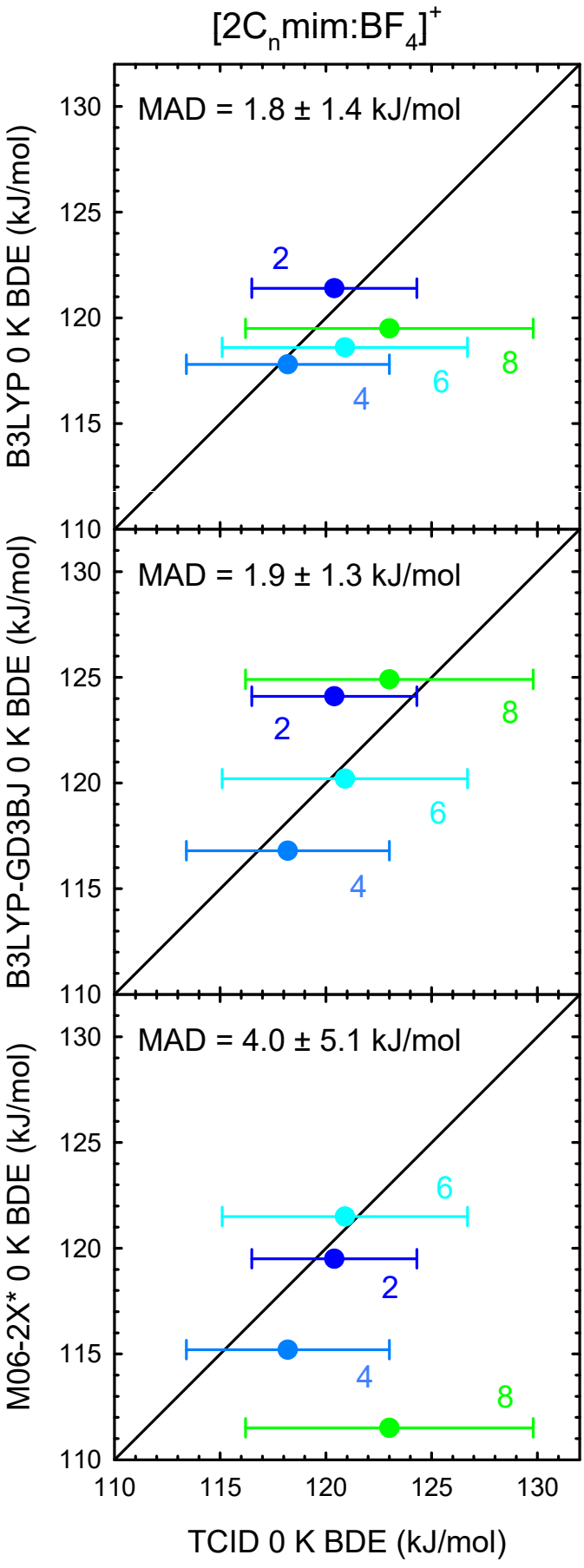
[2C$_n$mim:BF$_4$]$^+$
MAD = 1.8 ± 1.4 kJ/mol
MAD = 1.9 ± 1.3 kJ/mol
MAD = 4.0 ± 5.1 kJ/mol
B3LYP 0 K BDE (kJ/mol)
B3LYP-GD3BJ 0 K BDE (kJ/mol)
M06-2X* 0 K BDE (kJ/mol)
TCID 0 K BDE (kJ/mol)
110
115
120
125
130
2
4
6
8

TOC Graphic

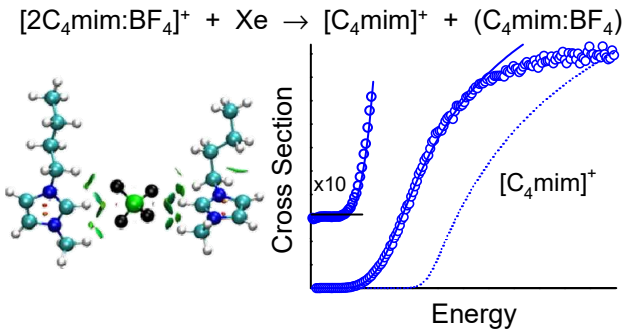
[2C4mim:BF4]+ + Xe → [C4mim]+ + (C4mim:BF4)
Cross Section
x10
[C4mim]+
Energy

Supporting Information for . . .

Gas-Phase Binding Energies and Dissociation Dynamics of 1-Alkyl-3-Methylimidazolium Tetrafluoroborate Ionic Liquid Clusters

H. A. Roy, L. A. Hamlow, and M. T. Rodgers*
Department of Chemistry, Wayne State University, Detroit, MI, 48202, USA

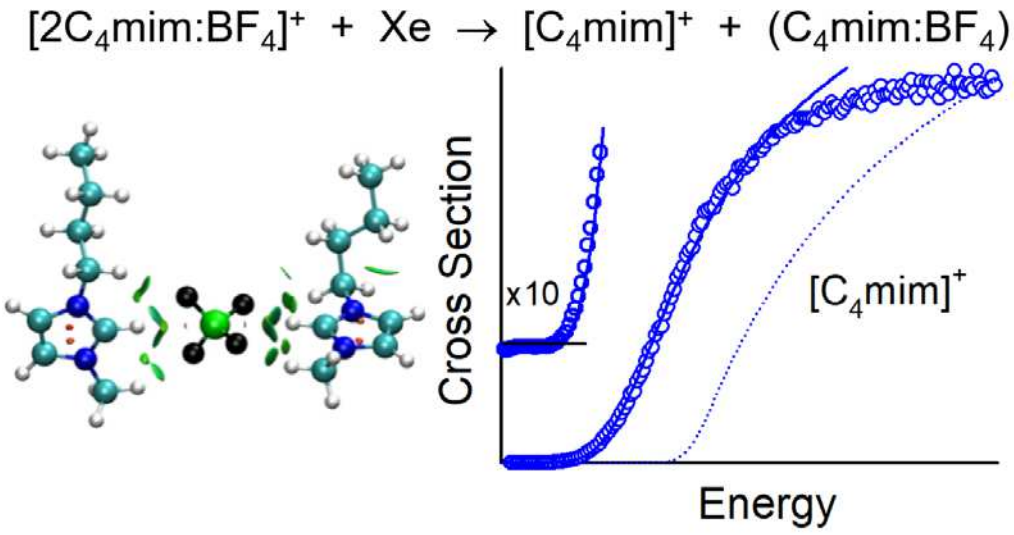

Table of Contents

Table of Contents (continued)

Structure of $[BF_4]^-$. Details of the B3LYP, B3LYP-GD3BJ, and M06-2X optimized geometries of the ground conformers of the $[BF_4]^-$ anion are summarized in **Table S4**. The B3LYP and M06-2X ground conformers of the $[BF_4]^-$ anion with NCI plots superimposed on the structures are compared in **Figure 4**. The B3LYP-GD3BJ ground conformer is not shown in the figure as it is identical to the B3LYP ground conformer. A single stable geometry is found for the $[BF_4]^-$ anion in which the fluorine atoms are coordinated to the central boron atom in an ideal tetrahedral fashion as shown in **Figure 4**. However, B3LYP and B3LYP-GD3BJ find a slightly longer B–F distance than M06-2X, 1.417 Å vs. 1.410 Å. As can be seen in the ESP map of $[BF_4]^-$ in **Figure 5**, the Mülliken charge on each fluorine atom is quite large, thus providing favorable sites for donation of electron density to the $[C_nmim]^+$ cations in the ($C_nmim{:}BF_4$) ion pairs and $[2C_nmim{:}BF_4]^+$ clusters. In contrast to that found for the H atoms of the $[C_nmim]^+$ cations, the electrostatic potential on the F atoms of $[BF_4]^-$ computed using M06-2X is slightly lower than found for B3LYP.

Table S1. CID Fragments of the $[2C_nmim{:}BF_4]^+$ Cluster Ions

precursor ion	m/z (Da/*e*)	symbol	1° fragment ion	2° fragment ions	neutral loss(es)
$[2C_2mim{:}BF_4]^+$	309				
	111	●	$[C_2mim]^+$		($C_2mim{:}BF_4$)
	83	□		$[C_4H_7N_2]^+$	C_2H_4
	29	◇		$[C_2H_5]^+$	$C_4H_6N_2$
$[2C_4mim{:}BF_4)]^+$	365				
	139	●	$[C_4mim]^+$		($C_4mim{:}BF_4$)
	83	□		$[C_4H_7N_2]^+$	C_4H_8
	57	△		$[C_4H_9]^+$	$C_4H_6N_2$
	43	○		$[C_3H_7]^+$	$C_5H_8N_2$
	29	◇		$[C_2H_5]^+$	$C_6H_{10}N_2$
$[2C_6mim{:}BF_4]^+$	421				
	167	●	$[C_6mim]^+$		($C_6mim{:}BF_4$)
	83	□		$[C_4H_7N_2]^+$	C_6H_{12}
	57	△		$[C_4H_9]^+$	$C_6H_{10}N_2$
	43	○		$[C_3H_7]^+$	$C_7H_{12}N_2$
$[2C_8mim{:}BF_4]^+$	477				
	195	●	$[C_8mim]^+$		($C_8mim{:}BF_4$)
	83	□		$[C_4H_7N_2]^+$	C_8H_{16}
	71	▽		$[C_5H_{11}]^+$	$C_7H_{12}N_2$
	57	△		$[C_4H_9]^+$	$C_8H_{14}N_2$
	43	○		$[C_3H_7]^+$	$C_9H_{16}N_2$

[a] The elemental compositions of the $[C_nmim]^+$ cations are: $[C_2mim]^+ = [C_6H_{11}N_2]^+$, $[C_4mim]^+ = [C_8H_{15}N_2]^+$, $[C_6mim]^+ = [C_{10}H_{19}N_2]^+$, and $[C_8mim]^+ = [C_{12}H_{23}N_2]^+$.

Table S2. Number of Initial Structures Subjected to Geometry Optimization and the Resultant "Unique" Stable Conformers of the $[C_nmim]^+$ Cations, ($C_nmim:BF_4$) Ion Pairs, and $[2C_nmim:BF_4]^+$ Clusters Found at the B3LYP, B3LYP-GD3BJ, and M06-2X Levels of Theory.[a]

Cation	B3LYP		B3LYP-GD3BJ		M06-2X	
	initial	"unique"	initial	"unique"	initial	"unique"
$[C_2mim]^+$	54	3	3	3	3	3
$[C_4mim]^+$	144	22	80	19	81	18
$[C_6mim]^+$	123	75	100	74	100	68
$[C_8mim]^+$	125	96	114	106	114	98
Ion Pair	B3LYP		B3LYP-GD3BJ		M06-2X	
	initial	"unique"	initial	"unique"	initial	"unique"
($C_2mim:BF_4$)	94	9	13	9	9	8
($C_4mim:BF_4$)	111	63	66	62	66	63
($C_6mim:BF_4$)	124	100	91	88	91	82
($C_8mim:BF_4$)	196	149	136	135	128	101
2:1 Cluster	B3LYP		B3LYP-GD3BJ		M06-2X	
	initial	"unique"	initial	"unique"	initial	"unique"
$[2C_2mim:BF_4]^+$	102	23	50	46	50	35
$[2C_4mim:BF_4]^+$	105	93	103	103	104	78
$[2C_6mim:BF_4]^+$	169	166	167	125	54	49
$[2C_8mim:BF_4]^+$	191	105	172	130	86	54

[a]All geometry optimizations were performed using a 6-311+G(d,p) basis set.

Table S3. Geometric Parameters of the B3LYP, B3LYP-GD3BJ, and M06-2X Ground Conformers of the $[C_nmim]^+$ Cations[a]

cation	theory	a1	a2	a3	a4	a5	a6	a7
$[C_2mim]^+$	B3LYP	-104.6						
	B3LYP-GD3BJ	-104.6						
	M06-2X	-108.0						
$[C_4mim]^+$	B3LYP	-100.1	-179.7	-179.6				
	B3LYP-GD3BJ	-103.5	61.9	177.3				
	M06-2X	-106.2	59.1	175.5				
$[C_6mim]^+$	B3LYP	-102.1	180.0	180.0	180.0	180.0		
	B3LYP-GD3BJ	-104.5	60.9	176.4	179.5	179.7		
	M06-2X	-106.4	58.9	174.0	179.2	179.4		
$[C_8mim]^+$	B3LYP	-103.0	179.3	179.8	179.5	180.0	179.7	180.0
	B3LYP-GD3BJ	-103.4	60.5	176.1	179.5	179.6	180.0	179.9
	M06-2X	-104.9	59.2	174.7	180.0	179.8	179.6	180.0

[a]The torsion angles are given in (°) and describe the following dihedral angles: a1 = ∠C2N1C1′C2′, a2 = ∠N1C1′C2′C3′, a3 = ∠C1′C2′C3′C4′, a4 = ∠C2′C3′C4′C5′, a5 = C3′C4′C5′C6′, a6 = C4′C5′C6′C7′, and a7 = ∠C5′C6′C7′C8′ as shown in **Figure S2**. The optimized structures were determined using the density functional indicated with a 6-311+G(d,p) basis set and are shown in **Figure 4** and **Figures S3-S6**.

Table S4. Geometric Parameters of B3LYP, B3LYP-GD3BJ, and M06-2X Optimized Geometries of the $[BF_4]^-$ Anion[a]

theory	B-F (Å)	∠FBF (°)
B3LYP	1.417	109.5
B3LYP-GD3BJ	1.417	109.5
M06-2X	1.410	109.5

[a]The optimized structures were determined using the density functional indicated with a 6-311+G(d,p) basis set.

Table S5. Geometric Parameters of the B3LYP, B3LYP-GD3BJ, and M06-2X Ground Conformers of the ($C_n$mim:BF_4) Ion Pairs[a]

ion pair	theory	∠C2N3C1″H	a1[b]	∠C2HB	**b**[c]	**b1**[d]
(C_2mim:BF_4)	B3LYP	-22.9	-102.5	117.6	2.4	51.1
	GD3BJ	-0.7	-38.3	106.3	-6.0	53.0
	M06-2X	-27.6	-115.1	93.4	-2.1	-61.7
(C_4mim:BF_4)	B3LYP	-26.0	-60.4	124.7	1.9	45.7
	GD3BJ	20.4	-103.5	111.6	-0.3	-53.9
	M06-2X	26.6	-35.6	91.8	-4.7	60.8
(C_6mim:BF_4)	B3LYP	-5.8	-87.1	118.4	-4.0	44.7
	GD3BJ	19.0	-103.2	112.2	-0.7	-52.9
	M06-2X	-25.1	-112.3	94.4	-2.0	-61.9
(C_8mim:BF_4)	B3LYP	-19.2	78.5	124.6	-5.7	42.9
	GD3BJ	-24.3	108.8	122.6	-1.8	46.4
	M06-2X	-22.3	-110.7	94.2	-1.6	-62.3

ion pair	theory	C1′H–F	C2H–F	C1″H–F	C2-F	C2-B
(C_2mim:BF_4)	B3LYP	2.294	2.072, 2.288	2.228	2.835	3.114
	GD3BJ	2.489	2.424, 2.051	2.365	2.851	3.052
	M06-2X	2.408	2.317, 2.294	2.617	2.709	2.937
(C_4mim:BF_4)	B3LYP	2.323	1.906, 2.428	2.241	2.950	3.166
	GD3BJ	2.442	2.222, 2.199	2.206	2.768	3.067
	M06-2X	2.365	2.392, 2.255	2.576	2.723	2.933
(C_6mim:BF_4)	B3LYP	2.261	2.296, 2.056	2.321	2.843	3.118
	GD3BJ	2.455	2.217, 2.199	2.204	2.758	3.066
	M06-2X	2.409	2.314, 2.284	2.589	2.717	2.943
(C_8mim:BF_4)	B3LYP	3.271	2.017, 2.435	2.094	2.882	3.211
	GD3BJ	2.906	1.889, 2.553	2.162	2.863	3.165
	M06-2X	2.371	2.299, 2.318	2.566	2.758	2.956

[a]Bond and dihedral angles are given in (°); bond distances are given in Angstroms. The optimized structures were determined using the density functional indicated with a 6-311+G(d,p) basis set and are shown in **Figure 6** and **Figures S7-S10**. See **Figure S2** for dihedral definitions. [b]First 1-alkyl dihedral angle a1 ≡ ∠C2N1C1′C2′. [c]Binding site dihedral angle defined as **b** ≡ ∠(C2,©,©+CP,B), where © denotes the centroid of the imidazolium ring. [d]Binding orientation dihedral angle defined as **b1** ≡ ∠C1″N3C2B.

Table S6. Geometric Parameters of the B3LYP, B3LYP-GD3BJ, and M06-2X Ground Conformers of the $[2C_nmim:BF_4]^+$ Clusters[a]

system	Theory	∠C2N3C1″H	a1[b]	∠C2HB	**b**[c]	**b1**[d]	**b2**[e]
$[2C_2mim:BF_4]^+$	B3LYP	-0.5	-107.9	178.4	-0.7	-0.6	93.1
		-0.4	-106.9	177.7	-0.1	1.1	
	B3LYP-GD3BJ	-3.9	101.5	172.3	0.5	7.7	92.8
		1.4	-103.0	178.0	0.5	-2.3	
	M06-2X	25.7	110.9	99.6	-4.0	56.4	147.8
		29.5	-117.5	87.9	-5.4	66.2	
$[2C_4mim:BF_4]^+$	B3LYP	1.2	85.0	172.9	-2.2	-4.8	-87.8
		0.6	104.7	174.9	1.5	-3.6	
	B3LYP-GD3BJ	10.3	-89.5	154.9	1.6	-24.4	-93.1
		-8.3	89.7	161.4	3.7	18.6	
	M06-2X	-3.7	-104.8	166.6	-0.4	11.7	-104.7
		-3.7	-104.7	166.6	-1.7	11.7	
$[2C_6mim:BF_4]^+$	B3LYP	-1.2	103.9	177.1	-1.3	1.6	88.8
		0.3	-105.4	176.7	0.4	1.0	
	B3LYP-GD3BJ	0.6	-104.0	169.9	4.9	-0.4	101.2
		22.0	-96.3	125.3	-2.1	-49.6	
	M06-2X	14.3	102.1	114.6	-25.0	34.5	155.7
		11.0	-104.3	145.8	-4.5	-30.3	
$[2C_8mim:BF_4]^-$	B3LYP	-2.2	-105.6	173.5	-2.3	3.9	95.5
		-2.3	-105.5	173.5	1.5	4.0	
	B3LYP-GD3BJ	-4.6	96.0	172.1	2.9	5.9	-69.2
		-4.7	96.0	172.2	-2.3	5.8	
	M06-2X	-2.7	-98.3	166.5	0.7	11.3	80.1
		22.6	-109.9	107.4	0.4	-62.5	

system	Theory	C1′H–F	C2H–F	C1″H–F	C2-B
$[2C_2mim:BF_4]^+$	B3LYP	2.460	2.082, 2.110	2.375	3.664
		2.471	2.071, 2.121	2.367	3.663
	B3LYP-GD3BJ	2.424	2.076, 2.048	2.395	3.613
		2.404	2.055, 2.068	2.389	3.618
	M06-2X	2.684	2.428, 2.366	2.688	3.039
		2.583	2.583, 2.509	2.908	3.028
$[2C_4mim:BF_4]^+$	B3LYP	2.726	2.049, 2.158	2.306	3.666
		2.514	2.066, 2.134	2.340	3.665
	B3LYP-GD3BJ	2.554	2.138, 2.045	2.432	3.578
		2.528	2.096, 2.066	2.459	3.599
	M06-2X	2.368	2.044, 2.053	2.318	3.586
		2.368	2.044, 2.053	2.318	3.585
$[2C_6mim:BF_4]^+$	B3LYP	2.526	2.074, 2.127	2.348	3.668
		2.513	2.066, 2.136	2.342	3.668
	B3LYP-GD3BJ	2.243	2.258, 1.941	2.647	3.644
		2.571	2.099, 2.279	2.405	3.373
	M06-2X	4.161	2.056, -	2.425	3.421
		2.460	2.088, 2.125	2.306	3.531
$[2C_8mim:BF_4]^-$	B3LYP	2.574	2.050, 2.157	2.301	3.667
		2.573	2.050, 2.157	2.301	3.667
	B3LYP-GD3BJ	2.319	2.123, 1.999	2.527	3.608
		2.319	2.122, 1.999	2.527	3.608
	M06-2X	2.317	2.111, 1.985	2.390	3.579
		2.384	2.199, 2.334	2.345	3.245

[a]Bond and dihedral angles are given in (°). The optimized structures were determined using the density functional indicated with a 6-311+G(d,p) basis set and are shown in **Figure 7** and **Figures S11-14**. See **Figure S2** for dihedral definitions. [b]First 1-alkyl dihedral angle a1 ≡ ∠C2N1C1′C2′. [c]Binding site dihedral angle defined as **b** ≡ ∠(C2,©,©+CP,B), where © denotes the centroid of the imidazolium ring. [d]Binding orientation dihedral angle defined as **b1** ≡ ∠C1″N3C2B. [e]Relative cation binding orientation dihedral angle defined as **b2** ≡ ∠C1′N1N1C1′.

Table S7. Vibrational Frequencies and Average Vibrational Energies of the ground conformers of the $[2C_nmim:BF_4]^+$, Clusters, the $[C_nmim]^+$ Cations and ($C_nmim:BF_4$) Ion Pairs[a]

system	E_{int}, eV [b]	Frequencies (cm^{-1}) [c]
$[2C_2mim:BF_4]^+$	0.66 (0.04)	9, 10, 14, 27, 29, 32, 43, 45, 54, 56, 74, 79, 81, 116, 118, 127, 137, 139, 208, 213, 232, 233, 297, 298, 329, 361, 377(2), 429(2), 496(2), 517, 595, 596, 634, 635, 663(2), 699(2), 744, 749(2), 808, 809, 868(2), 909, 911, 963, 964, 1014(2), 1031, 1038, 1048, 1049, 1056, 1102(2), 1108, 1109, 1121, 1122, 1141, 1142, 1157(2), 1177(2), 1274(2), 1313(2), 1345(2), 1388(2), 1413, 1414, 1425, 1426, 1448(2), 1464, 1465, 1493, 1494, 1495, 1496, 1497, 1498, 1511, 1512, 1513(2), 1592, 1593, 1604(2), 3043(2), 3063(2), 3074(2), 3108(2), 3119(2), 3138(2), 3140(2), 3165(2), 3247, 3251, 3274, 3275, 3292, 3293
$[2C_4mim:BF_4]^+$	0.81 (0.05)	5, 7, 13, 15, 20, 24, 29, 41, 44, 49, 70, 76(2), 78, 80, 81, 85, 110, 111, 121, 131, 148, 199, 207, 237, 240, 246, 249, 282, 290, 318, 327, 329, 361, 406, 415, 440, 493, 496, 497, 517, 595, 628, 635, 636, 664, 667, 699, 736, 744, 745, 749, 750, 758, 807, 827, 867, 868, 885, 909, 914, 919, 951, 960, 994, 1012, 1014, 1015, 1030, 1037, 1044, 1048, 1054, 1058, 1062, 1108(2), 1120, 1122, 1128, 1130, 1149, 1155, 1157(2), 1174, 1177, 1235, 1240, 1276, 1295, 1302, 1304, 1322, 1328, 1336, 1338, 1348, 1354, 1387, 1389, 1400, 1401, 1411, 1417, 1420, 1423, 1446, 1447, 1463, 1464, 1483, 1492, 1494, 1495(2), 1498, 1499, 1501, 1502, 1505, 1511, 1512(2), 1516, 1590, 1593, 1603, 1604, 3005, 3014, 3022, 3027, 3028, 3031, 3034, 3040, 3062(2), 3063, 3064, 3071, 3079, 3090, 3091, 3100(2), 3127, 3130, 3139(2), 3165, 3167, 3244, 3250, 3275, 3277, 3293, 3295
$[2C_6mim:BF_4]^+$	0.97 (0.07)	7, 9, 14, 16, 18, 26, 32, 33, 41, 43, 46, 48, 61, 62, 68, 75, 80(2), 82, 124, 125(2), 127, 130, 138, 139, 144, 147, 215(2), 240, 241, 244, 247, 286, 287, 296(2), 329, 361, 408, 409, 439, 440, 454(2), 496(2), 517, 629(2), 635, 636, 669, 670, 735, 736, 740(2), 744, 748, 749, 752(2), 803, 804, 866, 867, 899(2), 900(2), 910, 914, 1003, 1004, 1008, 1010, 1014, 1015, 1031, 1038(3), 1047(2), 1053, 1055, 1057, 1067, 1070, 1109(2), 1121, 1122, 1136(2), 1156, 1157, 1159, 1160, 1176, 1177, 1221, 1222, 1262, 1265, 1274(2), 1301, 1302, 1323(2), 1328, 1329, 1337, 1339, 1341(2), 1348, 1349, 1382(2), 1398(2), 1403, 1405, 1417(3), 1418, 1445, 1446, 1465(2), 1487(2), 1489(2), 1493(2), 1499(2), 1500, 1501(3), 1509(2), 1513, 1514, 1516(2), 1592, 1593, 1603, 1604, 2999(2), 3005(2), 3012(2), 3018, 3019, 3022(2), 3023(2), 3034(2), 3049, 3050, 3062, 3063, 3064(2), 3071(2), 3083, 3084, 3092, 3093, 3127, 3128, 3139(2), 3165(2), 3247, 3252, 3275(2), 3293(2)
$[2C_8mim:BF_4]^+$	1.11 (0.08)	5, 8, 9, 13, 19, 24, 27, 30, 34, 36, 38(2), 49, 50, 58(2), 74, 78, 79, 88(2), 95, 97, 109, 112, 131(3), 144(2), 157(2), 177(2), 194(2), 243(2), 247(2), 285(2), 313(2), 329, 361, 374(2), 418(2), 449(2), 493, 494, 496(2), 516, 628(2), 636(2), 669, 670, 733(2), 737(2), 740(2), 744, 749(2), 759(2), 804(2), 867(2), 874(2), 899(2), 911, 913, 957(2), 994(2), 1006(2), 1014, 1016, 1030, 1033, 1034, 1038, 1041(2), 1049, 1050, 1056, 1062(2), 1065(2), 1073(2), 1108, 1109, 1121, 1122, 1139(2), 1157(2), 1159(2), 1177, 1178, 1213(2), 1245(2), 1254(2), 1289(2), 1294(2), 1308(2), 1327(2), 1330(2), 1338(2), 1342(2), 1344(2), 1349(2), 1380(2), 1396(2), 1403(2), 1404(2), 1416(2), 1417(2), 1446(2), 1464, 1465, 1486(2), 1487(2), 1491(2), 1492(2), 1498(2), 1499(2), 1501(2), 1506(2), 1512(2), 1513(2), 1517(2), 1592(2), 1604(2), 2994(2), 2997(2), 3002(2), 3007(2), 3012(3), 3019(2), 3021(2), 3022(2), 3031(2), 3042(2), 3053(2), 3062(2), 3064(2), 3071(2), 3081(2), 3089(2), 3126(2), 3139(2), 3167(2), 3245, 3249, 3275(2), 3293(2)
($C_2mim:BF_4$)	0.36 (0.03)	8, 35, 43, 66, 75, 86, 109, 124, 179, 213, 237, 302, 342, 346, 383, 430, 497, 500, 507, 597, 636, 671, 705, 735, 736, 805, 854, 930, 951, 965, 996, 1040, 1050, 1103, 1111, 1120, 1140, 1157, 1161, 1181, 1271, 1313, 1353, 1392, 1412, 1424, 1456, 1464, 1494, 1497, 1505, 1509, 1516, 1596, 1603, 3036, 3056, 3077, 3099, 3112, 3135, 3137, 3158, 3257, 3276, 3295

Table S7. (continued) Vibrational Frequencies and Average Vibrational Energies of the ground conformers of the $[2C_nmim:BF_4]^+$, Clusters, the $[C_nmim]^+$ Cations and ($C_nmim:BF_4$) Ion Pairs[a]

system	E_{int}, eV [b]	Frequencies (cm^{-1}) [c]
($C_4mim:BF_4$)	0.44 (0.03)	7, 21, 47, 50, 60, 74, 84, 95, 109, 143, 177, 211, 248, 254, 298, 319, 344, 345, 413, 496, 500, 508(2), 597, 635, 664, 706, 735, 736, 759, 830, 851, 888, 946, 961, 972, 990, 1000, 1038, 1042, 1063, 1108, 1120, 1130, 1148, 1156, 1162, 1184, 1245, 1285, 1309, 1328, 1338, 1360, 1388, 1402, 1408, 1419, 1450, 1461, 1489, 1495, 1497, 1501, 1503, 1507, 1512, 1594, 1601, 3003, 3025, 3027, 3035, 3056, 3062, 3076, 3088, 3092, 3123, 3138, 3157, 3189, 3277, 3296
($C_6mim:BF_4$)	0.52 (0.04)	11, 16, 36, 39, 49, 57, 66, 83, 85, 99, 121, 123, 137, 165, 226, 243(2), 290, 297, 342, 345, 420, 437, 448, 496, 500, 508, 629, 638, 672, 734, 735(2), 748, 754, 802, 852, 896, 898, 933, 951, 996, 1004, 1005, 1040, 1041, 1045, 1053, 1066, 1110, 1120, 1137, 1152, 1158, 1160, 1181, 1220, 1262, 1272, 1302, 1320, 1327, 1334, 1337, 1355, 1383, 1402, 1403, 1415, 1418, 1452, 1464, 1487, 1489, 1494, 1495, 1500, 1502, 1510, 1511, 1517, 1594, 1605, 2996, 3002, 3010, 3014, 3019, 3021, 3033, 3045, 3058, 3061, 3069, 3080, 3087, 3123, 3139, 3161, 3255, 3276, 3295
($C_8mim:BF_4$)	0.59 (0.04)	1, 23, 28, 41, 43, 48, 55, 75, 81, 92, 106, 117, 130, 143, 158, 177, 193, 225, 245, 256, 293, 324, 343, 347, 393, 419, 470, 497, 501, 507, 511, 598, 636, 668, 704, 735, 737, 739, 745, 778, 836, 856, 875, 899, 923, 930, 969, 978, 989, 1007, 1027, 1040, 1042, 1049, 1057, 1066, 1082, 1110, 1121, 1137, 1154, 1159, 1162, 1179, 1216, 1233, 1258, 1278, 1303, 1311, 1319, 1331, 1339, 1346, 1352, 1364, 1387, 1396, 1402, 1403, 1414, 1415, 1451, 1464, 1485, 1486, 1489, 1492, 1495, 1499, 1500, 1506, 1507, 1508, 1514, 1591, 1604, 2981, 2991, 2996, 3003, 3006, 3015, 3019, 3023, 3024, 3038, 3045, 3053, 3061, 3063, 3080, 3083, 3103, 3119, 3136, 3155, 3227, 3278, 3296
$[C_2mim]^+$	0.19 (0.02)	46, 69, 135, 209, 233, 292, 378, 425, 592, 633, 660, 698, 753, 803, 834, 881, 962, 1036, 1043, 1099, 1102, 1125, 1136, 1150, 1175, 1270, 1311, 1343, 1385, 1411, 1428, 1437, 1461, 1484, 1491, 1494, 1509, 1510, 1595, 1604, 3046, 3070, 3079, 3110, 3122, 3134, 3150, 3165, 3274, 3278, 3292
$[C_4mim]^+$	0.27 (0.02)	28, 65, 69, 83, 112, 199, 237, 247, 273, 318, 407, 434, 626, 632, 664, 733, 741, 752, 801, 834, 879, 916, 946, 1010, 1037, 1042, 1054, 1100, 1125, 1128, 1147, 1150, 1175, 1234, 1295, 1299, 1318, 1336, 1345, 1381, 1395, 1412, 1424, 1436, 1460, 1484, 1489, 1492, 1502(2), 1510, 1515, 1594, 1603, 3015, 3025, 3032, 3041, 3065, 3069, 3072, 3094, 3108, 3121, 3149, 3165, 3274, 3279, 3292
$[C_6mim]^+$	0.34 (0.03)	28, 49, 52, 63, 76, 124, 131, 147, 214, 238, 245, 278, 294, 408, 437, 449, 626, 631, 666, 736, 737, 750, 754, 802, 833, 881, 897, 901, 1001, 1007, 1035, 1037, 1041, 1046, 1062, 1099, 1125, 1135, 1149, 1154, 1174, 1219, 1262, 1272, 1303, 1320, 1326, 1336, 1340, 1344, 1378, 1394, 1401, 1412, 1420, 1436, 1460, 1484, 1488, 1489, 1493, 1500, 1502, 1510(2), 1517, 1595, 1603, 3001, 3006, 3015, 3022, 3024, 3026, 3035, 3051, 3067, 3068, 3072, 3086, 3098, 3122, 3148, 3164, 3274, 3277, 3291
$[C_8mim]^+$	0.42 (0.03)	20, 38, 40, 53, 70, 93, 96, 107, 149, 156, 175, 193, 242(2), 279, 311, 374, 416, 448, 492, 626, 631, 666, 734, 736, 738, 752, 757, 801, 833, 872, 880, 900, 955, 994, 1004, 1032, 1036, 1038, 1044, 1059, 1064, 1072, 1100, 1125, 1138, 1148, 1155, 1172, 1211, 1245, 1251, 1286, 1294, 1306, 1322, 1329, 1338, 1340, 1342, 1345, 1378, 1392, 1402, 1403, 1412, 1419, 1435, 1461, 1484, 1486, 1487, 1491, 1492, 1497, 1501, 1505, 1511, 1512, 1517, 1594, 1603, 2996, 2999, 3004, 3009, 3014(2), 3022(2), 3025, 3032, 3044, 3055, 3068(2), 3071, 3083, 3091, 3120, 3148, 3164, 3275, 3277, 3292

[a] Determined at the B3LYP/6-311+G(d,p) level of theory and with frequencies scaled by 0.9887. [b] Uncertainties are listed in parentheses. [c] Degeneracies are listed in parentheses.

Table S8. Rotational Constants of $[2C_nmim:BF_4]^+$ Clusters and the Corresponding PSL TS

system	energized molecule		transition state		
	1-D[a]	2-D[b]	1-D[c]	2-D[c]	2-D[d]
$[2C_2mim:BF_4]^+$	0.018578	0.003256	0.178019, 0.032403	0.039347, 0.016170	0.0015
$[2C_4mim:BF_4]^+$	0.008542	0.002427	0.132015, 0.020795	0.016727, 0.011502	0.0010
$[2C_6mim:BF_4]^+$	0.003976	0.001782	0.110309, 0.019774	0.008309, 0.005575	0.0007
$[2C_8mim:BF_4]^+$	0.001084	0.001887	0.096471, 0.014283	0.004695, 0.004880	0.0004

[a] Active external. [b] Inactive external. [c] Rotational constants of the transition state treated as free internal rotors. [d] Two-dimensional rotational constants of the transition state at threshold, treated variationally and statistically.

Table S9. Fitting Parameters of eq 3, Threshold Dissociation Energies at 0 K, and Entropies of Activation at 1000 K of $[2C_nmim:BF_4]^+$ Clusters[a]

system	σ^b	n	$E_0{}^c$ (eV)	E_0(PSL)[b] (eV)	kinetic shift (eV)	$\Delta S^{\ddagger}$ (PSL)[b] (J mol^{-1} K^{-1})
$[2C_2mim:BF_4]^+$	105.7 (4.4)	0.93 (0.02)	1.95 (0.04)	1.21 (0.04)	0.74	12 (4)
$[2C_4mim:BF_4]^+$	84.9 (1.9)	0.91 (0.02)	2.25 (0.06)	1.14 (0.06)	1.11	-2(4)
$[2C_6mim:BF_4]^+$	108.6 (1.8)	1.06 (0.01)	2.54 (0.08)	1.20 (0.08)	1.24	55 (4)
$[2C_8mim:BF_4]^+$	98.9 (4.5)	1.29 (0.03)	2.81 (0.09)	1.30 (0.07)	1.51	58 (4)

[a] Average values obtained for fits to the $[C_nmim]^+$ product cross section based on parameters derived from the B3LYP-GD3BJ/6-311+G(d,p) optimized structures. Uncertainties are listed in parentheses. [b]Average values for a loose PSL TS. [c]No RRKM analysis.

Table S10. Fitting Parameters of eq 3, Threshold Dissociation Energies at 0 K, and Entropies of Activation at 1000 K of $[2C_nmim:BF_4]^+$ Clusters[a]

system	σ^b	n	$E_0{}^c$ (eV)	E_0(PSL)[b] (eV)	kinetic shift (eV)	$\Delta S^{\ddagger}$ (PSL)[b] (J mol^{-1} K^{-1})
$[2C_2mim:BF_4]^+$	103.8 (4.4)	0.94 (0.02)	1.92 (0.06)	1.27 (0.04)	0.65	39 (4)
$[2C_4mim:BF_4]^+$	82.8 (1.8)	0.94 (0.02)	2.21 (0.05)	1.20 (0.05)	1.00	17 (4)
$[2C_6mim:BF_4]^+$	93.4 (3.1)	1.22 (0.03)	2.41 (0.08)	1.33 (0.05)	1.07	71 (4)
$[2C_8mim:BF_4]^+$	97.5 (3.1)	1.28 (0.02)	2.78 (0.10)	1.28 (0.07)	1.50	47 (4)

[a] Average values obtained for fits to the $[C_nmim]^+$ product cross section based on parameters derived from the M06-2X/6-311+G(d,p) optimized structures. Uncertainties are listed in parentheses. [b]Average values for a loose PSL TS. [c]No RRKM analysis.

Figure Captions

Figure S1. Cross sections for collision-induced dissociation of the $[2C_nmim{:}BF_4]^+$ IL clusters with Xe as a function of collision energy in the center-of-mass frame (lower *x*-axis) and laboratory frame (upper *x*-axis); data for n = 2, 4, 6 and 8 are shown in parts a-d, respectively. The data shown was acquired at a Xe pressure of ~ 0.2 mTorr. Refer to **Table S1** for CID product legend.

Figure S2. Nomenclature employed in this work to describe the stable conformations predicted for the $[C_nmim]^+$ cations, $(C_nmim{:}BF_4)$ ion pairs, and $[2C_nmim{:}BF_4]^+$ clusters.

Figure S3. Relative Gibbs energy distributions for the stable B3LYP, B3LYP-GD3BJ and M06-2X conformers of the $[C_2mim]^+$ cation computed at 298 K (in kJ/mol).

Figure S4. Relative Gibbs energy distributions for the stable B3LYP, B3LYP-GD3BJ and M06-2X conformers of the $[C_4mim]^+$ cation computed at 298 K (in kJ/mol).

Figure S5. Relative Gibbs energy distributions for the stable B3LYP, B3LYP-GD3BJ and M06-2X conformers of the $[C_6mim]^+$ cation computed at 298 K (in kJ/mol).

Figure S6. Relative Gibbs energy distributions for the stable B3LYP, B3LYP-GD3BJ and M06-2X conformers of the $[C_8mim]^+$ cation computed at 298 K (in kJ/mol).

Figure S7. Relative Gibbs energy distributions for the stable B3LYP, B3LYP-GD3BJ and M06-2X conformers of the $(C_2mim{:}BF_4)$ ion pair computed at 298 K (in kJ/mol).

Figure S8. Relative Gibbs energy distributions for the stable B3LYP, B3LYP-GD3BJ and M06-2X conformers of the $(C_4mim{:}BF_4)$ ion pair computed at 298 K (in kJ/mol).

Figure S9. Relative Gibbs energy distributions for the stable B3LYP, B3LYP-GD3BJ and M06-2X conformers of the $(C_6mim{:}BF_4)$ ion pair computed at 298 K (in kJ/mol).

Figure S10. Relative Gibbs energy distributions for the stable B3LYP, B3LYP-GD3BJ and M06-2X conformers of the $(C_8mim{:}BF_4)$ ion pair computed at 298 K (in kJ/mol).

Figure S11. Relative Gibbs energy distributions for the stable B3LYP, B3LYP-GD3BJ and M06-2X conformers of the $[2C_2mim{:}BF_4]^+$ cluster computed at 298 K (in kJ/mol).

Figure S12. Relative Gibbs energy distributions for the stable B3LYP, B3LYP-GD3BJ and M06-2X conformers of the $[2C_4mim{:}BF_4]^+$ cluster computed at 298 K (in kJ/mol).

Figure S13. Relative Gibbs energy distributions for the stable B3LYP, B3LYP-GD3BJ and M06-2X conformers of the $[2C_6mim{:}BF_4]^+$ cluster computed at 298 K (in kJ/mol).

Figure S14. Relative Gibbs energy distributions for the stable B3LYP, B3LYP-GD3BJ and M06-2X conformers of the $[2C_8mim{:}BF_4]^+$ cluster computed at 298 K (in kJ/mol).

Figure S15. B3LYP/6-311+G(d,p) optimized geometries of the ground and stable low-energy conformers of the $[C_2mim]^+$ cation. Conformer designations along with the B3LYP/6-311+G(2d,2p), B3LYP-GD3BJ/6-31+G(2d,2p) and M06-2X/6-311+G(2d,2p) relative Gibbs energies at 298 K (in kJ/mol) are also given.

Figure S16. B3LYP/6-311+G(d,p) optimized geometries of the ground and stable low-energy conformers of the $[C_4mim]^+$ cation. Conformer designations along with the B3LYP/6-311+G(2d,2p), B3LYP-GD3BJ/6-31+G(2d,2p) and M06-2X/6-311+G(2d,2p) relative Gibbs energies at 298 K (in kJ/mol) are also given. All M06-2X values required use of an ultrafine integration grid during geometry optimization and frequency analysis for proper convergence.

Figure S17. B3LYP/6-311+G(d,p) optimized geometries of the ground and stable low-energy conformers of the $[C_6mim]^+$ cation. Conformer designations along with the B3LYP/6-311+G(2d,2p), B3LYP-GD3BJ/6-31+G(2d,2p) and M06-2X/6-311+G(2d,2p) relative Gibbs energies at 298 K (in kJ/mol) are also given. Values indicated with an asterisk required use of an ultrafine integration grid during optimization and frequency analysis for proper convergence.

Figure S18. B3LYP/6-311+G(d,p) optimized geometries of the ground and stable low-energy conformers of the $[C_8mim]^+$ cation. Conformer designations along with the B3LYP/6-311+G(2d,2p), B3LYP-GD3BJ/6-31+G(2d,2p) and M06-2X/6-311+G(2d,2p) relative Gibbs energies at 298 K (in kJ/mol) are also given.

Figure S19. Noncovalent interaction maps superimposed on the B3LYP/6-311+G(d,p) optimized geometries of the ground and stable low-energy conformers of the ($C_2mim:BF_4$) ion pair. Conformer designations along with the B3LYP/6-311+G(2d,2p), B3LYP-GD3BJ/6-31+G(2d,2p) and M06-2X/6-311+G(2d,2p) relative Gibbs energies at 298 K (in kJ/mol) are also given. Conformers not determined upon M06-2X re-optimization of the B3LYP optimized structures (due to significant structural rearrangement) are indicated with a dash.

Figure S20. Noncovalent interaction maps superimposed on the B3LYP/6-311+G(d,p) optimized geometries of the ground and stable low-energy conformers of the ($C_4mim:BF_4$) ion pair. Conformer designations along with the B3LYP/6-311+G(2d,2p), B3LYP-GD3BJ/6-31+G(2d,2p) and M06-2X/6-311+G(2d,2p) relative Gibbs energies at 298 K (in kJ/mol) are also given. Conformers not determined upon M06-2X re-optimization of the B3LYP optimized structures (due to significant structural rearrangement) are indicated with a dash.

Figure S21. Noncovalent interaction maps superimposed on the B3LYP/6-311+G(d,p) optimized geometries of the ground and stable low-energy conformers of the ($C_6mim:BF_4$) ion pair. Conformer designations along with the B3LYP/6-311+G(2d,2p), B3LYP-GD3BJ/6-31+G(2d,2p) and M06-2X/6-311+G(2d,2p) relative Gibbs energies at 298 K (in kJ/mol) are also given. Conformers not determined upon B3LYP-GD3BJ or M06-2X re-optimization of the B3LYP optimized structures (due to significant structural rearrangement) are indicated with a dash. Values indicated with an asterisk required use of an ultrafine integration grid during optimization and frequency analysis for proper convergence.

Figure S22. Noncovalent interaction maps superimposed on the B3LYP/6-311+G(d,p) optimized geometries of the ground and stable low-energy conformers of the ($C_8mim:BF_4$) ion pair. Conformer designations along with the B3LYP/6-311+G(2d,2p), B3LYP-GD3BJ/6-31+G(2d,2p) and M06-2X/6-311+G(2d,2p) relative Gibbs energies at 298 K (in kJ/mol) are also given. Conformers not determined upon M06-2X re-optimization of the B3LYP optimized structures (due to significant structural rearrangement) are indicated with a dash.

Figure S23. Electrostatic potential maps of the B3LYP/6-311+G(d,p) and M06-2X/6-311+G(d,p) ground conformers of the ($C_nmim:BF_4$) ion pairs.

Figure S24. Distributions of **B**, $\mathbf{B_m}$, $\mathbf{F_m}$, **F**, $\mathbf{F_a}$, $\mathbf{B_a}$, and **B** binding sites found among the stable B3LYP, B3LYP-GD3BJ, and M06-2X conformations computed for the ($C_2mim:BF_4$) ion pair. The vertical dotted lines delineate the range of **b** values that define the binding site designations.

Figure S25. Distributions of **B**, $\mathbf{B_m}$, $\mathbf{F_m}$, **F**, $\mathbf{F_a}$, $\mathbf{B_a}$, and **B** binding sites found among the stable B3LYP, B3LYP-GD3BJ, and M06-2X conformations computed for the ($C_4mim:BF_4$) ion pair. The vertical dotted lines delineate the range of **b** values that define the binding site designations.

Figure S26. Distributions of **B**, $\mathbf{B_m}$, $\mathbf{F_m}$, **F**, $\mathbf{F_a}$, $\mathbf{B_a}$, and **B** binding sites found among the stable B3LYP, B3LYP-GD3BJ, and M06-2X conformations computed for the ($C_6mim:BF_4$) ion pair. The vertical dotted lines delineate the range of **b** values that define the binding site designations.

Figure S27. Distributions of **B**, $\mathbf{B_m}$, $\mathbf{F_m}$, **F**, $\mathbf{F_a}$, $\mathbf{B_a}$, and **B** binding sites found among the stable B3LYP, B3LYP-GD3BJ, and M06-2X conformations computed for the ($C_8mim:BF_4$) ion pair. The vertical dotted lines delineate the range of **b** values that define the binding site designations.

Figure S28. Noncovalent interaction maps superimposed on the B3LYP/6-311+G(d,p) optimized geometries of the ground and stable low-energy conformers of the $[2C_2mim:BF_4]^+$ cluster. Conformer designations along with the B3LYP/6-311+G(2d,2p), B3LYP-GD3BJ/6-31+G(2d,2p) and M06-2X/6-311+G(2d,2p) relative Gibbs energies at 298 K (in kJ/mol) are also given. Conformers not determined upon M06-2X re-optimization of the B3LYP optimized structures (due to significant structural rearrangement) are indicated with a dash.

Figure S29. Noncovalent interaction maps superimposed on the B3LYP/6-311+G(d,p) optimized geometries of the ground and stable low-energy conformers of the $[2C_4mim:BF_4]^+$ cluster. Conformer designations along with the B3LYP/6-311+G(2d,2p), B3LYP-GD3BJ/6-31+G(2d,2p) and M06-2X/6-311+G(2d,2p) relative Gibbs energies at 298 K (in kJ/mol) are also given. Conformers not determined upon M06-2X re-optimization of the B3LYP optimized structures (due to significant structural rearrangement) are indicated with a dash.

Figure S30. Noncovalent interaction maps superimposed on the B3LYP/6-311+G(d,p) optimized geometries of the ground and stable low-energy conformers of the $[2C_6mim:BF_4]^+$ cluster. Conformer designations along with the B3LYP/6-311+G(2d,2p), B3LYP-GD3BJ/6-31+G(2d,2p) and M06-2X/6-311+G(2d,2p) relative Gibbs energies at 298 K (in kJ/mol) are also given. Conformers not determined upon M06-2X re-optimization of the B3LYP optimized structures (due to significant structural rearrangement) are indicated with a dash. Values indicated with an asterisk required use of an ultrafine integration grid during optimization and frequency analysis for proper convergence.

Figure S31. Noncovalent interaction maps superimposed on the B3LYP/6-311+G(d,p) optimized geometries of the ground and stable low-energy conformers of the $[2C_8mim:BF_4)]^+$ cluster. Conformer designations along with the B3LYP/6-311+G(2d,2p), B3LYP-GD3BJ/6-31+G(2d,2p) and M06-2X/6-311+G(2d,2p) relative Gibbs energies at 298 K (in kJ/mol) are also given. Conformers not determined upon M06-2X re-optimization of the B3LYP optimized structures (due to significant structural rearrangement) are indicated with a dash.

Figure S32. Electrostatic potential maps of the B3LYP/6-311+G(d,p) and M06-2X/6-311+G(d,p) ground conformers of the $[2C_nmim:BF_4)]^+$ clusters.

Figure S33. Distributions of **B**, $\mathbf{B_m}$, $\mathbf{F_m}$, **F**, $\mathbf{F_a}$, $\mathbf{B_a}$, and **B** binding sites found among the stable B3LYP, B3LYP-GD3BJ, and M06-2X conformations computed for the $[2C_2mim:BF_4]^+$ cluster. The vertical dotted lines delineate the range of **b** values that define the binding site designations.

Figure S34. Distributions of **B**, $\mathbf{B_m}$, $\mathbf{F_m}$, **F**, $\mathbf{F_a}$, $\mathbf{B_a}$, and **B** binding sites found among the stable B3LYP, B3LYP-GD3BJ, and M06-2X conformations computed for the $[2C_4mim:BF_4]^+$ cluster. The vertical dotted lines delineate the range of **b** values that define the binding site designations.

Figure S35. Distributions of **B**, $\mathbf{B_m}$, $\mathbf{F_m}$, **F**, $\mathbf{F_a}$, $\mathbf{B_a}$, and **B** binding sites found among the stable B3LYP, B3LYP-GD3BJ, and M06-2X conformations computed for the $[2C_6mim:BF_4]^+$ cluster. The vertical dotted lines delineate the range of **b** values that define the binding site designations.

Figure S36. Distributions of **B**, $\mathbf{B_m}$, $\mathbf{F_m}$, **F**, $\mathbf{F_a}$, $\mathbf{B_a}$, and **B** binding sites found among the stable B3LYP, B3LYP-GD3BJ, and M06-2X conformations computed for the $[2C_8mim:BF_4]^+$ cluster. The vertical dotted lines delineate the range of **b** values that define the binding site designations.

Figure S37. B3LYP/6-311+G(d,p) isotropic molecular polarizabilities of the $[C_nmim]^+$ cations, $(C_nmim:BF_4)$ ion pairs and $[2C_nmim:BF_4]^+$ clusters (solid lines), and PBE1PBE/6-311+G(2d,p) isotropic molecular polarizabilities of the $(C_nmim:BF_4)$ ion pairs (dashed lines). All values are based on the B3LYP/6-311+G(d,p) optimized geometries for the ground conformers. The lines are linear regression fits to the data for each series.

Figure 38. B3LYP/6-311+G(d,p) isotropic molecular polarizability distributions of the $(C_nmim:BF_4)$ ion pairs. The mean polarizability and standard deviation are given for each $(C_nmim:BF_4)$ ion pair.

Figure S39. Comparison of B3LYP/6-311+G(d,p) predicted vibrational frequencies (scaled by a factor of 0.9887) versus B3LYP-GD3BJ/6-311+G(2,p) predicted frequencies (unscaled) for the $[2C_nmim:BF_4]^+$ clusters and their $[C_nmim]^+$ and $(C_nmim:BF_4)$ CID products. Data for the $[2C_nmim:BF_4)]^+$ clusters, $[C_nmim]^+$ cations, and $(C_nmim:BF_4)$ ion pairs are shown as open circles, closed circles, and open squares, respectively. Data for the n = 2, 4, 6 and 8 are shown in parts a-d, respectively. The diagonal lines indicate values for which the B3LYP and M06-2X predicted frequencies are equal.

Figure S40. Comparison of B3LYP/6-311+G(d,p) predicted vibrational frequencies (scaled by a factor of 0.9887) versus M06-2X/6-311+G(2,p) predicted frequencies (unscaled) for the $[2C_nmim:BF_4]^+$ clusters and their $[C_nmim]^+$ and ($C_nmim:BF_4$) CID products. Data for the $[2C_nmim:BF_4)]^+$ clusters, $[C_nmim]^+$ cations, and ($C_nmim:BF_4$) ion pairs are shown as open circles, closed circles, and open squares, respectively. Data for the n = 2, 4, 6 and 8 are shown in parts a-d, respectively. The diagonal lines indicate values for which the B3LYP and M06-2X predicted frequencies are equal.

Figure S41. Zero-pressure-extrapolated cross section for collision-induced dissociation of the $[2C_nmim:BF_4]^+$ IL clusters with Xe as a function of the collision energy in the center-of-mass frame (lower *x*-axis) and laboratory frame (upper *x*-axis); data for n = 2, 4, 6 and 8 are shown in parts a-d, respectively. The solid lines show the best fits to the data convoluted over the neutral and ion kinetic and internal energy distributions. The dashed lines show the model cross sections in the absence of experimental kinetic energy broadening for reactants with an internal energy corresponding to 0 K.

Figure S42. Comparison of M06-2X computed 0 K BDEs versus measured TCID 0 K BDEs of the $[2C_nmim:BF_4]^+$ IL clusters for n = 2, 4, 6, and 8 All theoretical values include ZPE corrections. Values indicated with open symbols also include BSSE corrections, whereas those indicated with closed symbols do not include BSSE corrections. The diagonal line indicates values for which the calculated and measured values are equal.

Figure S43. Comparison of B3LYP, B3LYP-GD3BJ, and M06-2X computed 0 K BDEs versus measured threshold dissociation energies of the $[2C_nmim:BF_4]^+$ IL clusters for n = 2, 4, 6, and 8 for thermochemical analyses that make use of the molecular parameters of the precursor clusters and CID products determined using the same functional with a 6-311+G(2d,2p) basis set. All theoretical values include ZPE corrections. The B3LYP and B3LYP-GD3BJ values also include BSSE corrections; whereas the M06-2X values plotted do not include BSSE corrections. The diagonal line indicates values for which the calculated and measured values are equal.

Figure S1.

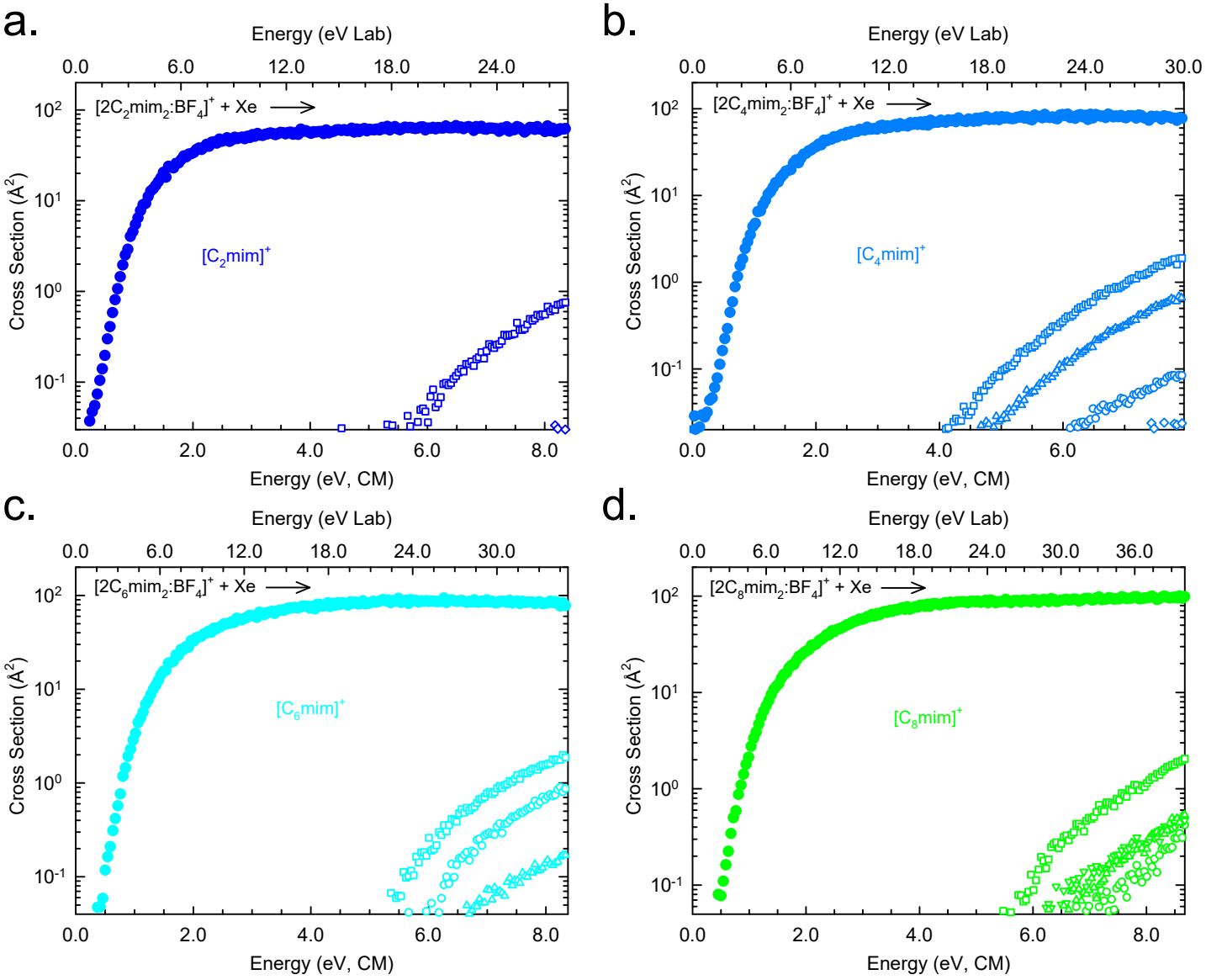
a.
Energy (eV Lab)
0.0
6.0
12.0
18.0
24.0
[2C2mim2:BF4]+ + Xe
[C2mim]+
Cross Section (Å2)
Energy (eV, CM)
b.
30.0
[2C4mim2:BF4]+ + Xe
[C4mim]+
c.
[2C6mim2:BF4]+ + Xe
[C6mim]+
d.
36.0
[2C8mim2:BF4]+ + Xe
[C8mim]+

Figure S2.

$[C_n mim]^+$ Nomenclature

$[a1a2\ldots an\text{-}1]^+$

$[C_2mim]^+ = [a1]^+$

$[C_4mim]^+ = [a1a2a3]^+$

$[C_6mim]^+ = [a1a2a3a4a5]^+$

$[C_8mim]^+ = [a1a2a3a4a5a6a7]^+$

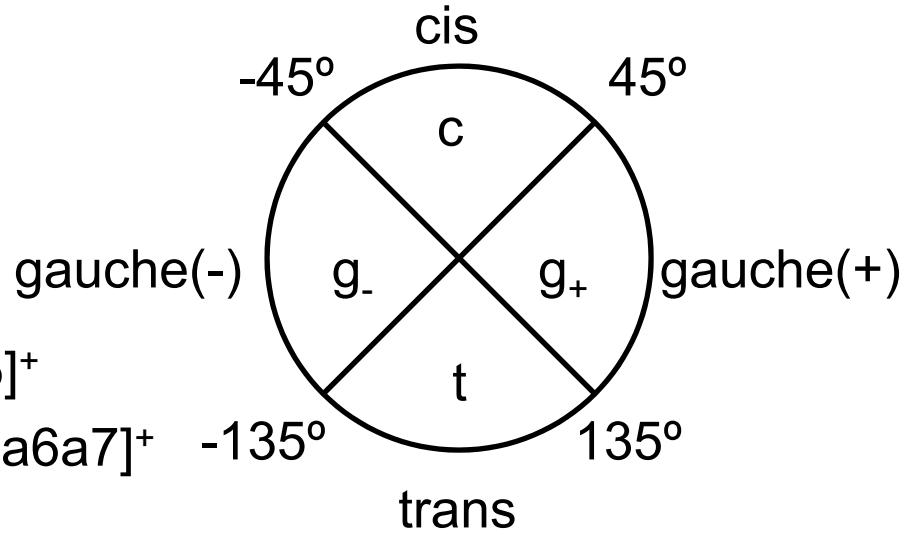

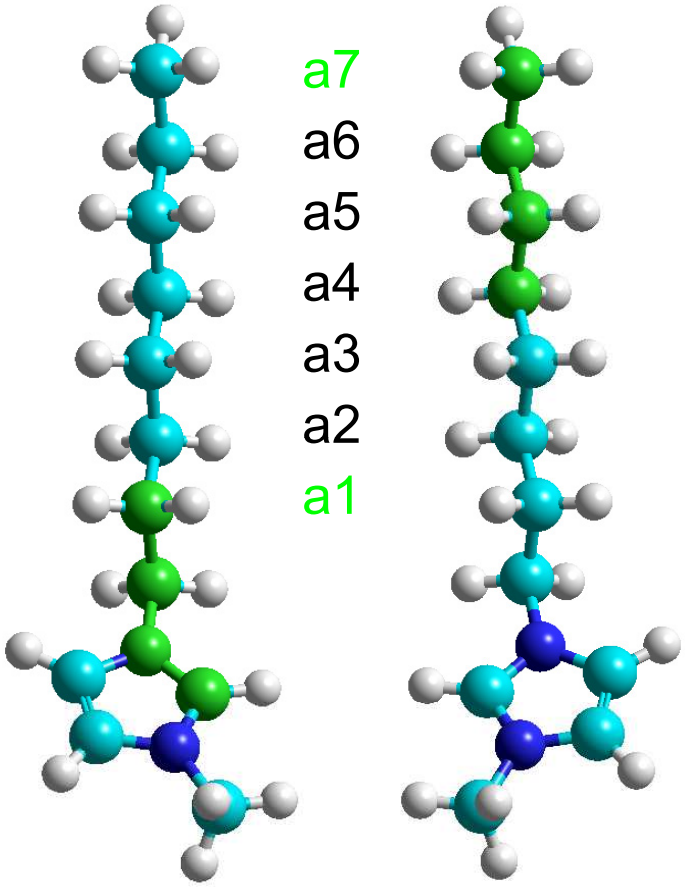

$[g_-ttttt]^+$ $[g_+ttttt]^+$

$[g_-t_6]^+$ $[g_+t_6]^+$

$[C_8mim]^+$

Dihedral Angle Classification

1-Alkyl Dihedral Angles

a1 = ∠C2N1C1′C2′
a2 = ∠N1C1′C2′C3′
a3 = ∠C1′C2′C3′C4′
a4 = ∠C2′C3′C4′C5′
a5 = ∠C3′C4′C5′C6′
a6 = ∠C4′C5′C6′C7′
a7 = ∠C5′C6′C7′C8′

Figure S2.

Binding Site (BS) Nomenclature

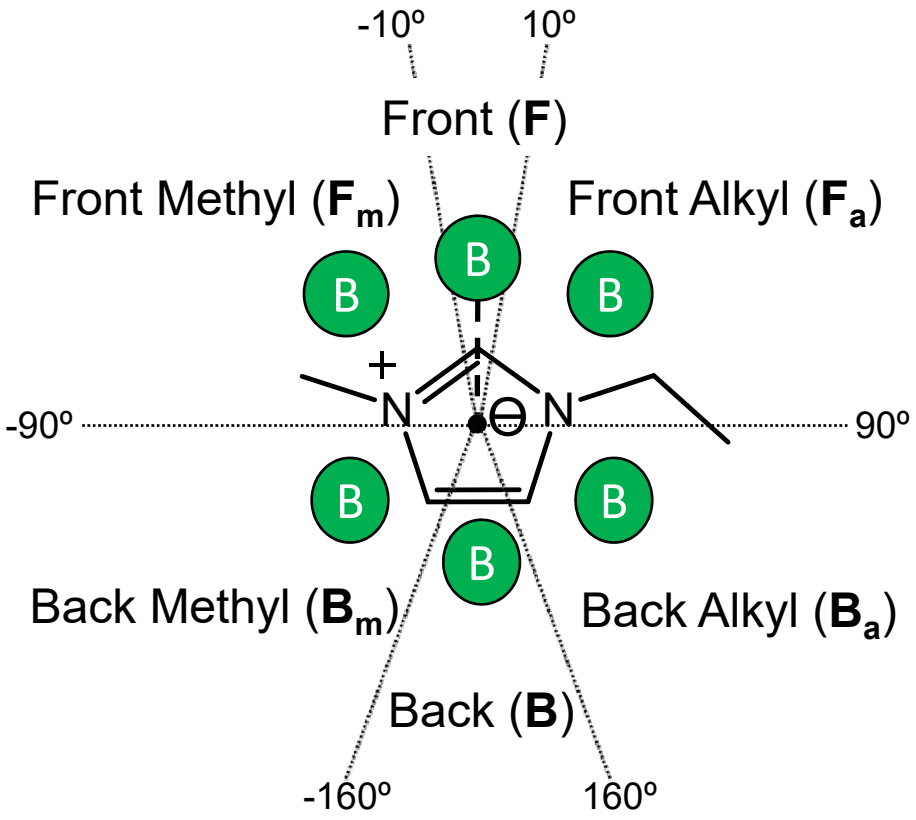

The **binding site** (**BS**) designation is readily described by the dihedral angle **b** = ∠(C2,©,©+CP,B), where © denotes the centroid of the imidazolium ring (N1C2N3C4C5) and CP denotes the cross product of the vectors that describe the C2-N1 and C2-N3 bonds, i.e., CP = $\overrightarrow{(C2\text{-}N1)}x\overrightarrow{(C2\text{-}N3)}$. The range of angles that define BS designations are shown in the figure above and the bar below.

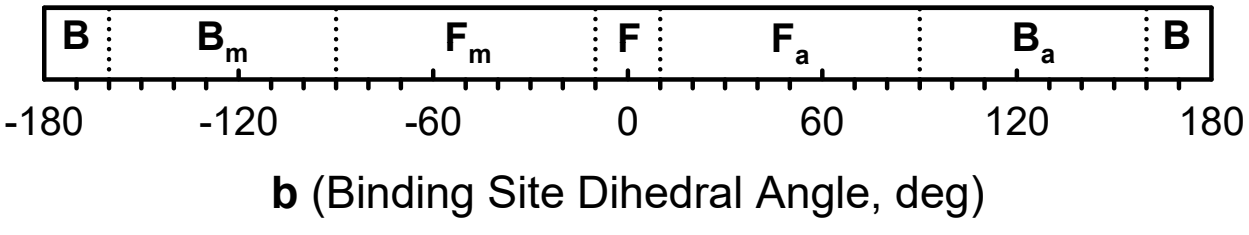

Figure S2.

Binding Site (BS) Nomenclature

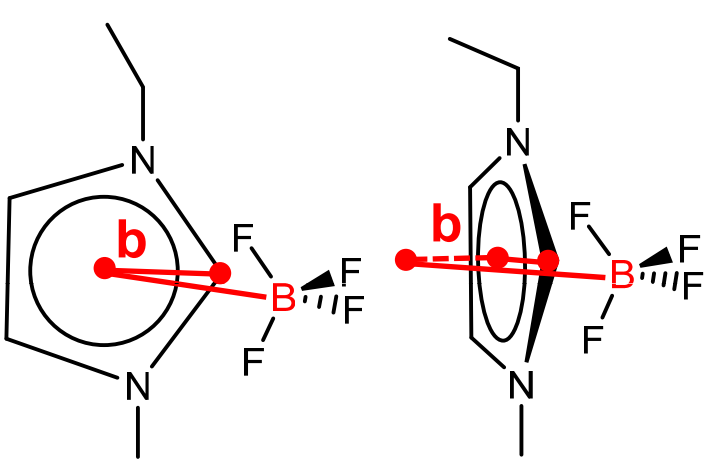

Front Binding (**F**)

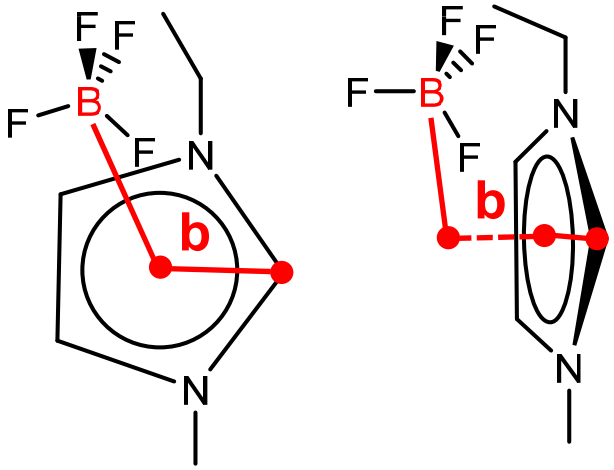

Back Alkyl Binding ($\mathbf{B_a}$)

The **binding site** (**BS**) designation is readily described by the dihedral angle **b** = ∠(C2,©,©+CP,B), where © denotes the centroid of the imidazolium ring (N1C2N3C4C5) and CP denotes the cross product of the vectors that describe the C2-N1 and C2-N3 bonds, i.e., CP = $\overrightarrow{(C2\text{-}N1)}x\overrightarrow{(C2\text{-}N3)}$. The range of angles that define BS designations are shown in the figure above and the bar below.

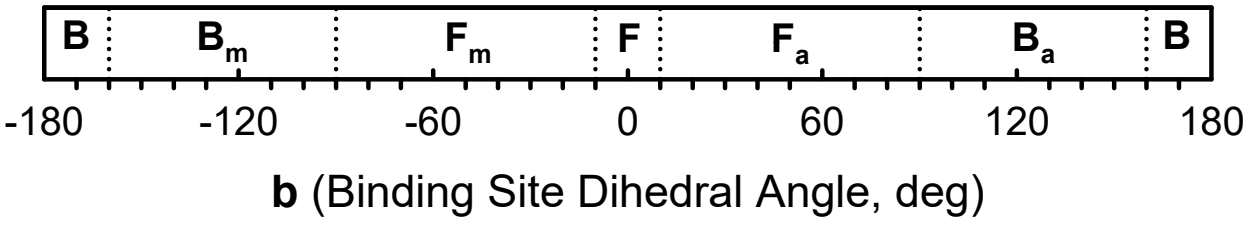

Figure S2.

($C_n$mim:BF_4) Nomenclature

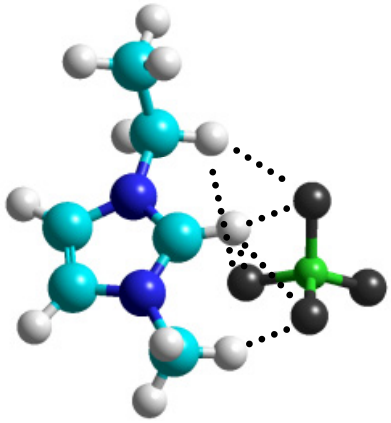

(C_2mim:BF_4)

(**g$_+$F**;g$_-$)

(**Binding Site**;Alkyl)

(**b1BS**;a1…an)

b1 = ∠C1″N3C2B

[2$C_n$mim:BF_4]$^+$ Nomenclature

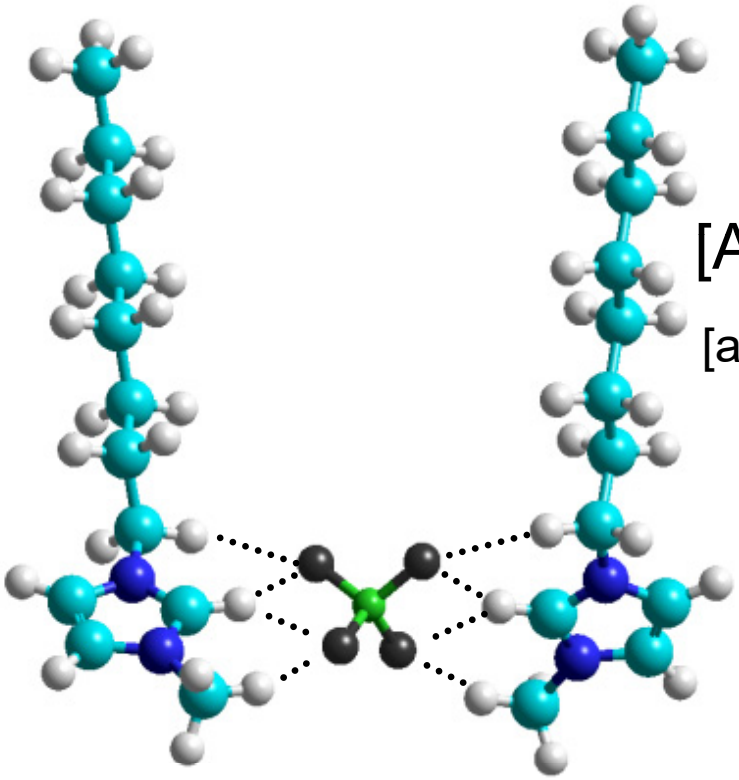

[2C_8mim:BF_4]$^+$

[g$_-$t$_6$;**g$_+$cFcF**;g$_-$t$_6$]$^+$

[Alkyl1;**BindingSites**;Alkyl2]$^+$

[a1…an;**b2b1BS(1)b1BS(2)**; a1…an]$^+$

b2 = ∠C1′(1)N1(1)N1(2)C1′(2)

Figure S3.

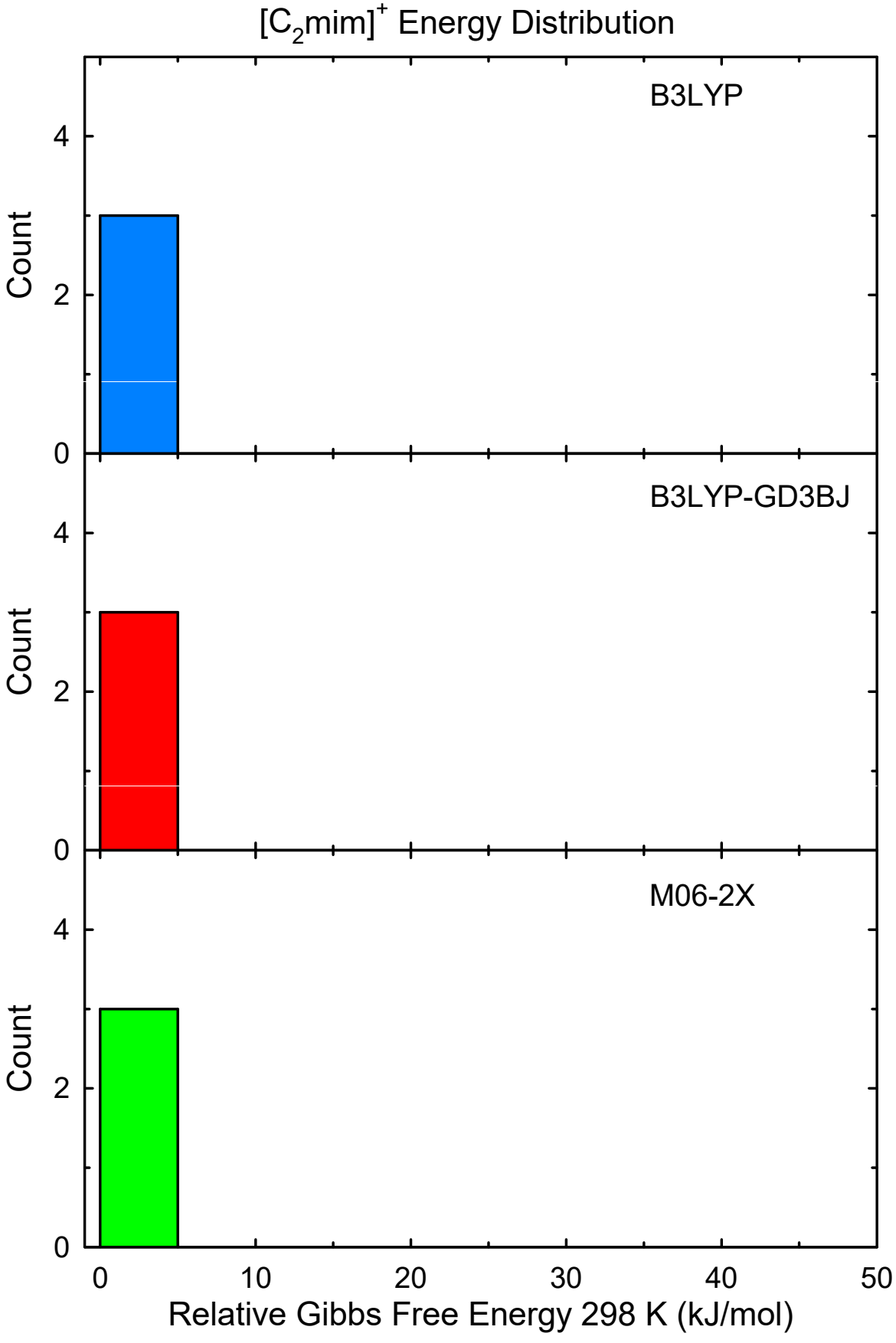
[C2mim]+ Energy Distribution
B3LYP
B3LYP-GD3BJ
M06-2X
Count
Count
Count
0
2
4
0
2
4
0
2
4
0
10
20
30
40
50
Relative Gibbs Free Energy 298 K (kJ/mol)

Figure S4.

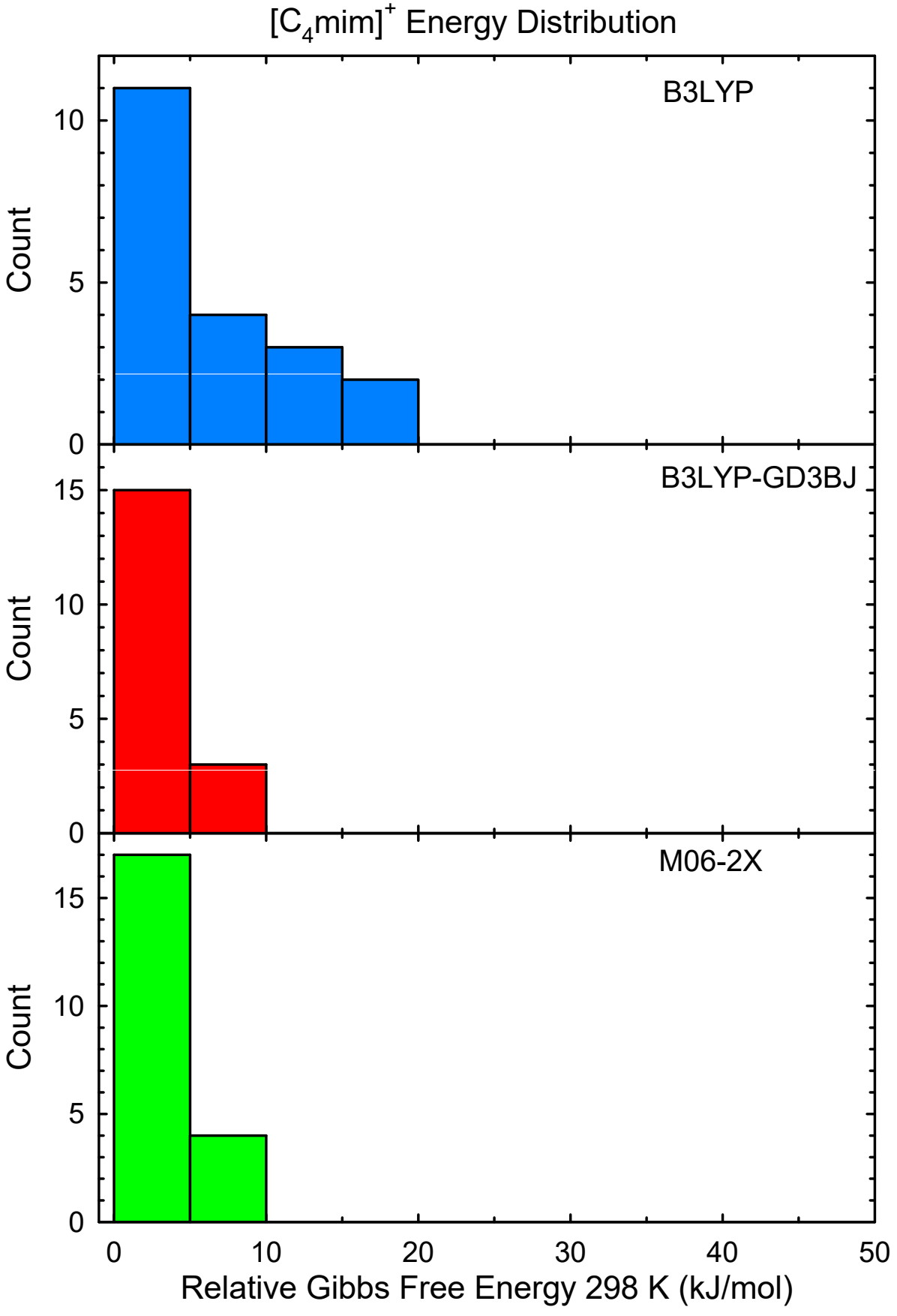
[C4mim]+ Energy Distribution
B3LYP
B3LYP-GD3BJ
M06-2X
Count
Count
Count
0
5
10
0
5
10
15
0
5
10
15
0
10
20
30
40
50
Relative Gibbs Free Energy 298 K (kJ/mol)

Figure S5.

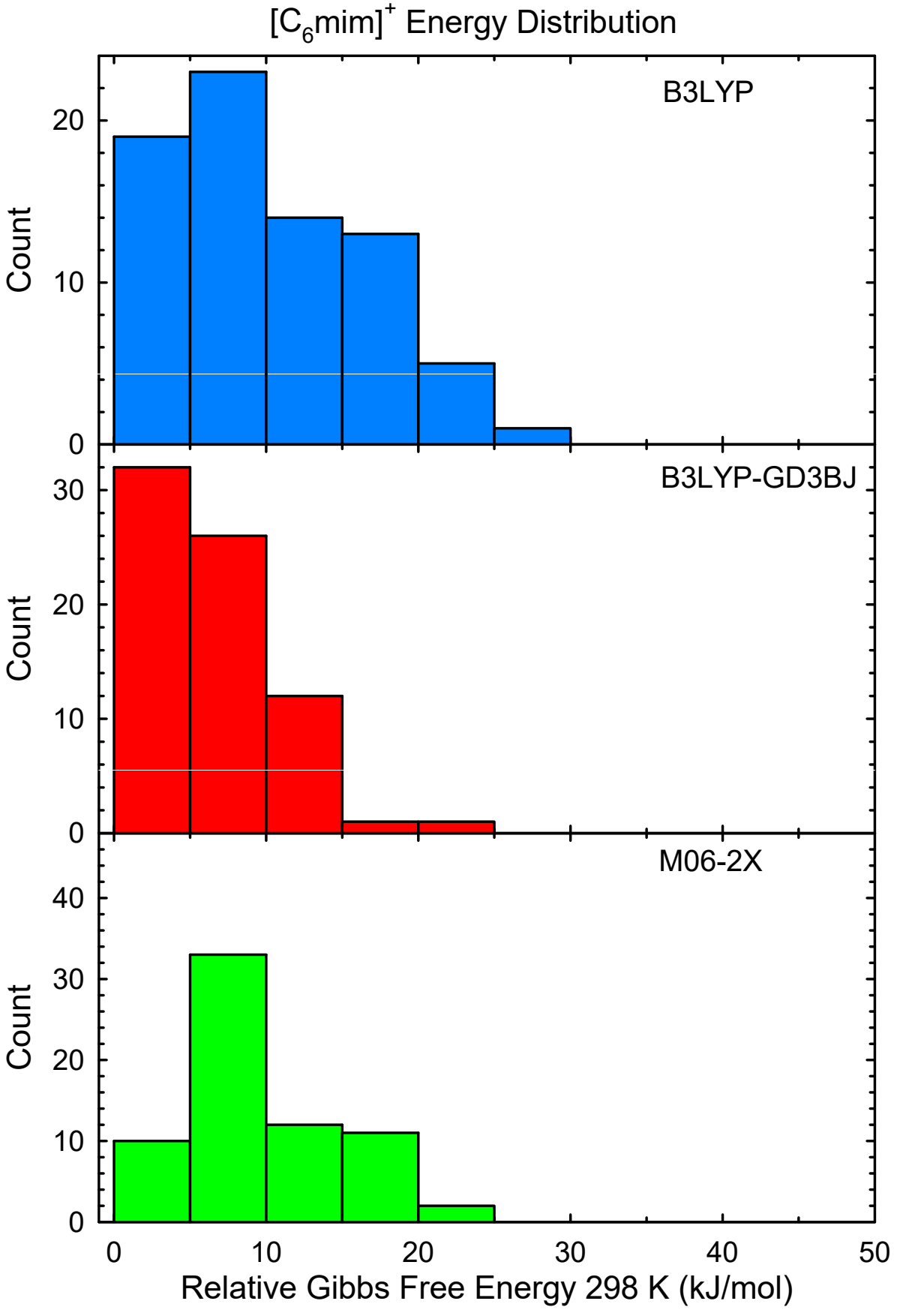
[C6mim]+ Energy Distribution
B3LYP
B3LYP-GD3BJ
M06-2X
Count
Count
Count
0
10
20
0
10
20
30
0
10
20
30
40
0
10
20
30
40
50
Relative Gibbs Free Energy 298 K (kJ/mol)

Figure S6.

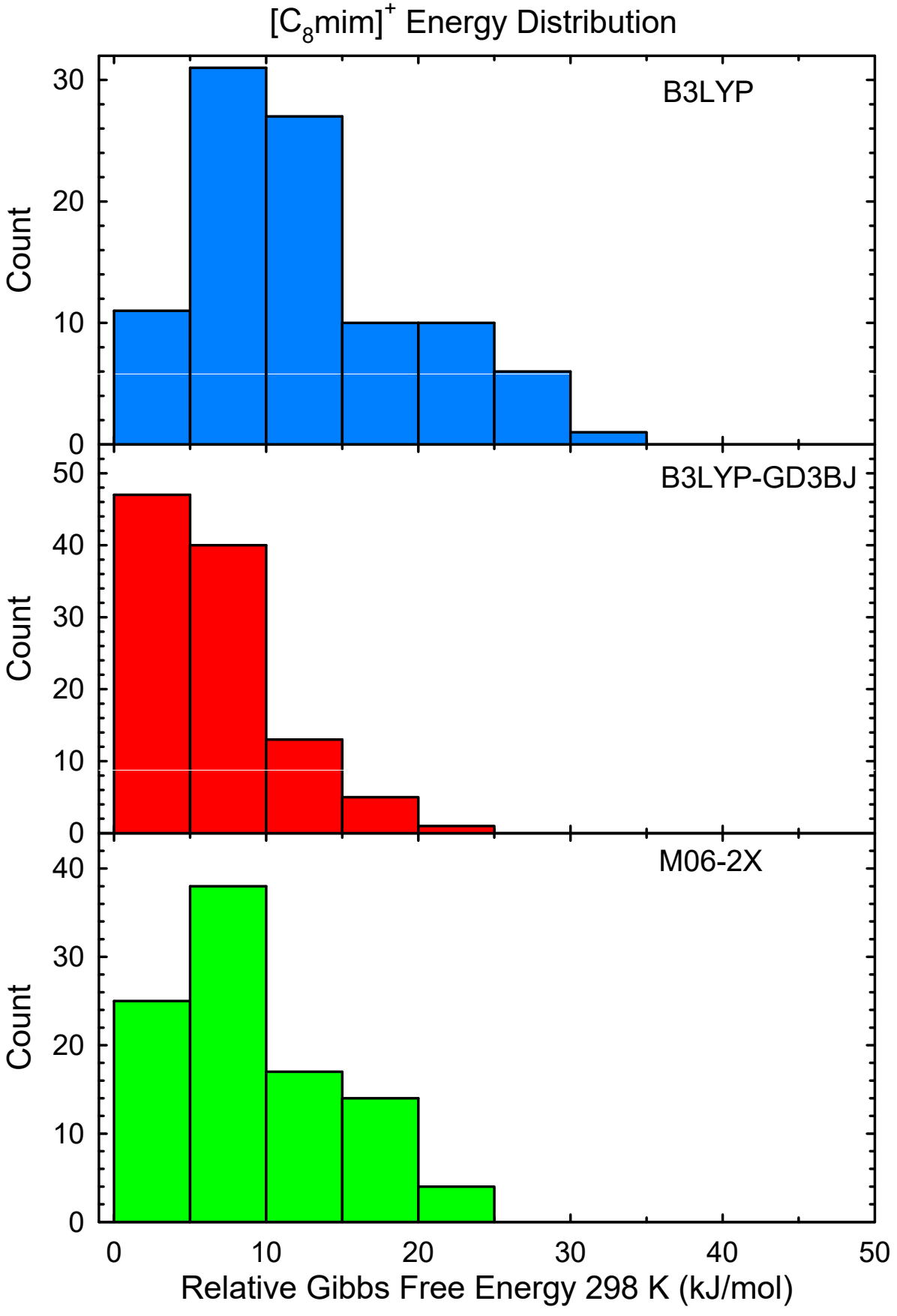
[C8mim]+ Energy Distribution
B3LYP
B3LYP-GD3BJ
M06-2X
Count
Count
Count
0
10
20
30
40
50
Relative Gibbs Free Energy 298 K (kJ/mol)

Figure S7.

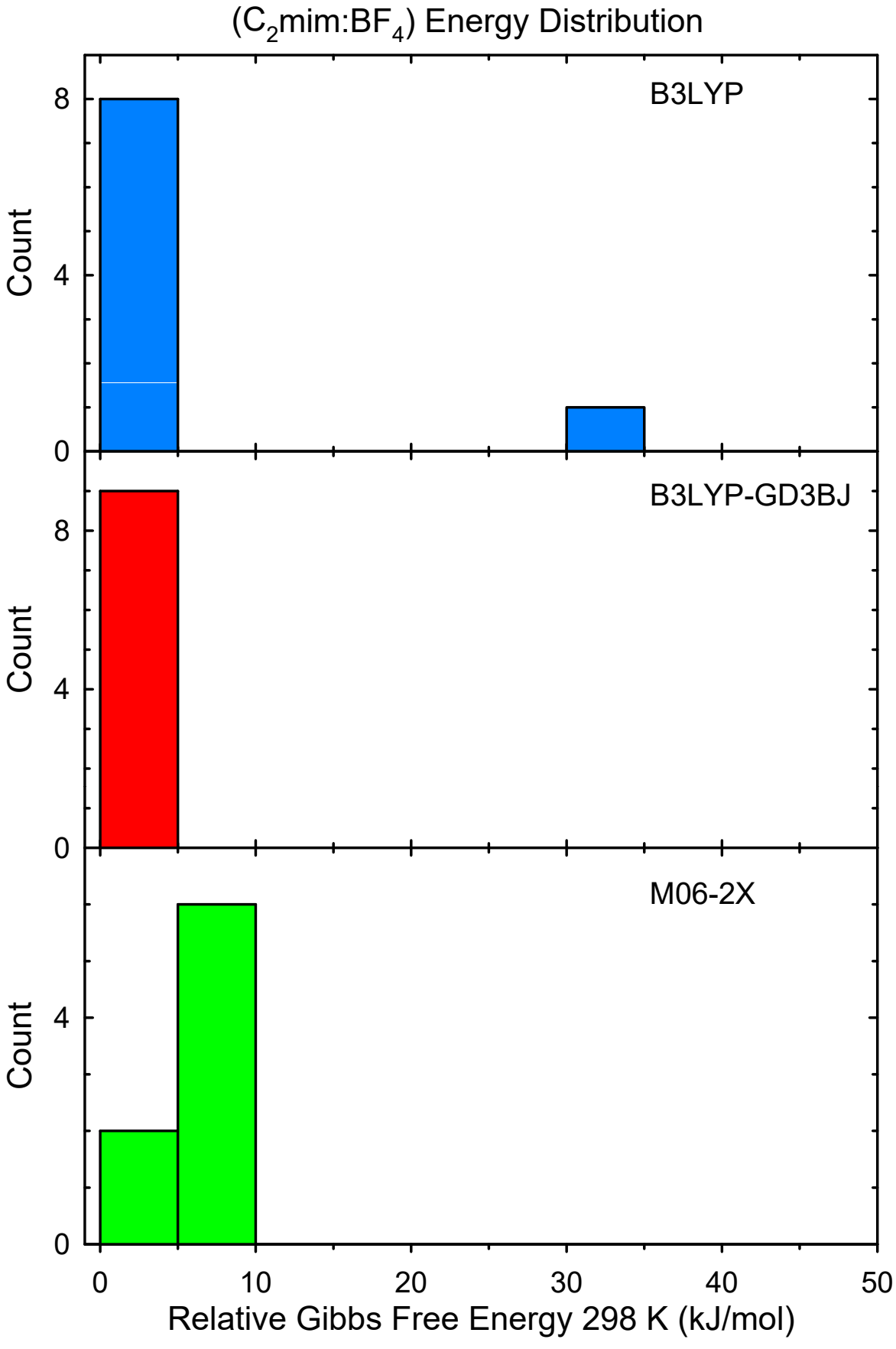
(C_2mim:BF_4) Energy Distribution
B3LYP
B3LYP-GD3BJ
M06-2X
Count
Count
Count
8
4
0
8
4
0
4
0
0
10
20
30
40
50
Relative Gibbs Free Energy 298 K (kJ/mol)

Figure S8.

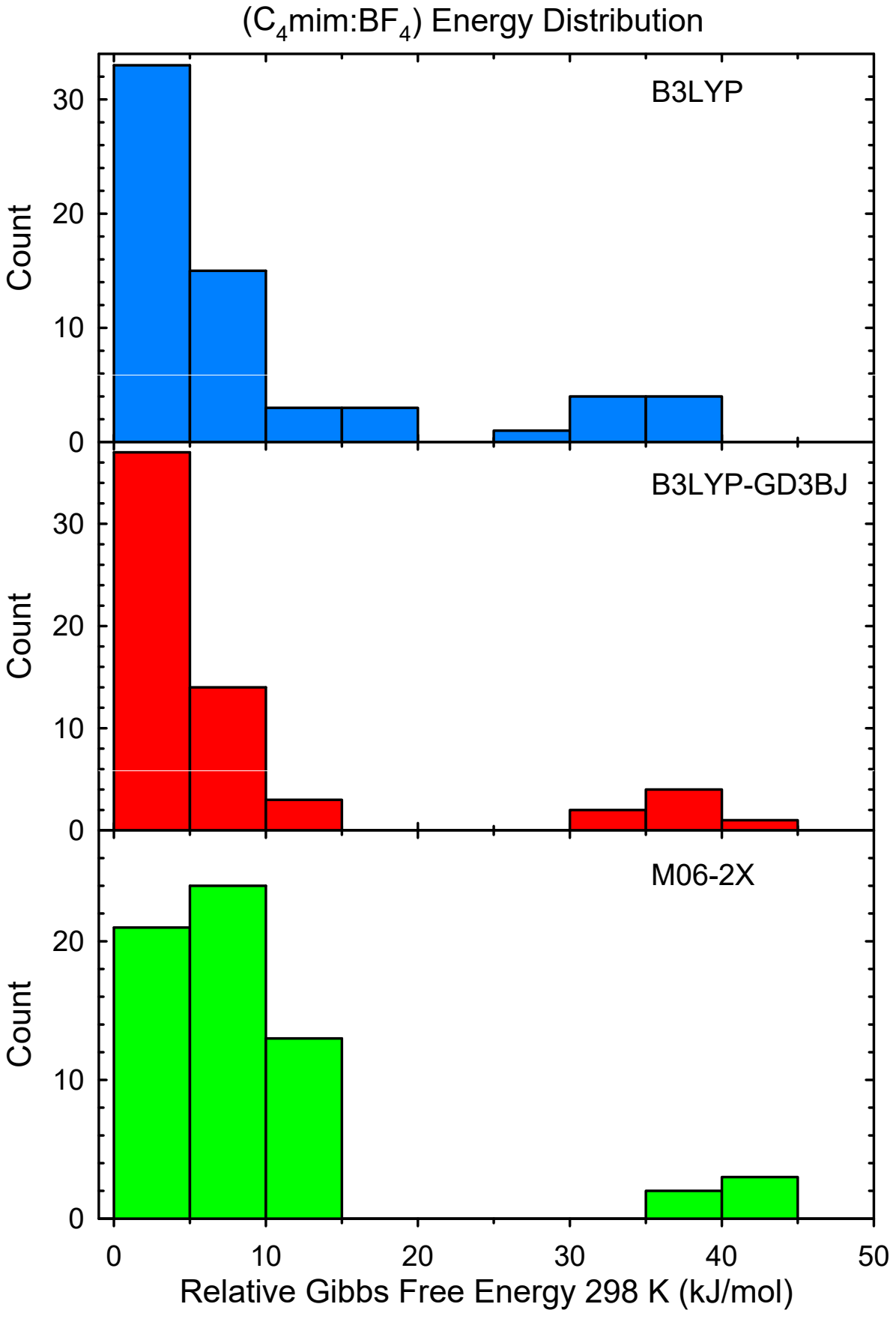
(C_4mim:BF_4) Energy Distribution
B3LYP
B3LYP-GD3BJ
M06-2X
Count
Count
Count
0
10
20
30
0
10
20
30
40
50
Relative Gibbs Free Energy 298 K (kJ/mol)

Figure S9.

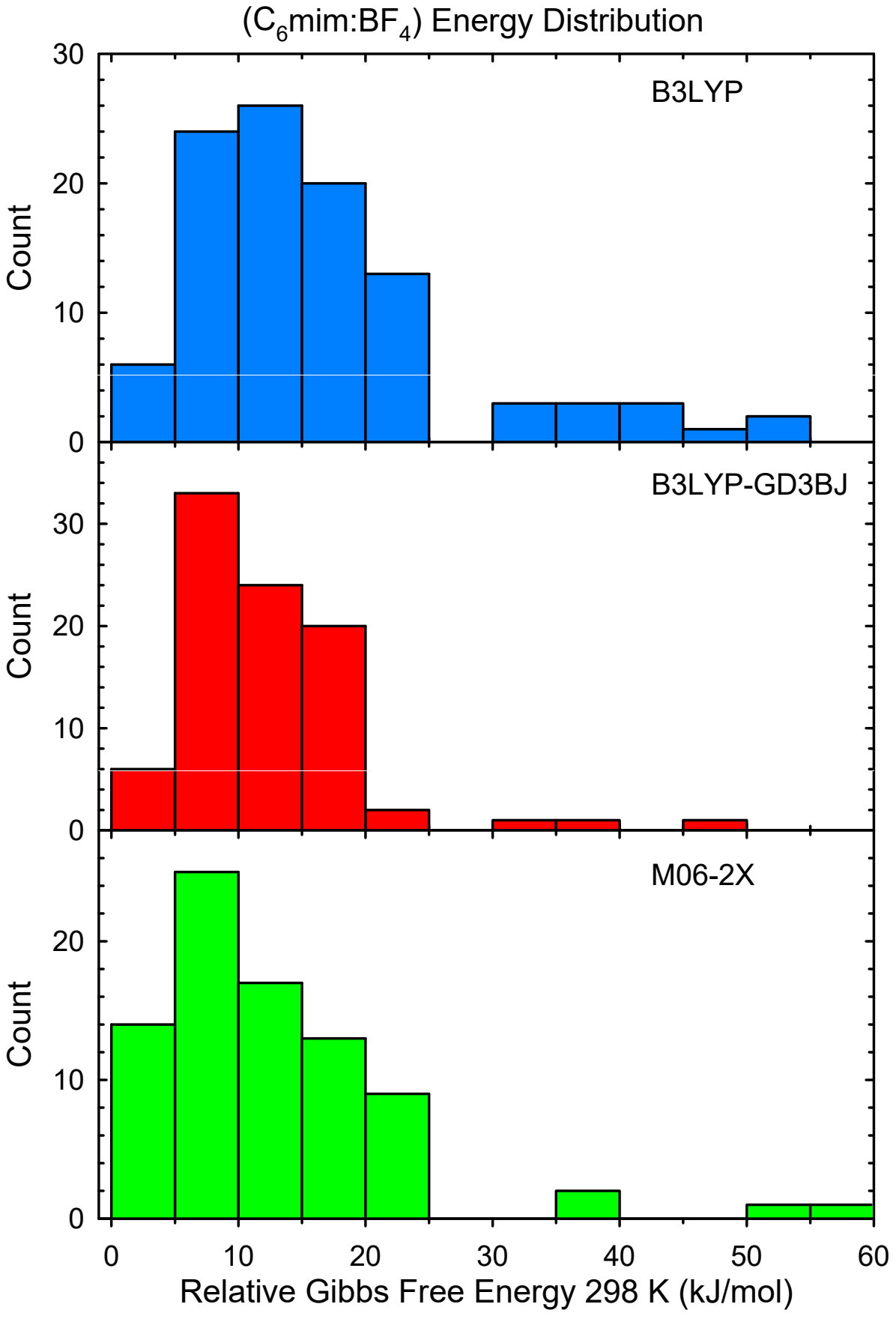
(C_6mim:BF_4) Energy Distribution
B3LYP
B3LYP-GD3BJ
M06-2X
Count
Count
Count
Relative Gibbs Free Energy 298 K (kJ/mol)
0
10
20
30
40
50
60

Figure S10.

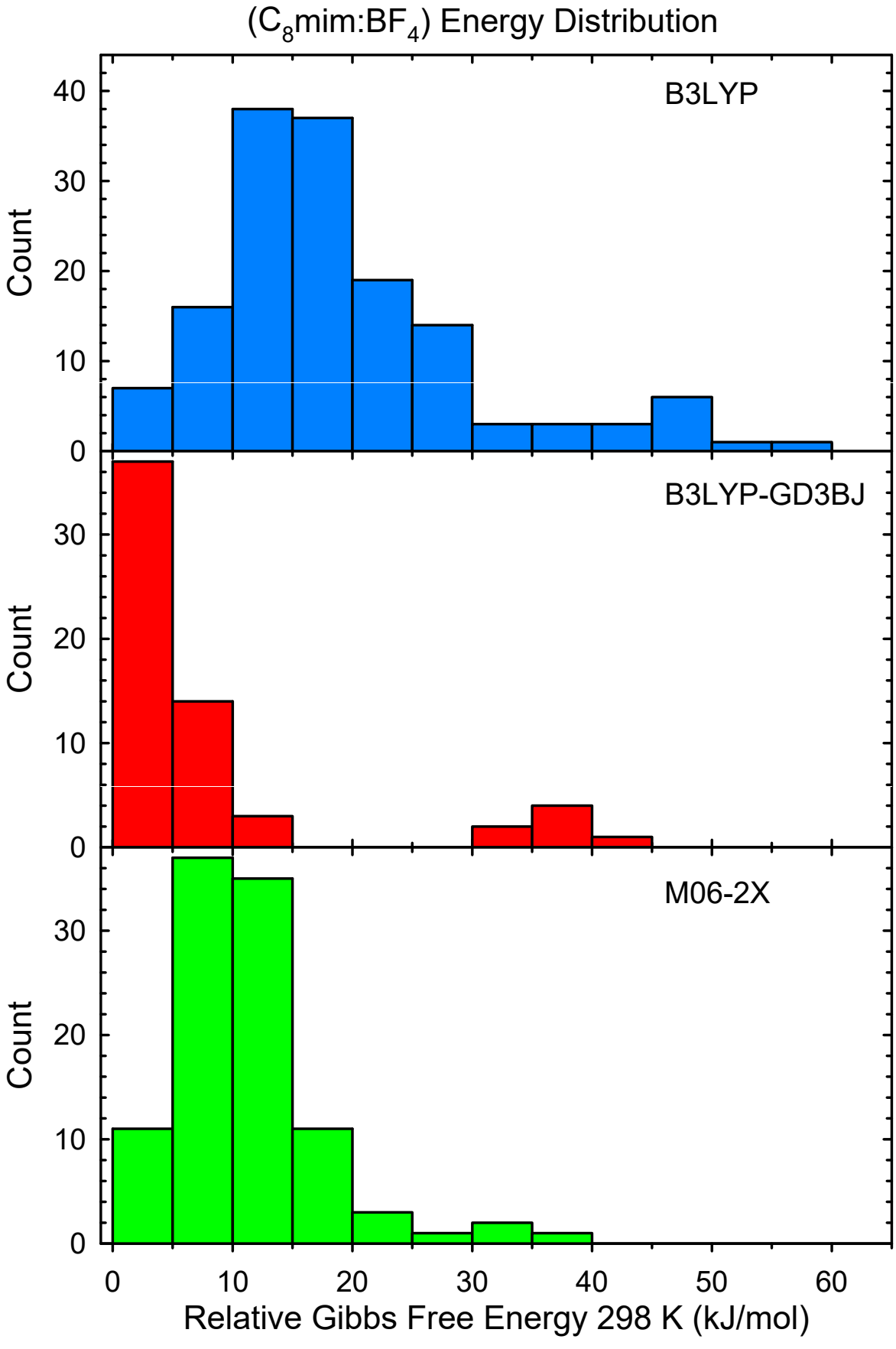
(C_8mim:BF_4) Energy Distribution
B3LYP
B3LYP-GD3BJ
M06-2X
Count
Count
Count
0
10
20
30
40
50
60
Relative Gibbs Free Energy 298 K (kJ/mol)

Figure S11.

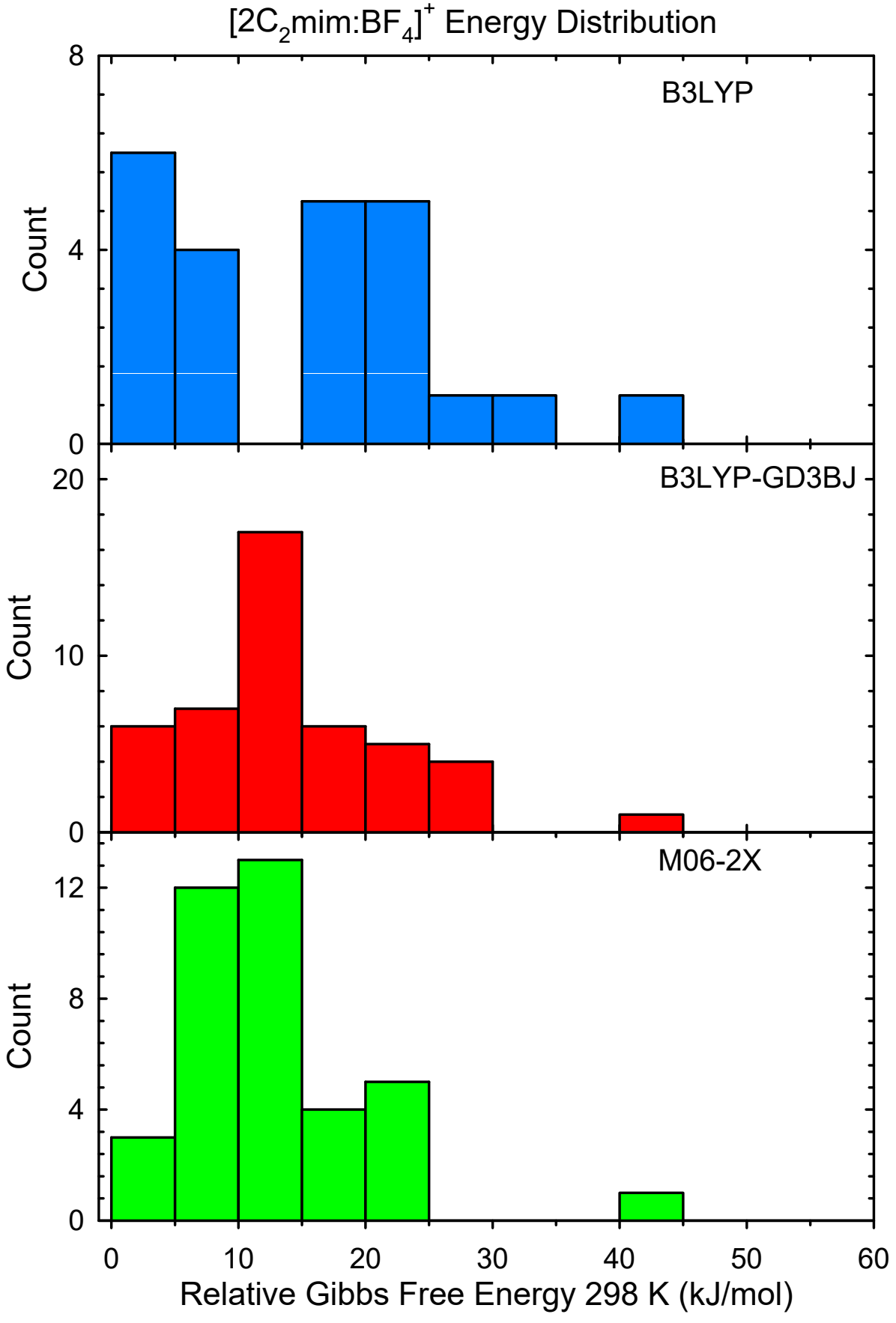
[2C2mim:BF4]+ Energy Distribution
B3LYP
B3LYP-GD3BJ
M06-2X
Count
Count
Count
0
4
8
0
10
20
0
4
8
12
0
10
20
30
40
50
60
Relative Gibbs Free Energy 298 K (kJ/mol)

Figure S12.

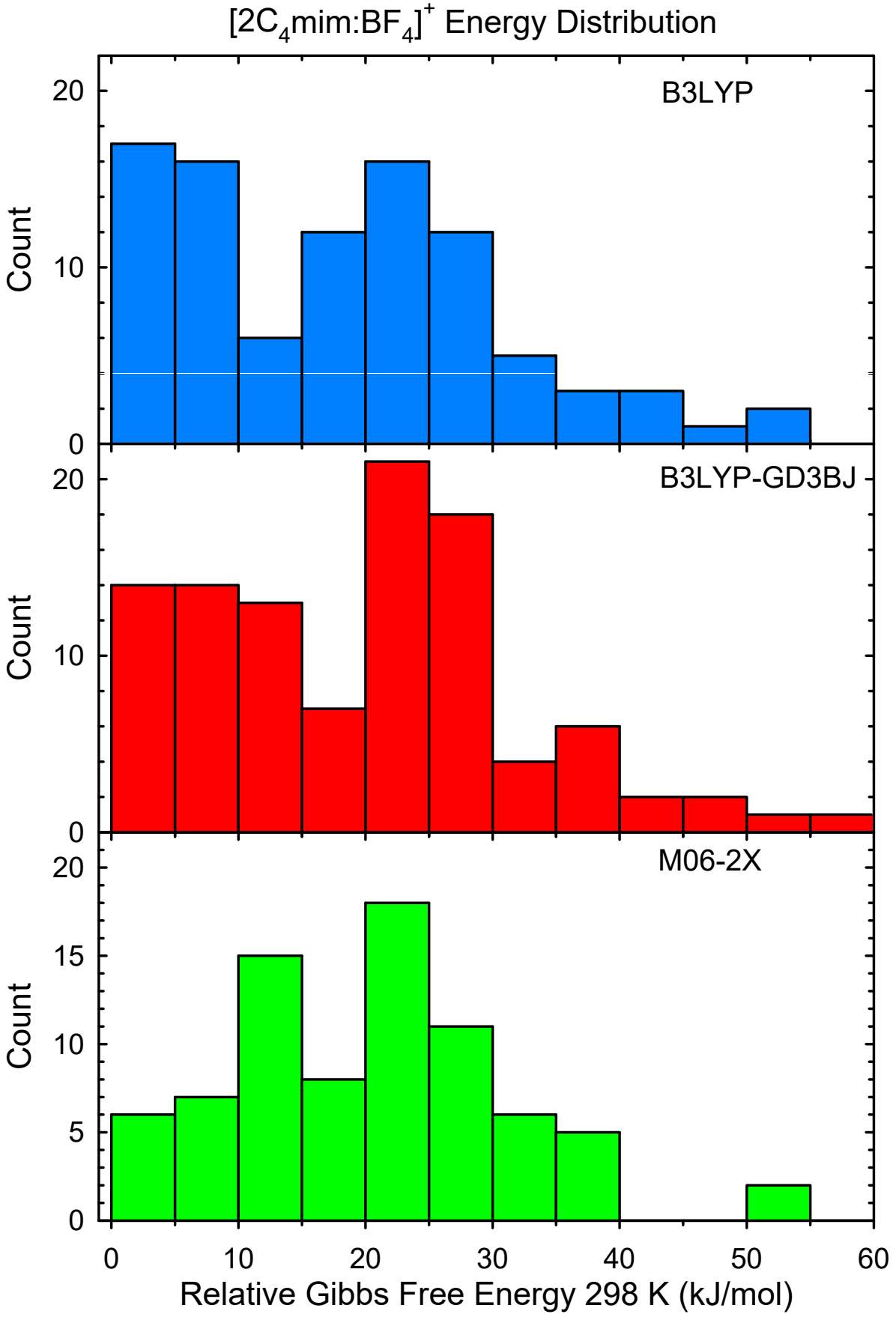
[2C4mim:BF4]+ Energy Distribution
B3LYP
B3LYP-GD3BJ
M06-2X
Count
Count
Count
0
10
20
0
10
20
0
10
20
0
5
10
15
0
10
20
30
40
50
60
Relative Gibbs Free Energy 298 K (kJ/mol)

Figure S13.

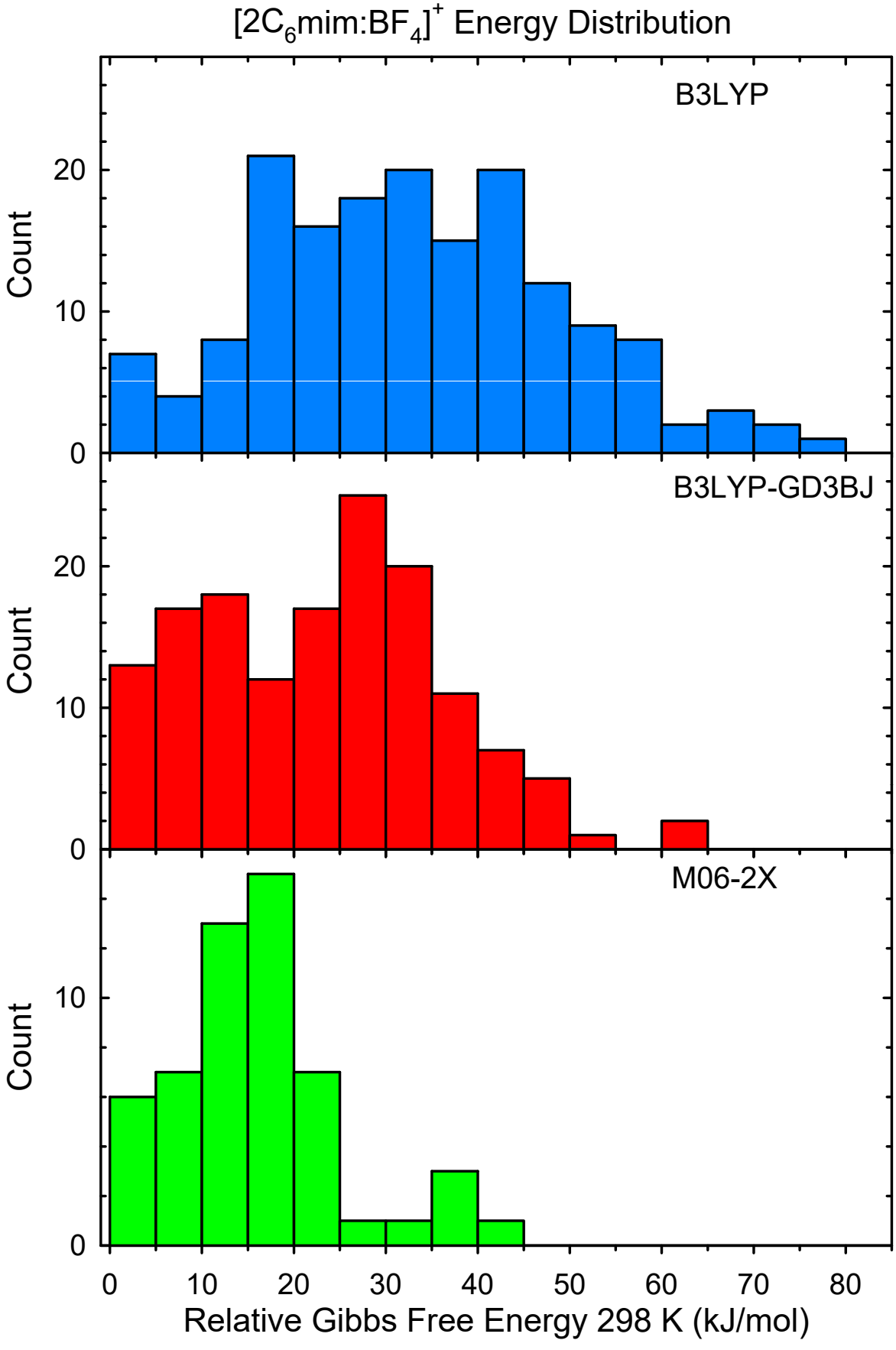
[2C6mim:BF4]+ Energy Distribution
B3LYP
B3LYP-GD3BJ
M06-2X
Count
Count
Count
0
10
20
0
10
20
0
10
0
10
20
30
40
50
60
70
80
Relative Gibbs Free Energy 298 K (kJ/mol)

Figure S14.

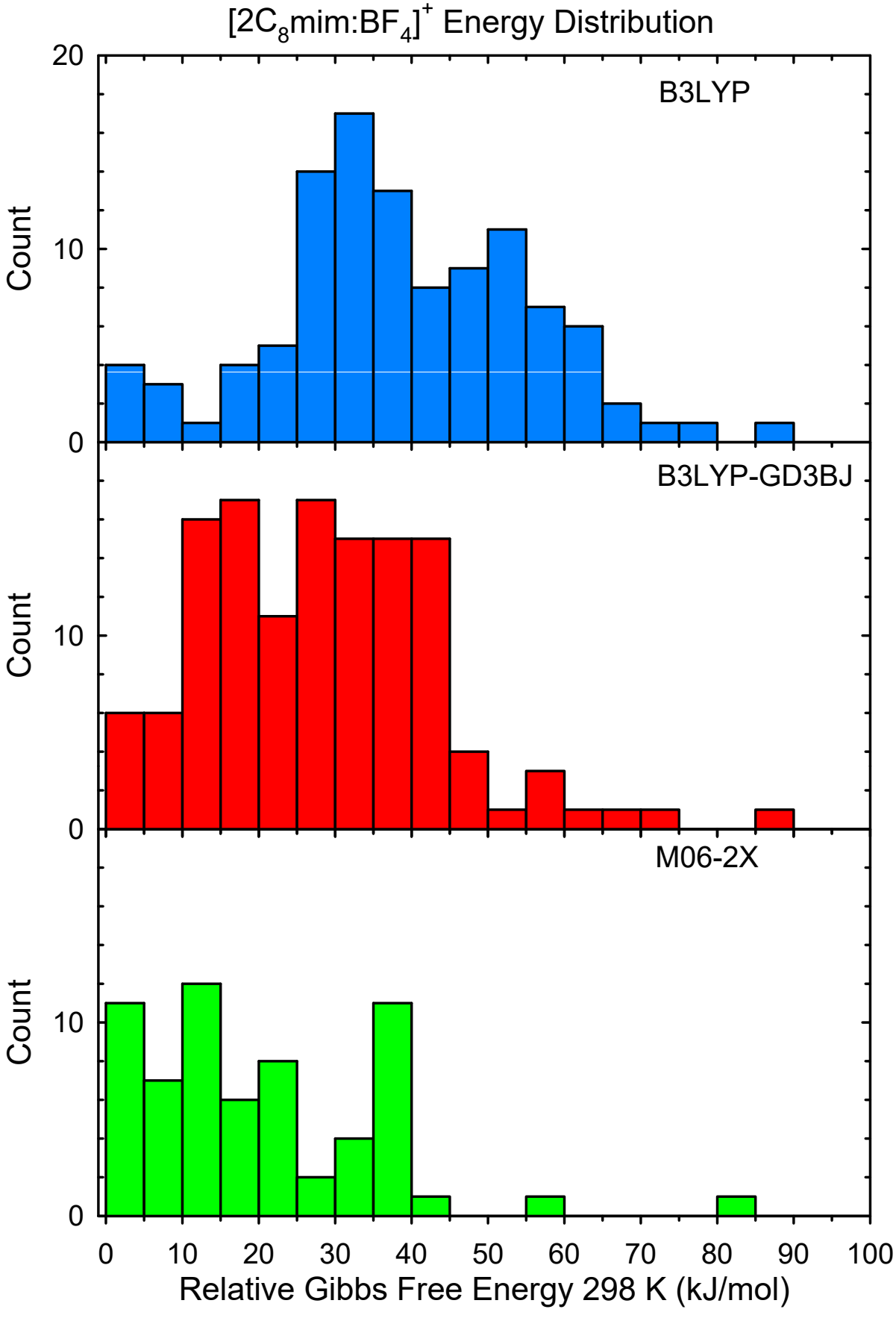
[2C8mim:BF4]+ Energy Distribution
B3LYP
B3LYP-GD3BJ
M06-2X
Count
Count
Count
20
10
0
10
0
10
0
0
10
20
30
40
50
60
70
80
90
100
Relative Gibbs Free Energy 298 K (kJ/mol)

Figure S15.

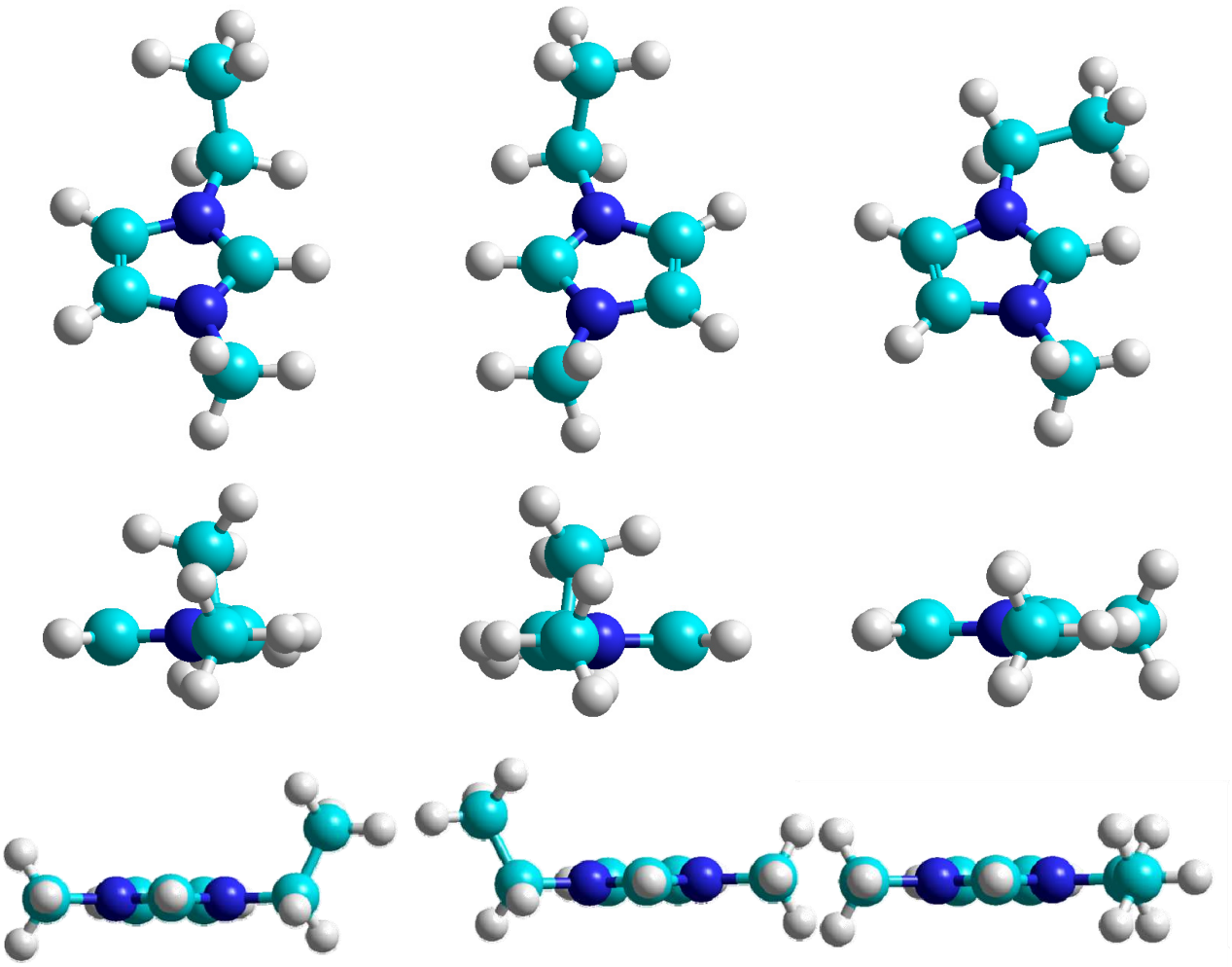

$[g_-]^+$
0.0,0.0, 0.0 kJ/mol

$[g_+]^+$
0.1, 0.1, 0.0 kJ/mol

$[c]^+$
1.1, 1.1, 2.5 kJ/mol

$[C_2mim]^+$

Figure S16.

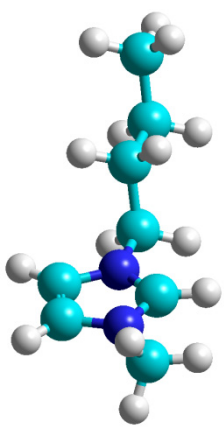

$[g_-t_2]^+$
0.0, 0.5, 1.0 kJ/mol

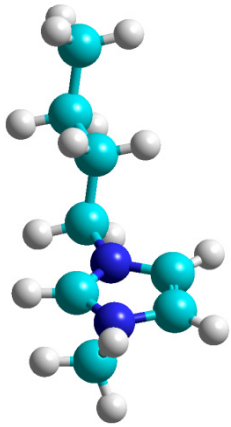

$[g_+t_2]^+$
0.5, 0.8, 1.0 kJ/mol

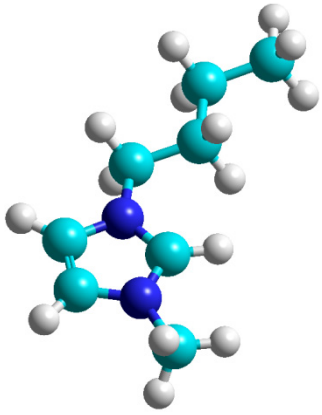

$[ct_2]^+$
2.8, 2.3, 0.8 kJ/mol

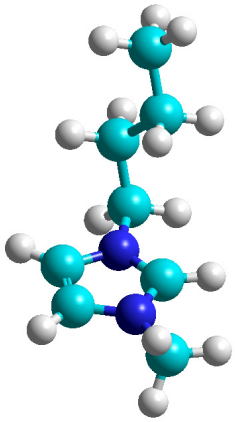

$[g_-g_+t]^+$
2.9, 0.0, 0.0 kJ/mol

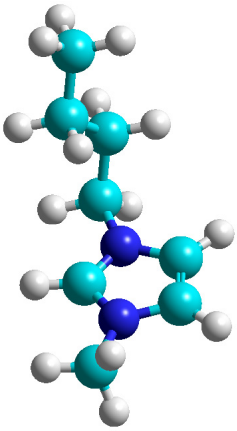

$[g_+g_-t]^+$
2.9, 0,0, 0.0 kJ/mol

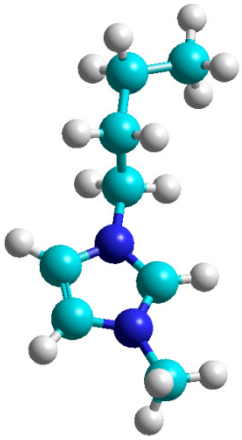

$[g_-tg_-]^+$
2.9, 1.9, 3.7 kJ/mol

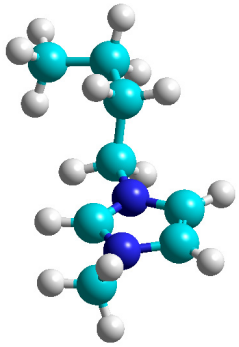

$[g_+tg_+]^+$
3.0, 1.9, 3.7 kJ/mol

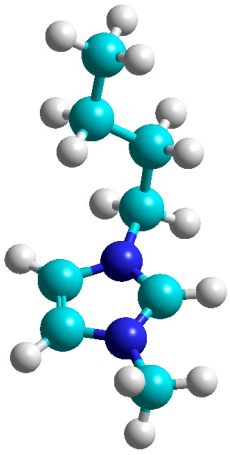

$[g_{-2}t]^+$
3.4, 0.8, 1.4 kJ/mol

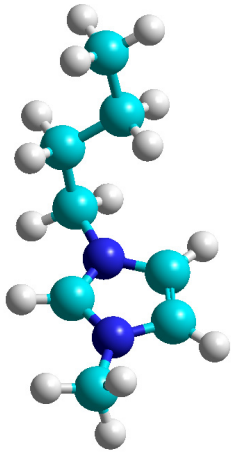

$[g_{+2}t]^+$
3.5, 0.8,1.4 kJ/mol

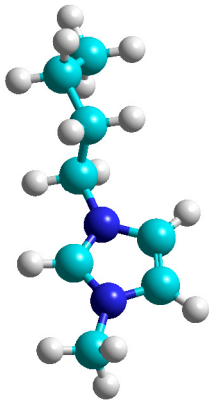

$[g_+tg_-]^+$
4.0, 2.9, 1.1 kJ/mol

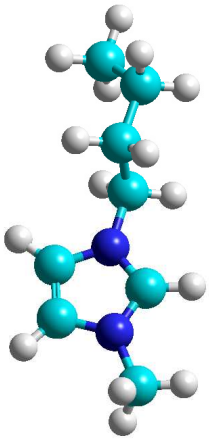

$[g_-tg_+]^+$
4.0, 2.9, 1.1 kJ/mol

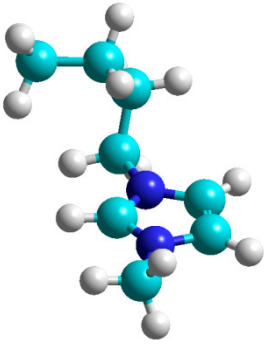

$[g_+g_{-2}]^+$
6.2, 2.9, 1.6 kJ/mol

$[C_4mim]^+$

Figure S17.

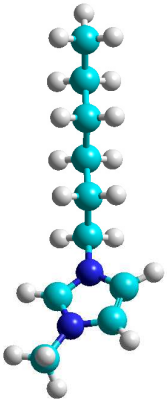

$[g_+t_4]^+$
0.0, 2.1, 2.3* kJ/mol

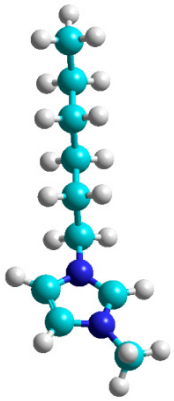

$[g_-t_4]^+$
0.1, 2.1, 2.3* kJ/mol

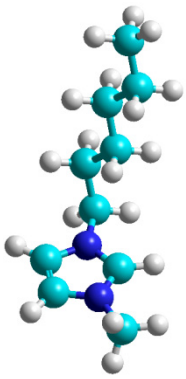

$[g_-g_+t_3]^+$
1.4, 0.0, 0.0 kJ/mol

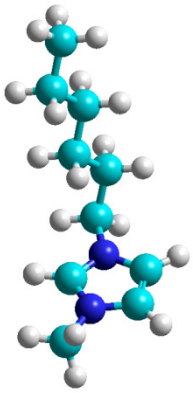

$[g_+g_-t_3]^+$
1.4, 0.0, 0.0 kJ/mol

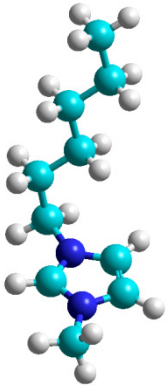

$[g_{+2}t_3]^+$
3.1, 2.6, 5.4 kJ/mol

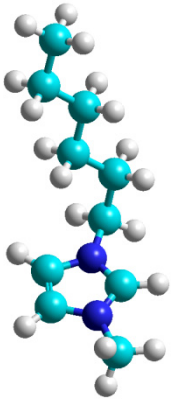

$[g_{-2}t_3]^+$
3.1, 2.6, 5.4 kJ/mol

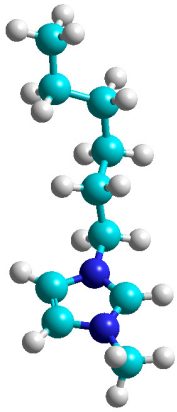

$[g_-t_2g_-t]^+$
3.8, 3.6, 6.5 kJ/mol

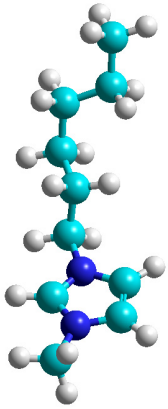

$[g_+t_2g_+t]^+$
3.8, 3.6, 6.5 kJ/mol

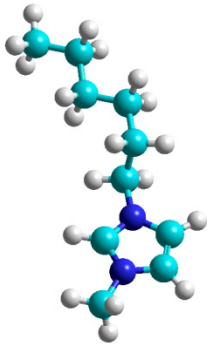

$[g_+tg_+t_2]^+$
3.5, 4.2, 3.0 kJ/mol

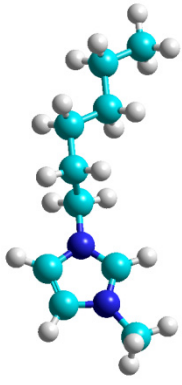

$[g_-tg_-t_2]^+$
3.5, 4.2, 3.0 kJ/mol

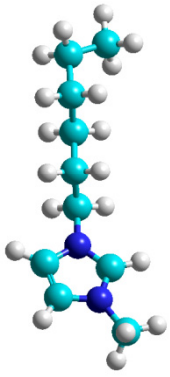

$[g_-t_3g_-]^+$
3.9, 4.4, 6.0 kJ/mol

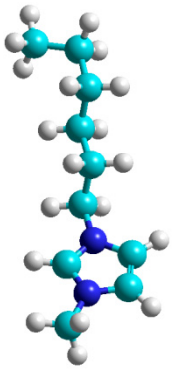

$[g_+t_3g_+]^+$
3.9, 4.5, 5.9 kJ/mol

$[C_6mim]^+$

Figure S18.

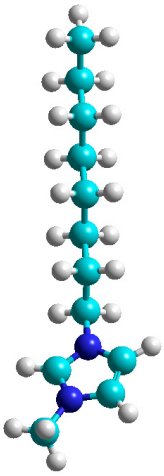

$[g_+t_6]^+$
0.0, 1.2, 3.8 kJ/mol

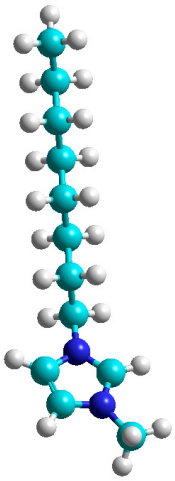

$[g_-t_6]^+$
0.1, 1.2, 3.7 kJ/mol

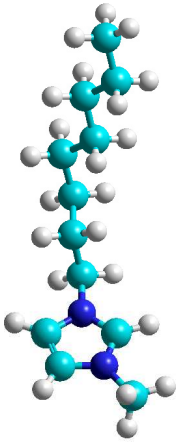

$[g_-t_2g_+t_3]^+$
0.4, 4.0, 4.0 kJ/mol

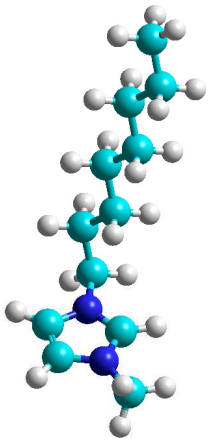

$[g_-g_+t_5]^+$
1.6, 0.0, 0.0 kJ/mol

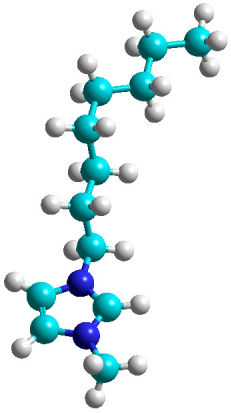

$[g_-t_3g_-t_2]^+$
2.6, 2.5, 5.5 kJ/mol

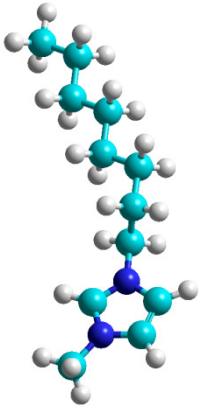

$[g_+tg_+t_4]^+$
2.9, 1.9, 3.5 kJ/mol

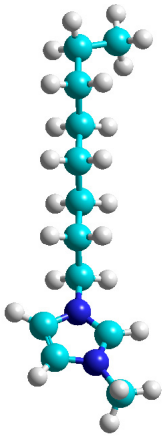

$[g_-t_5g_-]^+$
3.6, 2.8, 6.3 kJ/mol

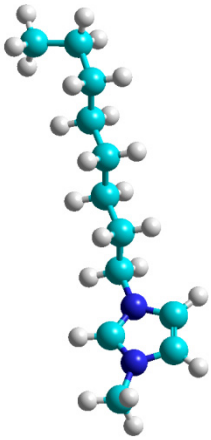

$[g_+t_5g_+]^+$
3.7, 2.8, 6.3 kJ/mol

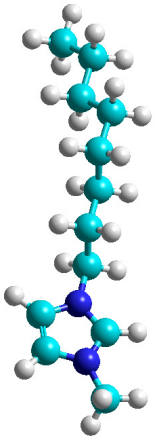

$[g_-t_3g_+t_2]^+$
3.8, 2.8, 5.5 kJ/mol

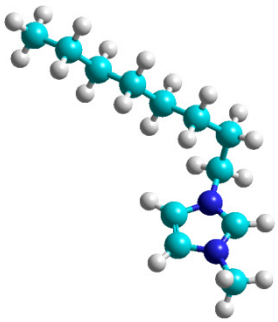

$[g_{-3}t_4]^+$
4.3, 2.0, 5.6 kJ/mol

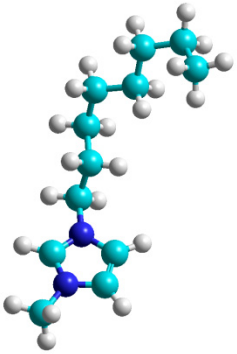

$[g_+t_2g_+t_2g_-]^+$
4.4, 2.7, 7.1 kJ/mol

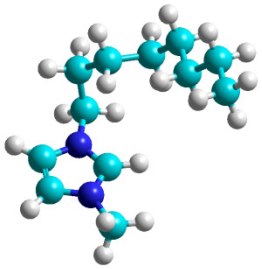

$[g_-g_{+2}tg_+t_2]^+$
8.7, 2.4, 8.6 kJ/mol

$[C_8mim]^+$

Figure S19.

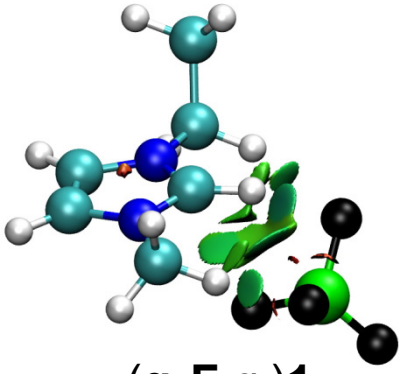

(**g**$_+$**F**;g$_-$)**1**
0.0, 0.0, 6.9 kJ/mol

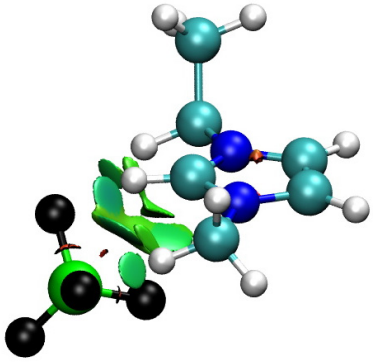

(**g**$_-$**F**;g$_+$)**1**
0.0, 0.1, 7.0 kJ/mol

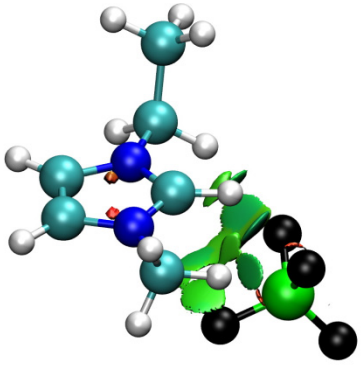

(**g**$_+$**F**;g$_-$)**2**
0.7, -,- kJ/mol

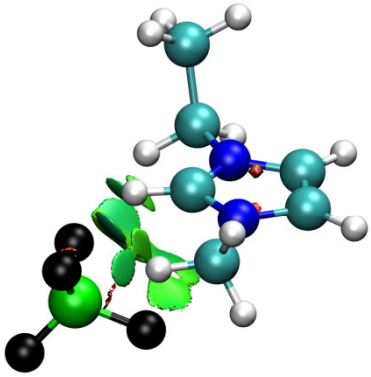

(**g**$_-$**F**;g$_+$)**2**
0.7, -, - kJ/mol

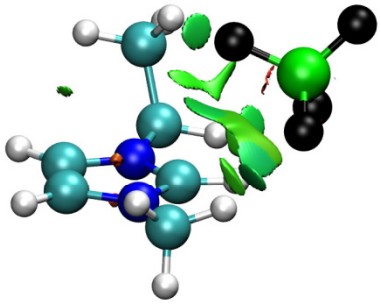

(**g**$_-$**F**;g$_-$)
2.6, 0.2, 0.0 kJ/mol

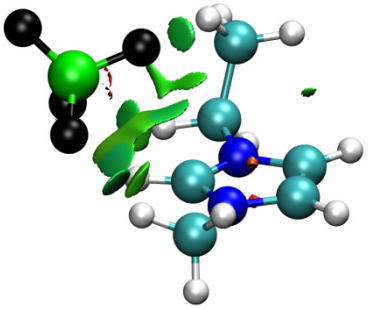

(**g**$_+$**F**;g$_+$)
2.6, 0.3, 0.0 kJ/mol

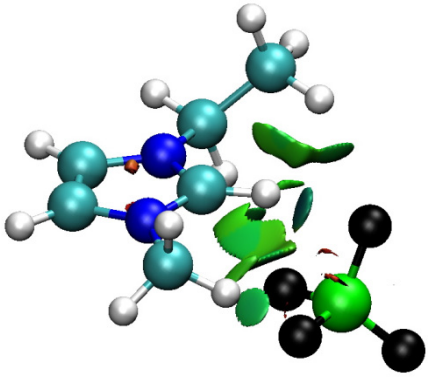

(**g**$_+$**F**;g$_-$)**3**
3.3, -, - kJ/mol

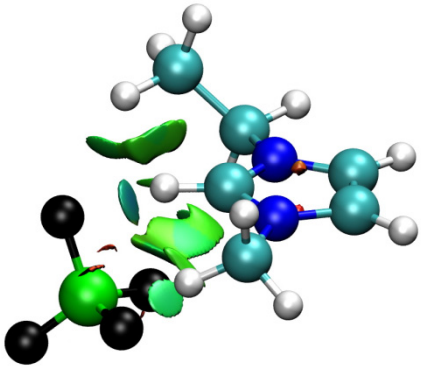

(**g**$_-$**F**;g$_+$)**3**
3.3, -, - kJ/mol

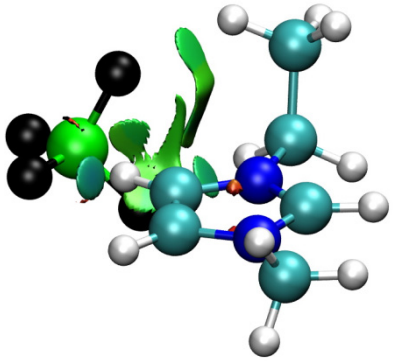

(**tB**$_a$;g$_-$)
30.8, -, - kJ/mol

(C_2mim:BF_4)

Figure S20.

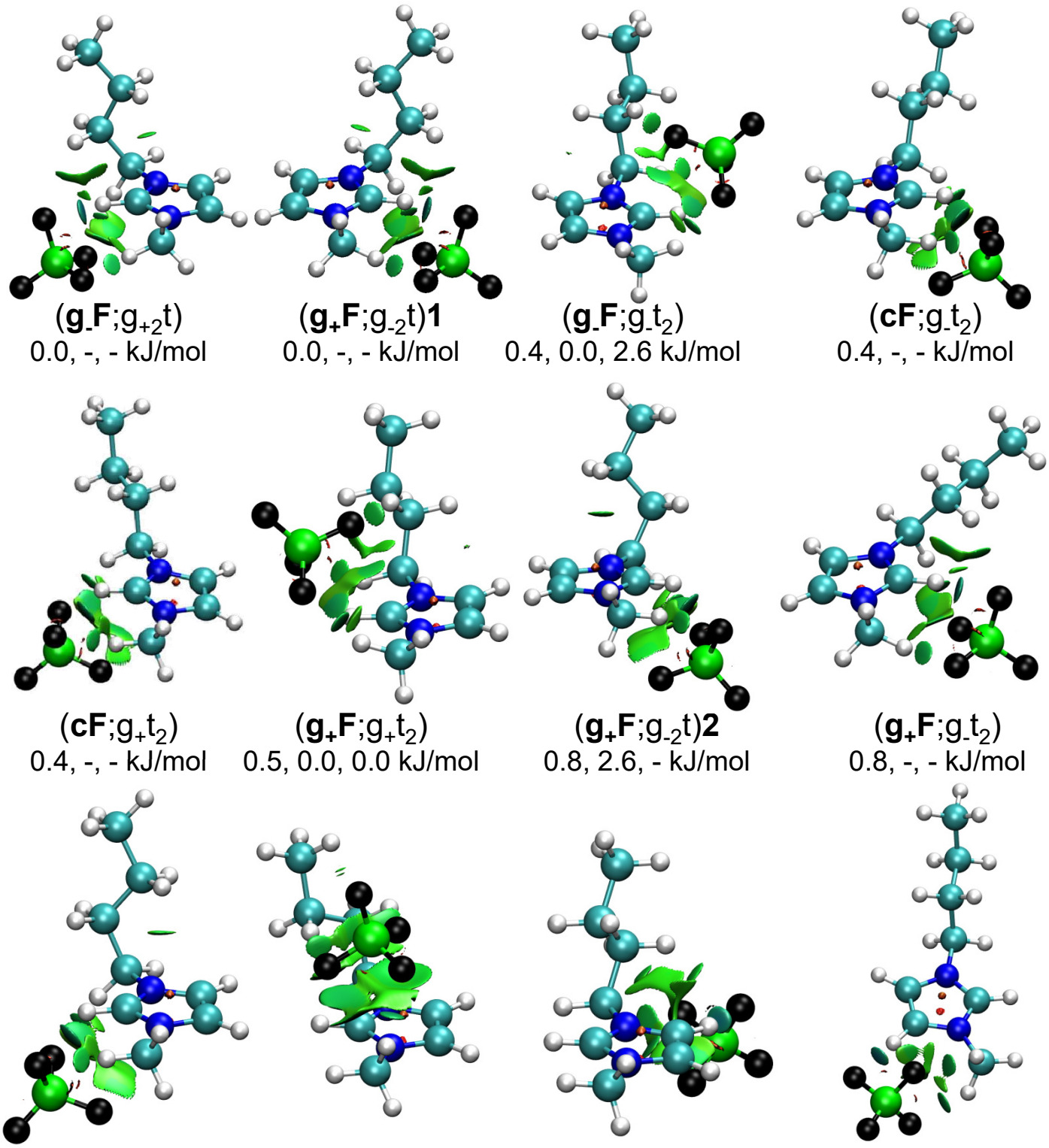

(C_4mim:BF_4)

Figure S21.

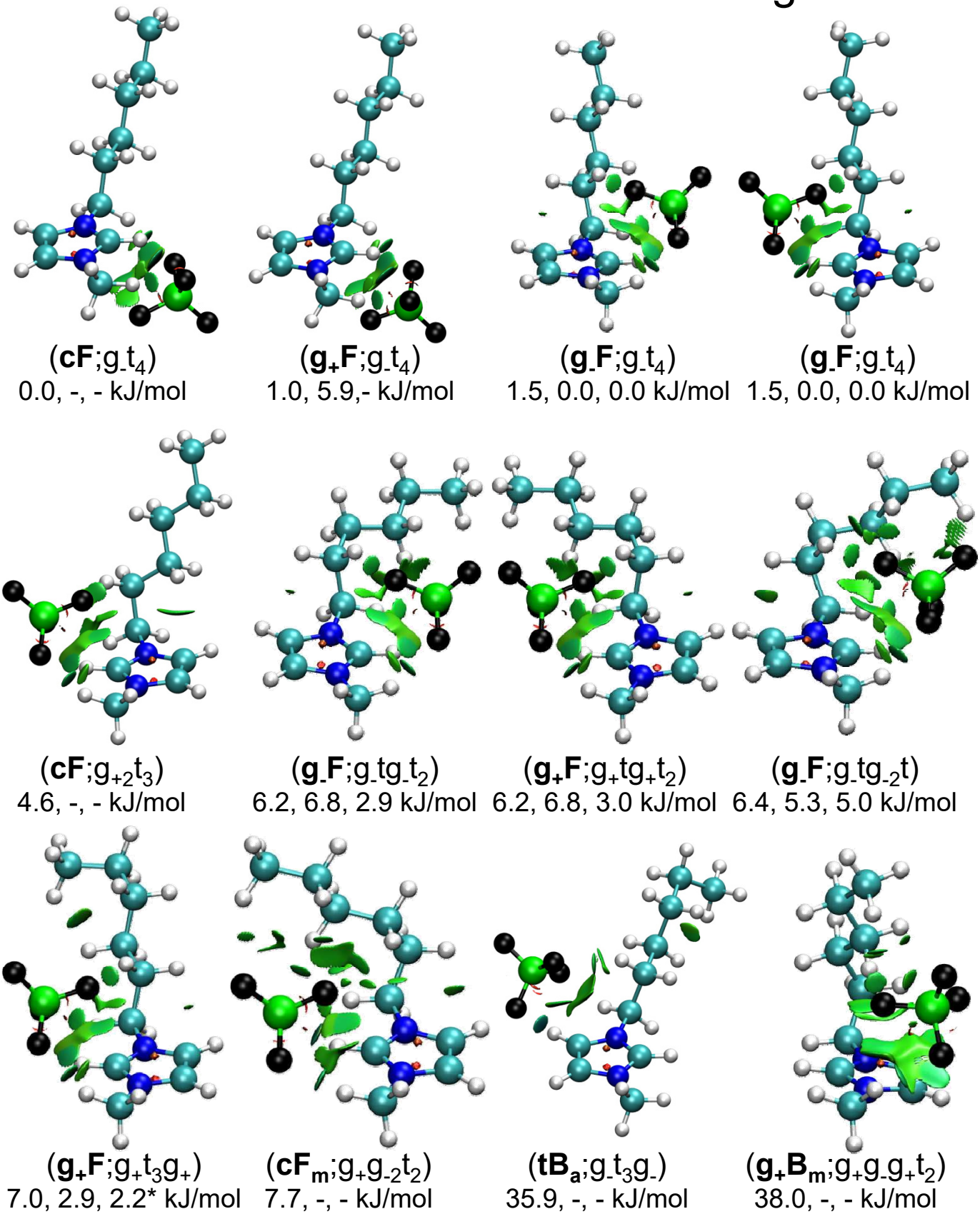

(C_6mim:BF_4)

Figure S22.

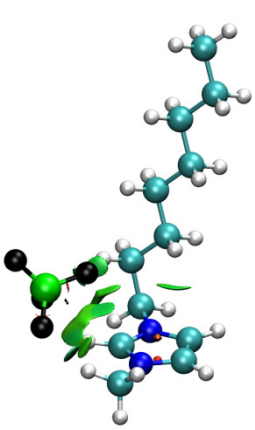

(**cF**;$g_{+2}t_5$)
0.0, -, - kJ/mol

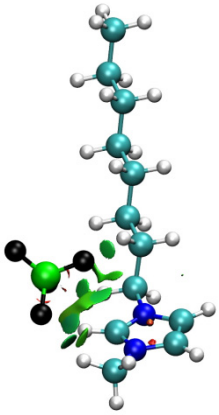

(**g$_+$F**;g_+t_6)
1.8, 1.5, 4.4 kJ/mol

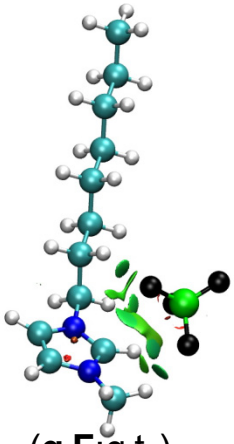

(**g$_-$F**;g_-t_6)
2.0, 1.5, 4.5 kJ/mol

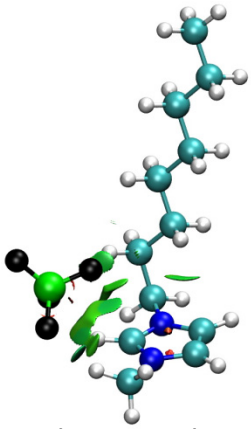

(**cF**;$g_{+2}t_5$)
4.3, -, - kJ/mol

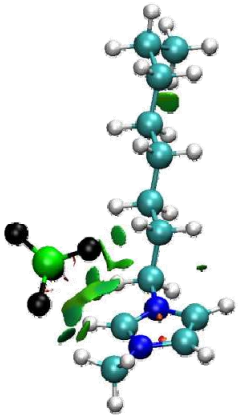

(**g$_+$F**;$g_+t_5g_-$)
5.2, 0.4, 0.9 kJ/mol

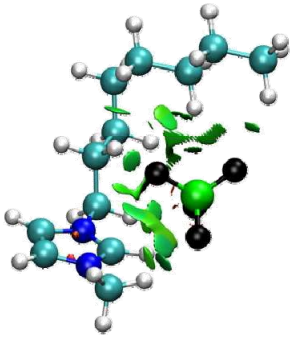

(**g$_-$F**;$g_-t_2g_{+2}t_2$)
5.2, 1.3, 0.0 kJ/mol

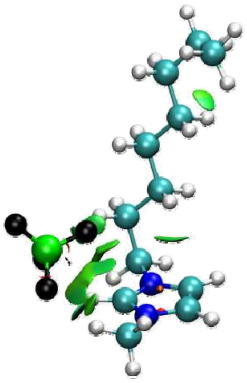

(**cF**;$g_{+2}t_4g_-$)
5.6, -, - kJ/mol

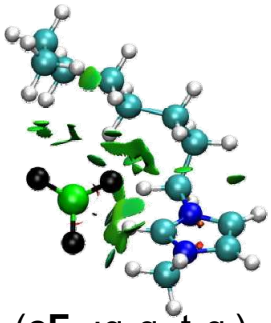

(**cF$_m$**;$g_+g_{-2}t_3g_-$)
6.6, -, - kJ/mol

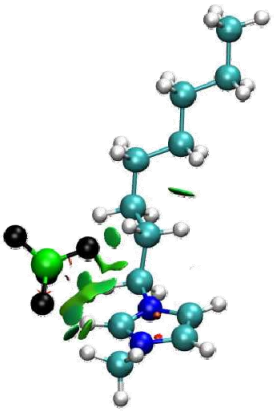

(**g$_+$F**;$g_+t_2g_+t_3$)
6.9, 4.0, 7.6 kJ/mol

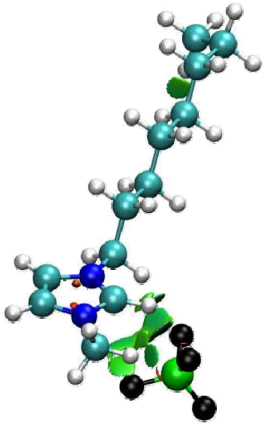

(**cF**;$g_-t_5g_+$)
6.9, -, - k/mol

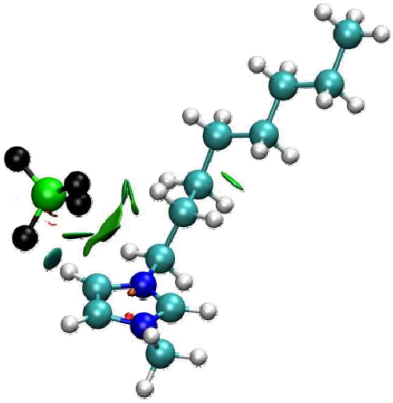

(**tB$_a$**;$g_-t_2g_+t_3$)
35.5, -, - kJ/mol

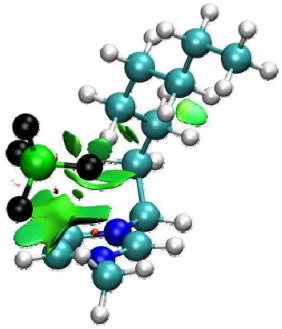

(**g$_-$B$_m$**;$g_-g_+g_-tg_-t_2$)
42.8, 26.8, 33.6 kJ/mol

(C_8mim:BF_4)

Figure S23.

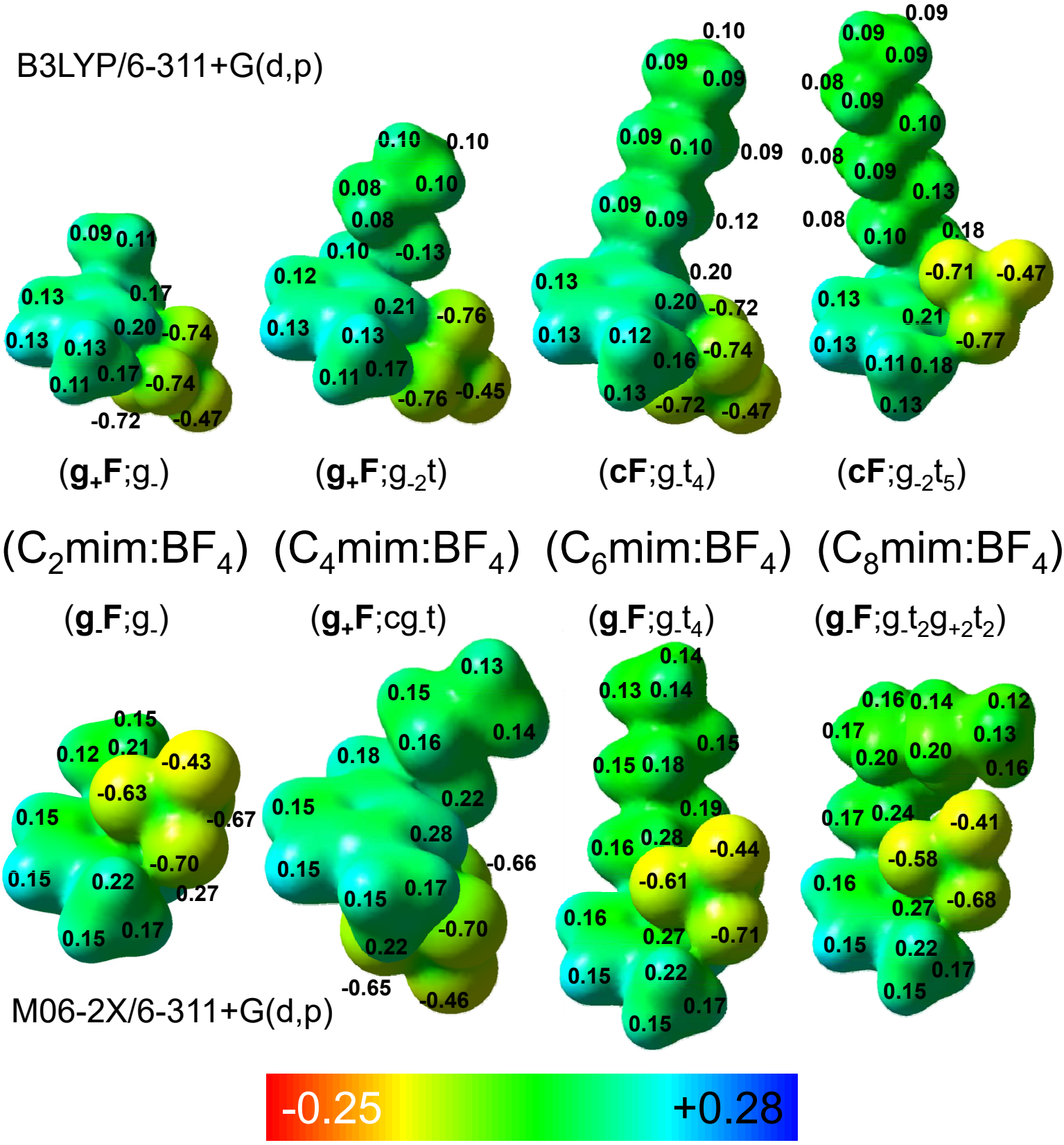
B3LYP/6-311+G(d,p)
(g+F;g-)
(g+F;g-2t)
(cF;g-t4)
(cF;g-2t5)
(C2mim:BF4)
(C4mim:BF4)
(C6mim:BF4)
(C8mim:BF4)
(g-F;g-)
(g+F;cg-t)
(g-F;g-t4)
(g-F;g-t2g+2t2)
M06-2X/6-311+G(d,p)
-0.25
+0.28

Figure S24.

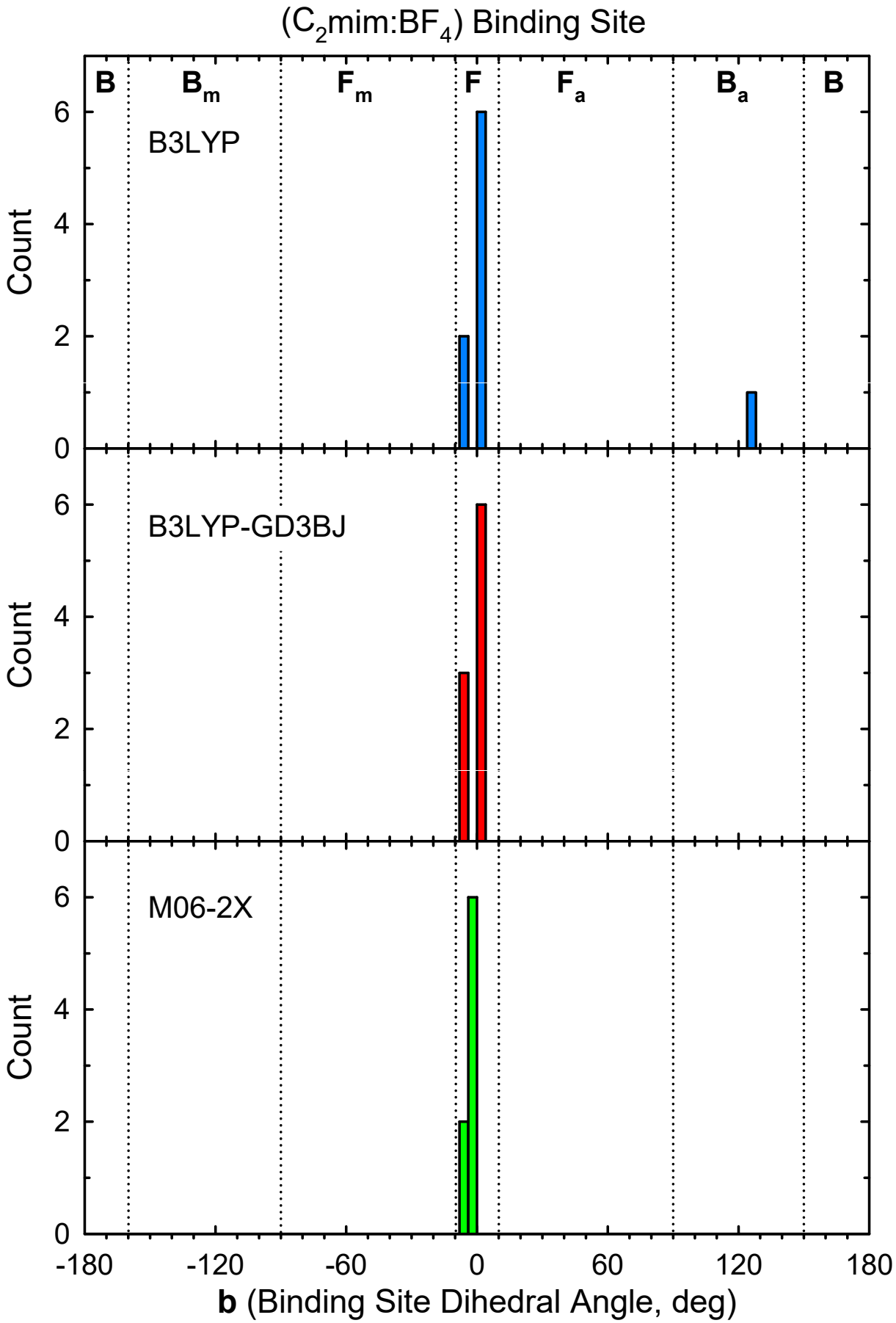
(C_2mim:BF_4) Binding Site
B
B_m
F_m
F
F_a
B_a
B
B3LYP
B3LYP-GD3BJ
M06-2X
Count
0
2
4
6
-180
-120
-60
0
60
120
180
b (Binding Site Dihedral Angle, deg)

Figure S25.

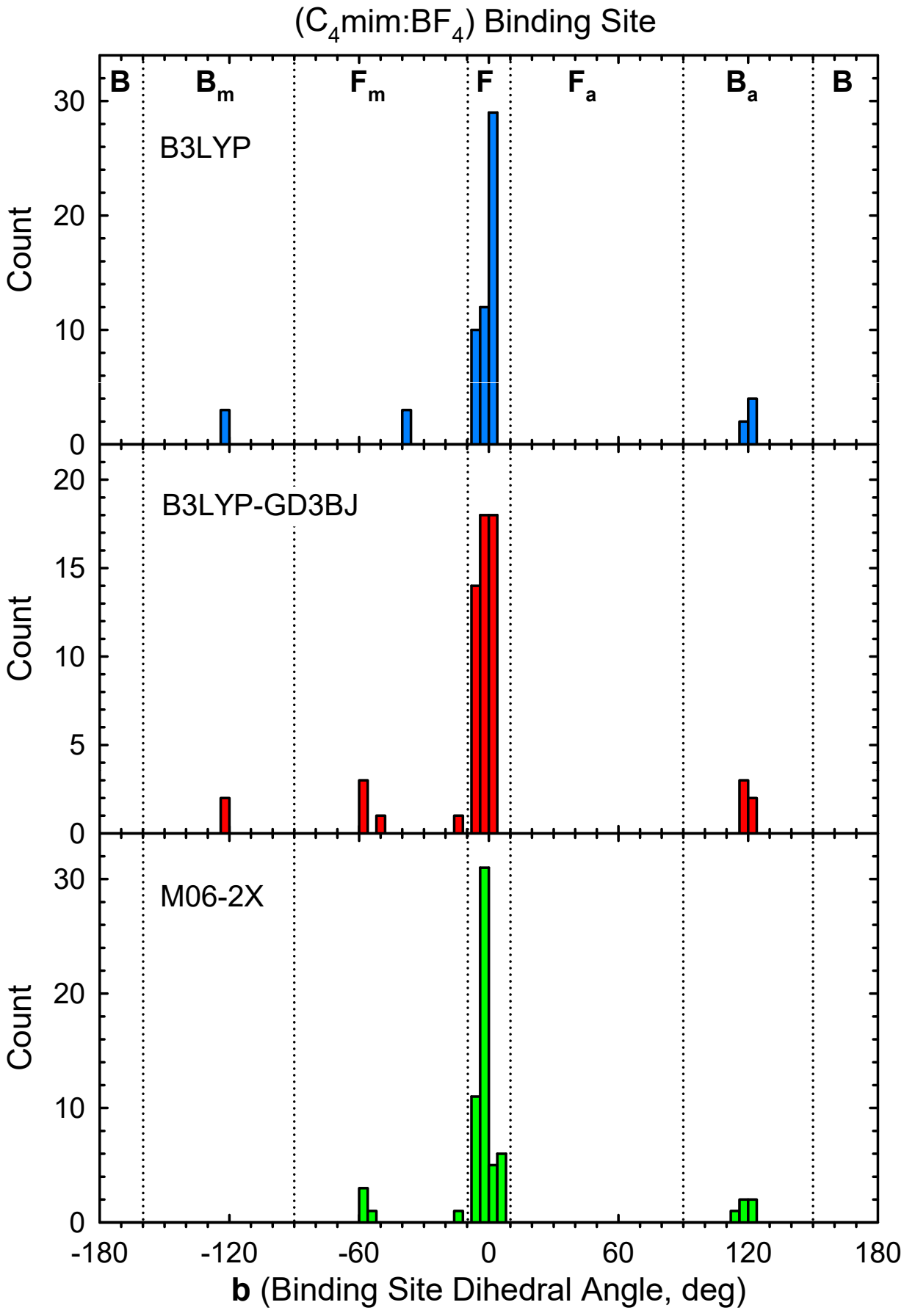
(C_4mim:BF_4) Binding Site
B
B_m
F_m
F
F_a
B_a
B
B3LYP
B3LYP-GD3BJ
M06-2X
Count
Count
Count
0
10
20
30
0
5
10
15
20
0
10
20
30
-180
-120
-60
0
60
120
180
b (Binding Site Dihedral Angle, deg)

Figure S26.

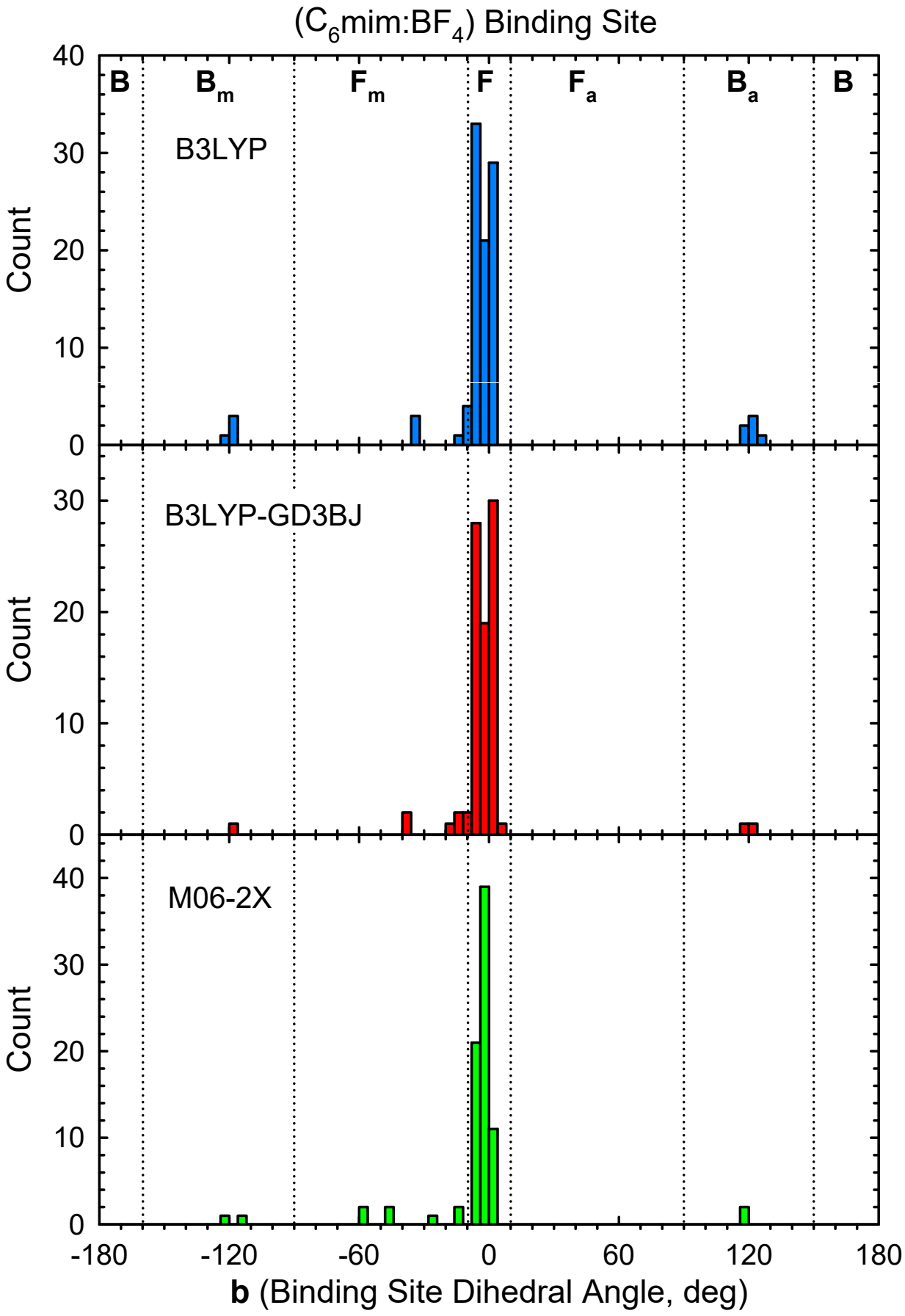
(C_6mim:BF_4) Binding Site
B
B_m
F_m
F
F_a
B_a
B
B3LYP
B3LYP-GD3BJ
M06-2X
Count
0
10
20
30
40
-180
-120
-60
0
60
120
180
b (Binding Site Dihedral Angle, deg)

Figure S27.

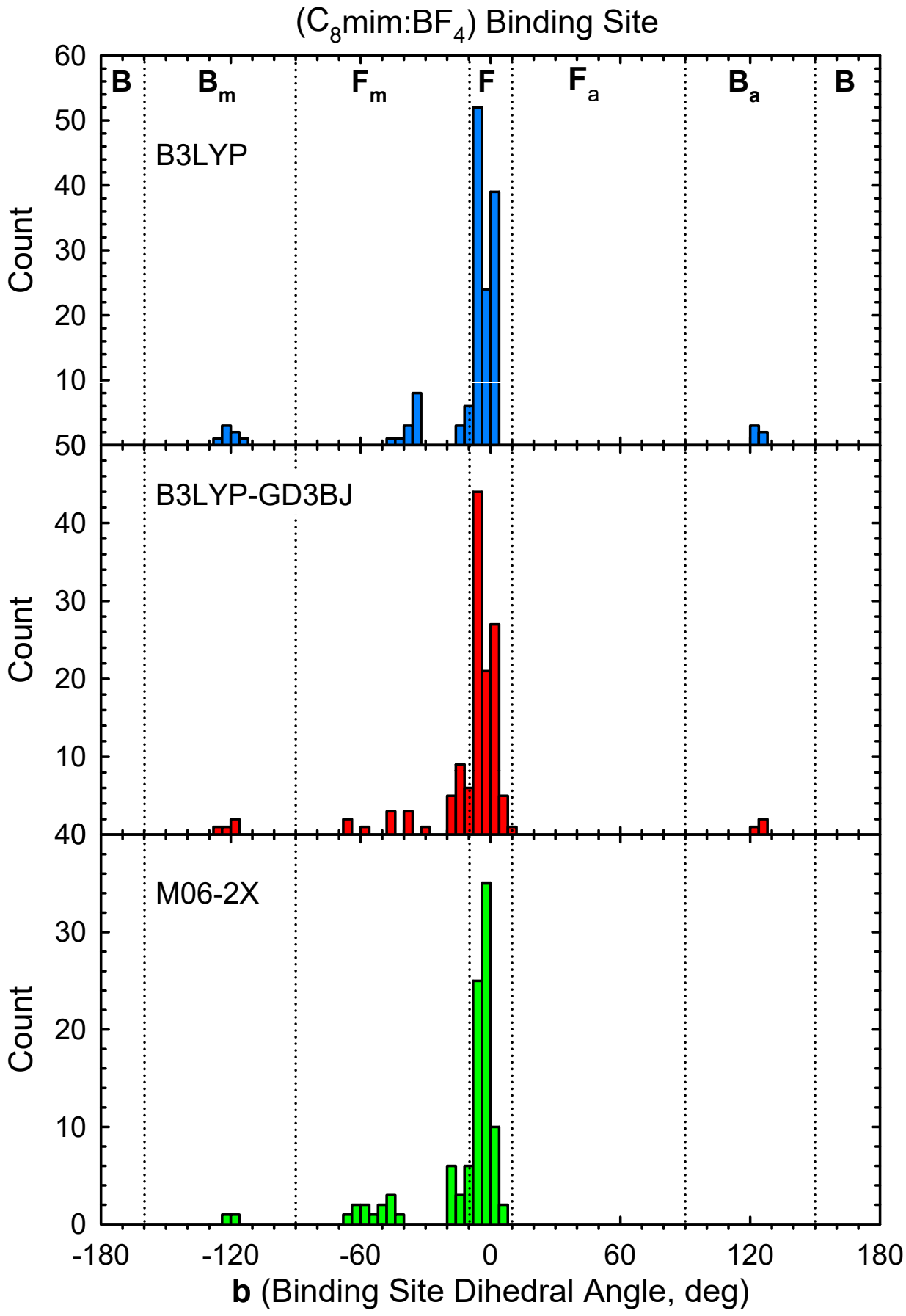
(C_8mim:BF_4) Binding Site
B
B_m
F_m
F
F_a
B_a
B
B3LYP
B3LYP-GD3BJ
M06-2X
Count
Count
Count
60
50
40
30
20
10
50
40
30
20
10
40
30
20
10
0
-180
-120
-60
0
60
120
180
b (Binding Site Dihedral Angle, deg)

Figure S28.

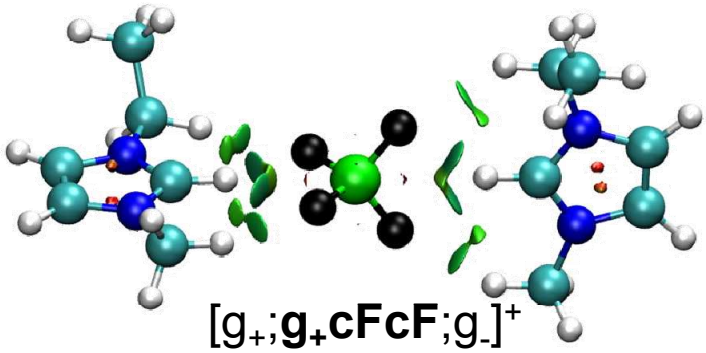

$[g_+;\mathbf{g_+cFcF};g_-]^+$
0.0, 0.0, - kJ/mol

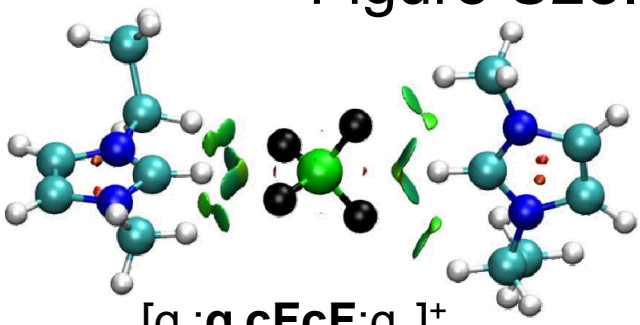

$[g_-;\mathbf{g_-cFcF};g_+]^+$
0.1, 1.9, - kJ/mol

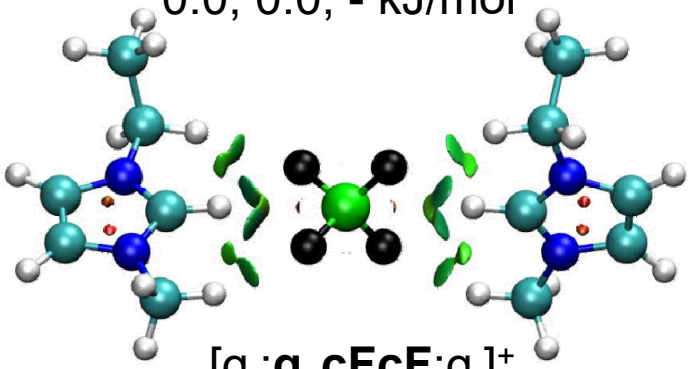

$[g_-;\mathbf{g_+cFcF};g_-]^+$
1.8, 0.5, - kJ/mol

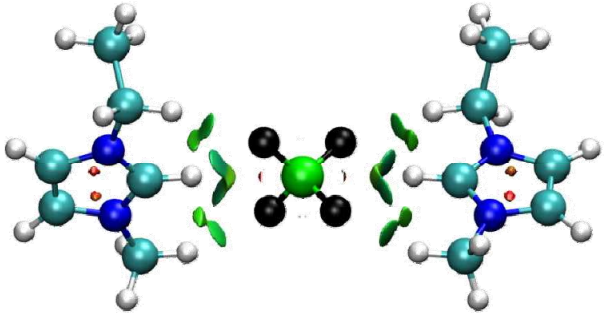

$[g_+;\mathbf{g_-cFcF};g_+]^+$
1.9, 0.5, - kJ/mol

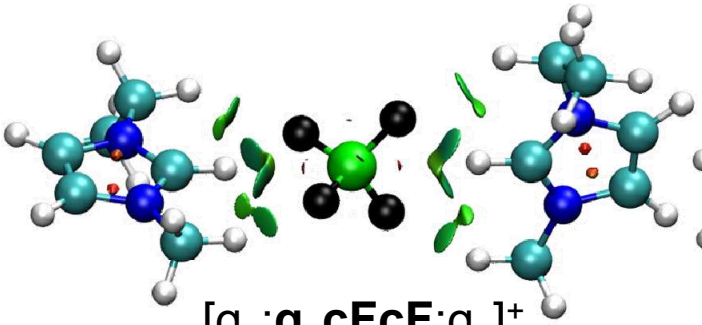

$[g_+;\mathbf{g_+cFcF};g_+]^+$
2.1, 1.6, - kJ/mol

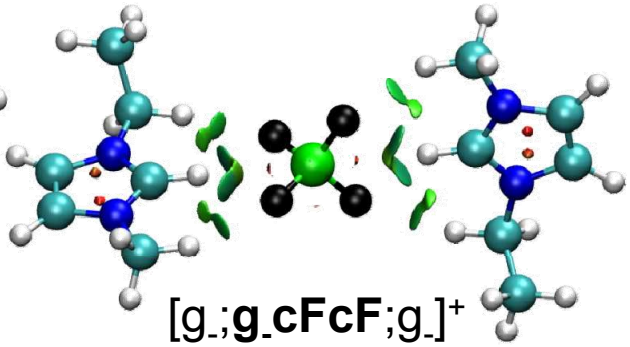

$[g_-;\mathbf{g_-cFcF};g_-]^+$
2.1, 1.6, - kJ/mol

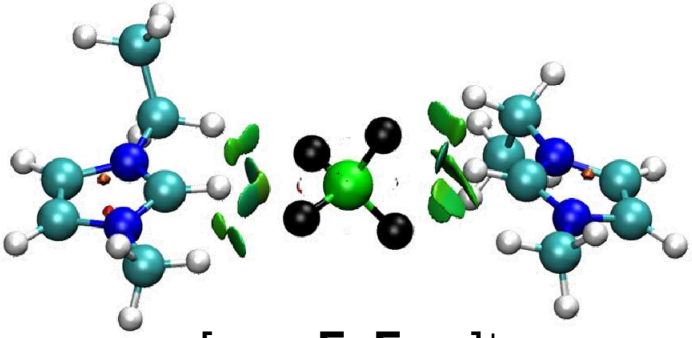

$[g_-;\mathbf{ccFcF_a};g_-]^+$
6.8, -, - kJ/mol

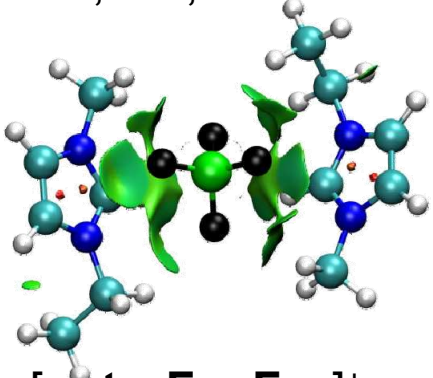

$[g_+;\mathbf{tg_+Fg_+F};g_-]^+$
-, -, 0.0 kJ/mol

$[2C_2mim{:}BF_4]^+$

Figure S28.

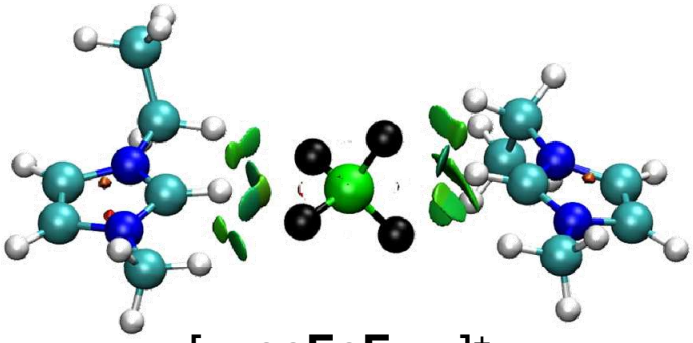

$[g_-;\mathbf{ccFcF_a};g_-]^+$
6.8, -, - kJ/mol

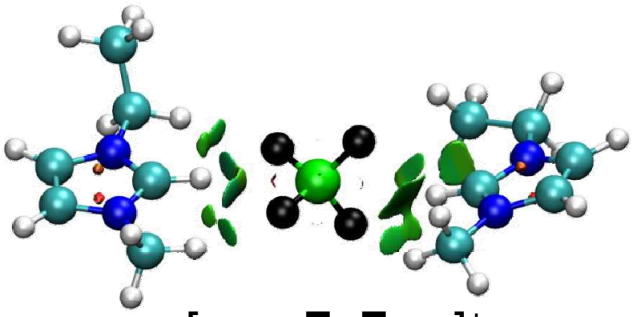

$[g_-;\mathbf{ccFcF_m};c]^+$
7.6, 5.7, 3.9 kJ/mol

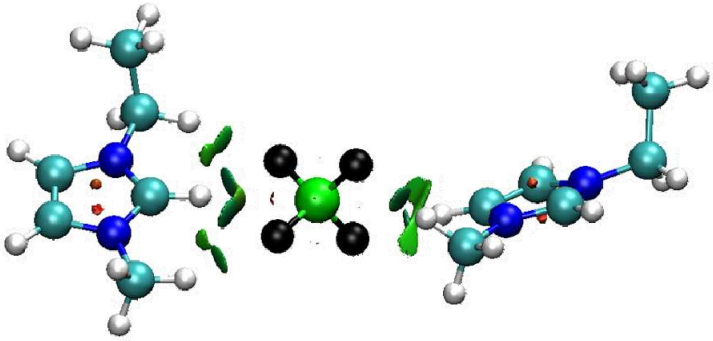

$[g_-;\mathbf{ccFg_-B_m};g_-]^+$
18.4, 20.6, - kJ/mol

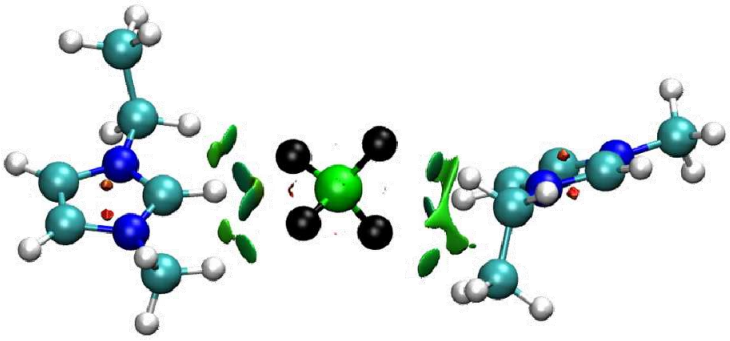

$[g_-;\mathbf{tcFtB_a};g_-]^+$
18.9, 17.5,14.0 kJ/mol

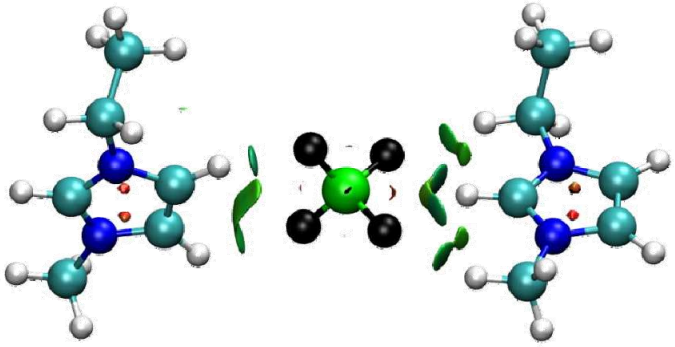

$[g_-;\mathbf{g_-tBcF};g_+]^+$
23.8, 23.3, 22.9 kJ/mol

$[2C_2mim{:}BF_4]^+$

Figure S29.

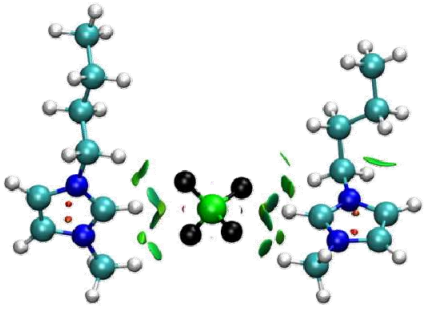

$[g_{+2}t;\mathbf{g_{-}cFcF};g_{+}t_2]^{+}$
0.0, -, - kJ/mol

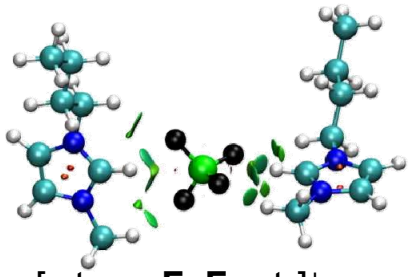

$[g_{-}t_2;\mathbf{g_{-}cFcF};g_{+}t_2]^{+}$
0.5, 0.4, - kJ/mol

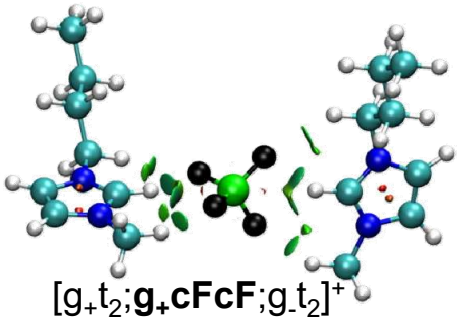

$[g_{+}t_2;\mathbf{g_{+}cFcF};g_{-}t_2]^{+}$
0.5, 1.5, - kJ/mol

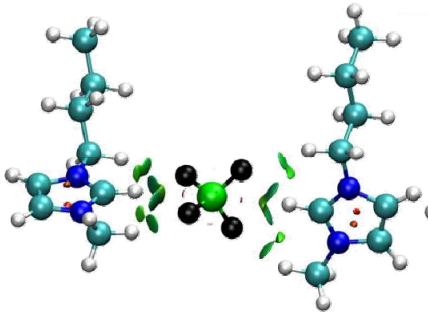

$[g_{-}t_2;\mathbf{g_{+}cFcF};g_{-}t_2]^{+}$
0.7, -, 11.1 kJ/mol

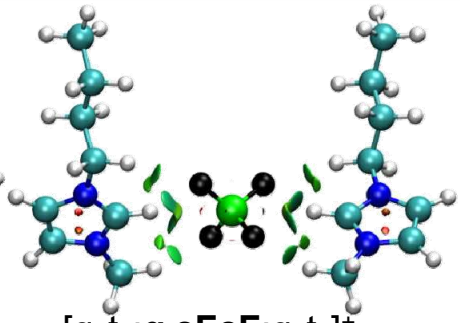

$[g_{+}t_2;\mathbf{g_{-}cFcF};g_{+}t_2]^{+}$
0.8, -, - kJ/mol

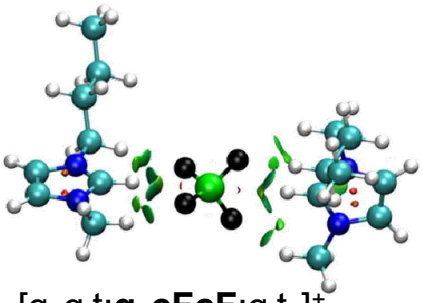

$[g_{+}g_{-}t;\mathbf{g_{+}cFcF};g_{-}t_2]^{+}$
1.4, 0.9, - kJ/mol

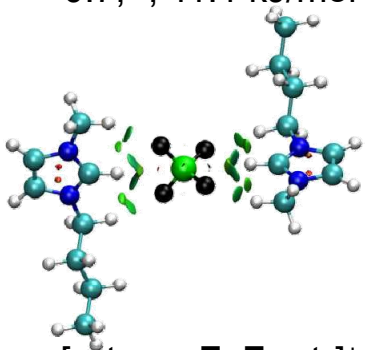

$[g_{+}t_2;\mathbf{g_{+}cFcF};g_{+}t_2]^{+}$
1.7, 3.2, - kJ/mol

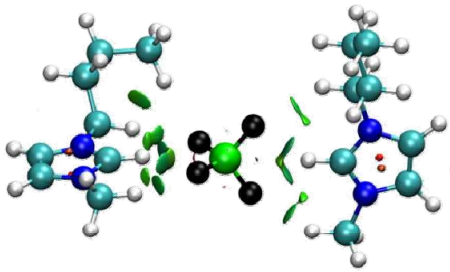

$[g_{-}tg_{-};\mathbf{g_{+}cFcF};g_{+}t_2]^{+}$
1.8, -, - kJ/mol

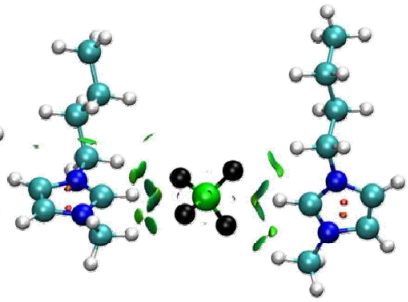

$[g_{-}t_2;\mathbf{g_{+}cFcF};g_{-}g_{+}t]^{+}$
2.2, -, - kJ/mol

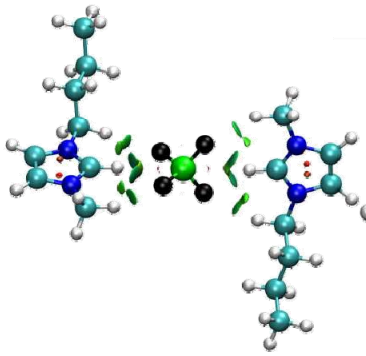

$[g_{-}t_2;\mathbf{g_{-}cFcF};g_{-}t_2]^{+}$
3.0, 3.2, 0.0 kJ/mol

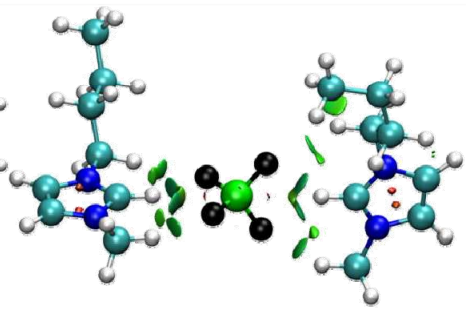

$[g_{+}tg_{+};\mathbf{g_{+}cFcF};g_{-}t_2]^{+}$
3.2, -, - kJ/mol

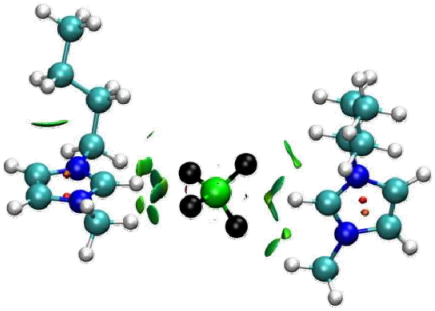

$[g_{+}t_2;\mathbf{g_{+}cFcF};g_{-2}t]^{+}$
3.3, 5.2, - kJ/mol

$[2C_4mim{:}BF_4]^{+}$

Figure S29.

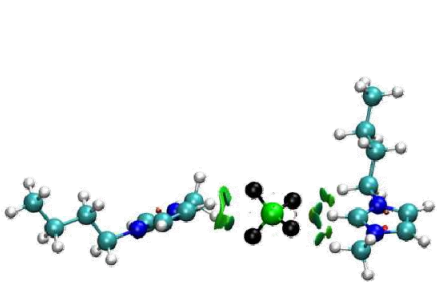

$[g_{-}t_2;\mathbf{tg_{+}B_mcF};g_{+}t_2]^{+}$
16.9, -, - kJ/mol

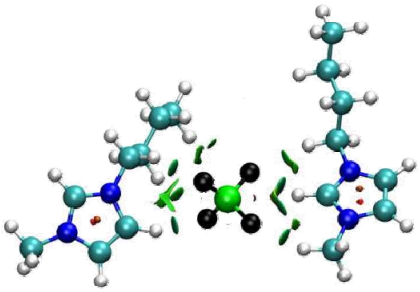

$[g_{-}t_2;\mathbf{ctB_acF};g_{+}t_2]^{+}$
18.1, 20.3, - kJ/mol

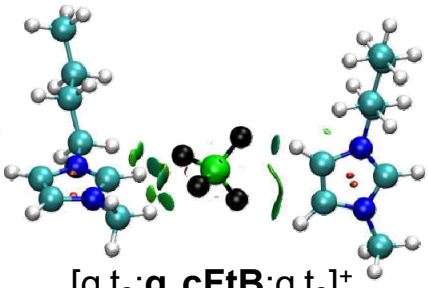

$[g_{-}t_2;\mathbf{g_{+}cFtB};g_{-}t_2]^{+}$
19.4, 25.4, - kJ/mol

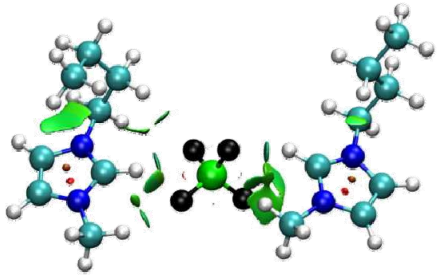

$[g_{+}g_{-}t;\mathbf{ccF_mcF};g_{-2}g_{+}]^{+}$
23.3, 18.2, 17.4 kJ/mol

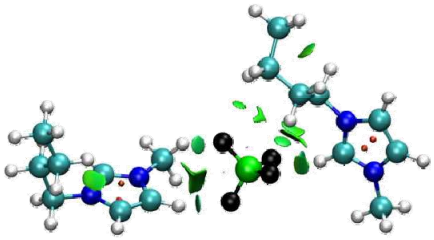

$[g_{+}tg_{-};\mathbf{g_{-}cF_ag_{-}B_m};g_{-2}t]^{+}$
32.9, -, - kJ/mol

$[2C_4mim{:}BF_4]^{+}$

Figure S30.

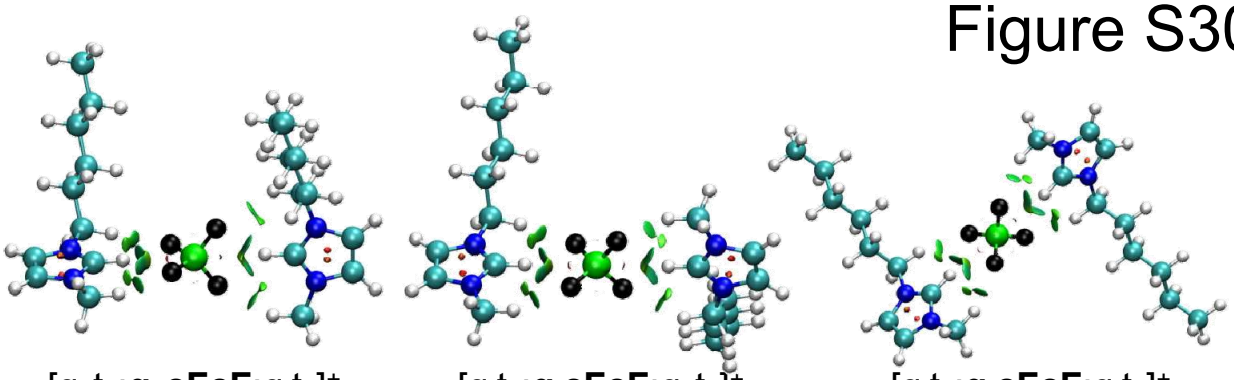

$[g_+t_4;\mathbf{g_+cFcF};g_-t_4]^+$
0.0, -, - kJ/mol

$[g_-t_4;\mathbf{g_-cFcF};g_+t_4]^+$
0.0, -, - kJ/mol

$[g_-t_4;\mathbf{g_-cFcF};g_-t_4]^+$
0.5, 3.5, - kJ/mol

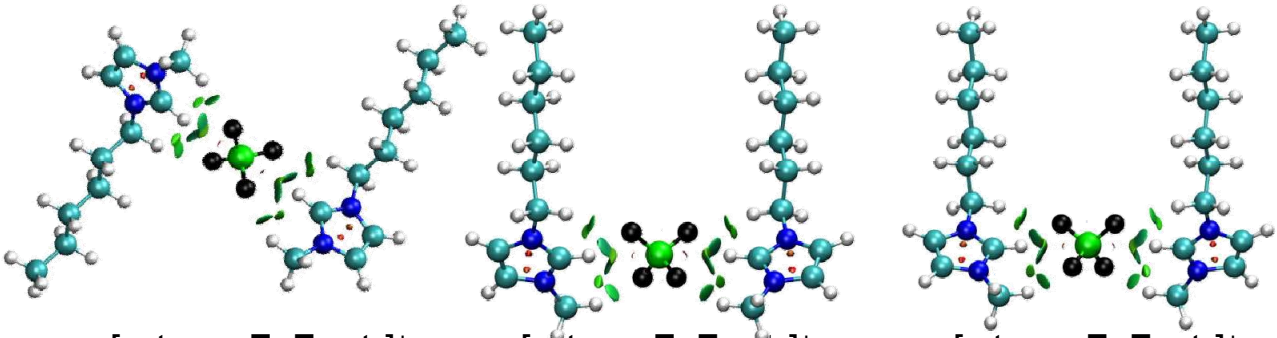

$[g_+t_4;\mathbf{g_+cFcF};g_+t_4]^+$
0.5, 3.5, - kJ/mol

$[g_+t_4;\mathbf{g_-cFcF};g_+t_4]^+$
1.0, 4.8, 7.8* kJ/mol

$[g_-t_4;\mathbf{g_+cFcF};g_-t_4]^+$
1.1, -, - kJ/mol

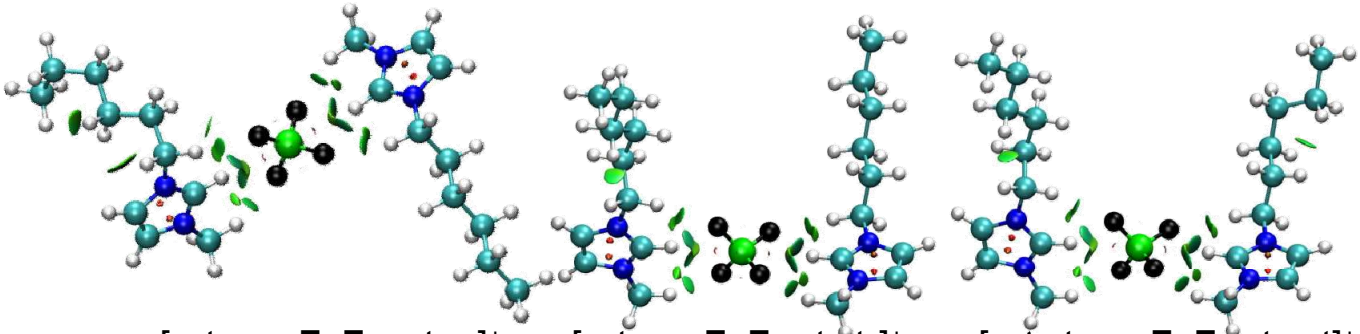

$[g_+t_4;\mathbf{g_+cFcF};g_{+2}t_2g_-]^+$
5.1, -, - kJ/mol

$[g_+t_4;\mathbf{g_-cFcF};g_+tg_-t_2]^+$
5.3, -, 5.1 kJ/mol

$[g_+tg_-t_2;\mathbf{g_-cFcF};g_+t_2g_+t]^+$
8.0, 6.3, - kJ/mol

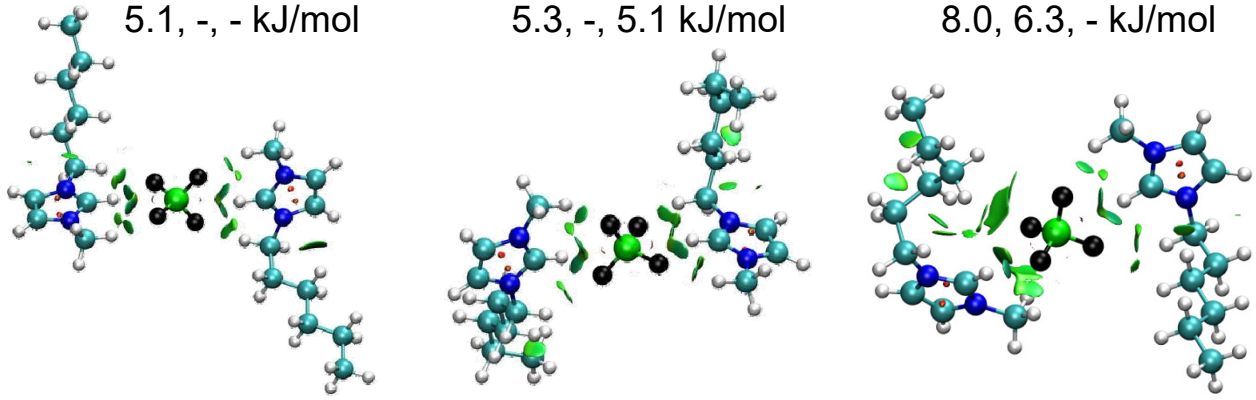

$[g_{-2}t_3;\mathbf{g_-cFcF};g_-g_+t_3]^+$
8.8, 1.6, 1.1 kJ/mol

$[g_+g_-t_2g_+;\mathbf{g_+cFcF};g_-t_3g_-]^+$
11.5, -, - kJ/mol

$[g_+g_{-4};\mathbf{tcF_mcF};g_-g_+t_3]^+$
22.3, -, 0.0 kJ/mol

$[2C_6mim{:}BF_4]^+$

Figure S30.

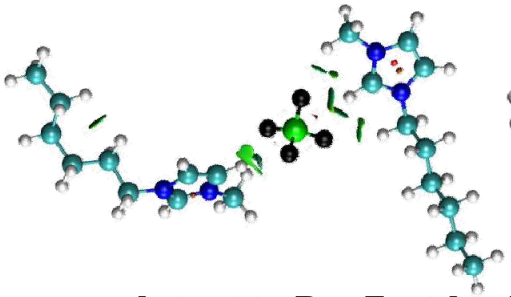

$[g_-t_2g_-t;\mathbf{tg_-B_mcF};g_-t_4]^+$
15.7, -. - kJ/mol

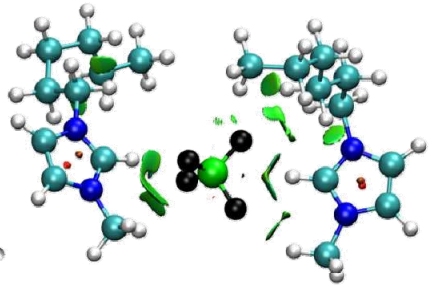

$[g_+tg_{+2}t;\mathbf{ccF_mcF};g_+g_-t_2g_-]^+$
16.3, -, 7.1 kJ/mol

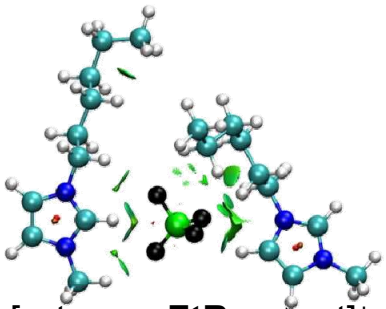

$[g_+t_3g_+;\mathbf{ccFtB_a};g_-t_2g_-t]^+$
26.6, -, - kJ/mol

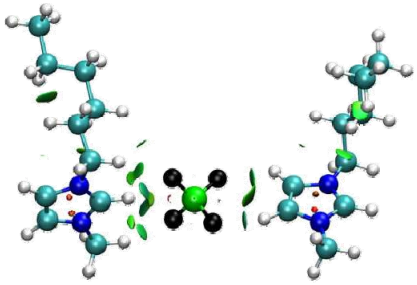

$[g_-g_+t_2g_-;\mathbf{g_-tBcF};g_+g_-tg_-t]^+$
33.4, 29.7, 20.0 kJ/mol

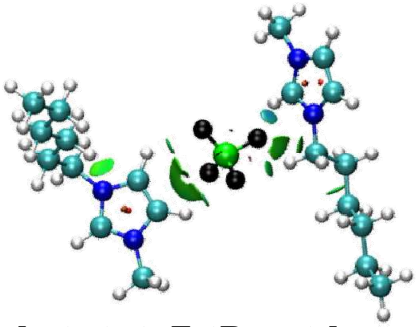

$[g_+tg_-t_2;\mathbf{tcF_atB};g_{+2}t_3]^+$
39.7, -, - kJ/mol

$[2C_6mim{:}BF_4]^+$

Figure S31.

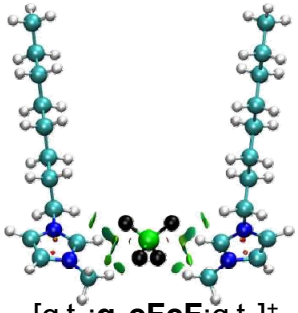

$[g_{-}t_6;\mathbf{g_{+}cFcF};g_{-}t_6]^{+}$
0.0, 0.0, - kJ/mol

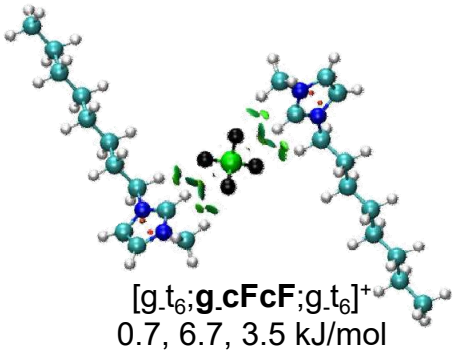

$[g_{-}t_6;\mathbf{g_{-}cFcF};g_{-}t_6]^{+}$
0.7, 6.7, 3.5 kJ/mol

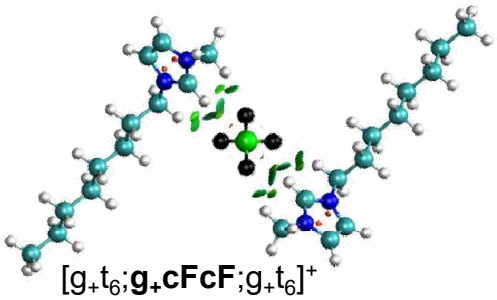

$[g_{+}t_6;\mathbf{g_{+}cFcF};g_{+}t_6]^{+}$
0.8, 5.5, 1.1 kJ/mol

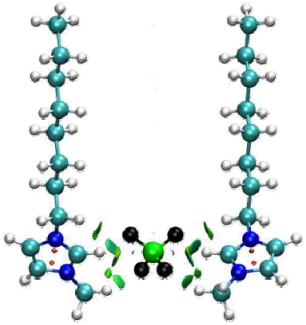

$[g_{+}t_6;\mathbf{g_{-}cFcF};g_{+}t_6]^{+}$
2.1, 0.0, 3.0 kJ/mol

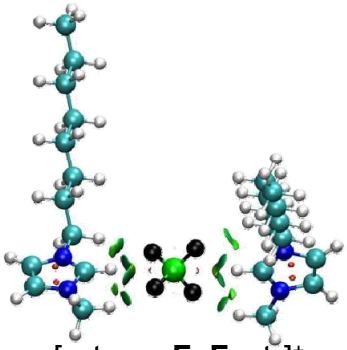

$[g_{+}t_6;\mathbf{g_{+}cFcF};g_{-}t_6]^{+}$
7.0, -, - kJ/mol

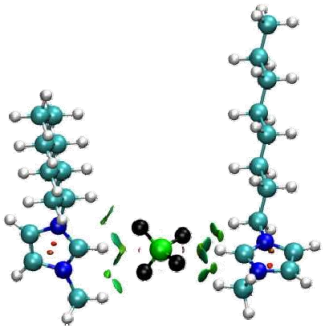

$[g_{-}t_6;\mathbf{g_{-}cFcF};g_{+}t_6]^{+}$
7.2, 3.6, - kJ/mol

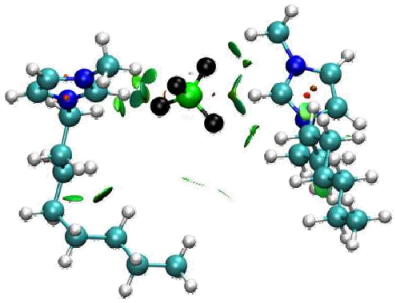

$[g_{+}t_2g_{-2}t_2;\mathbf{g_{-}cFcF};g_{-}g_{+}tg_{-}t_3]^{+}$
13.4, -, - kJ/mol

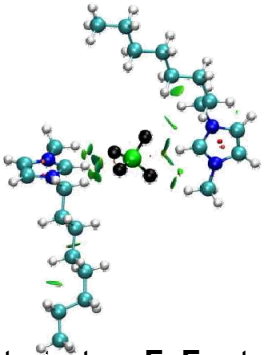

$[g_{-}t_2tg_{+}tg_{+}t;\mathbf{g_{-}cFcF};g_{+}tg_{+}t_4]^{+}$
16.1, 11.7,- kJ/mol

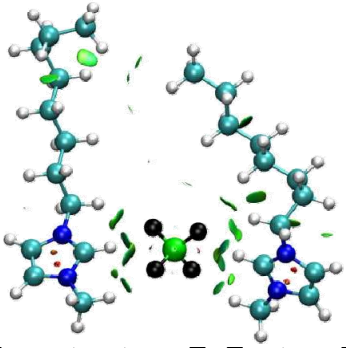

$[g_{-}g_{+2}t_2g_{+}t;\mathbf{g_{+}cFcF};g_{-}t_4g_{+2}]^{+}$
19.2, 2.2, 5.7 kJ/mol

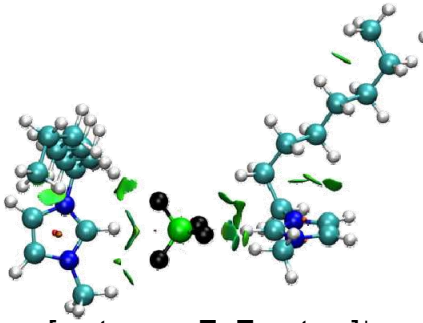

$[g_{+3}t_3g_{-};\mathbf{g_{-}cFcF};g_{-2}t_4g_{+}]^{+}$
19.4, -, 1.6 kJ/mol

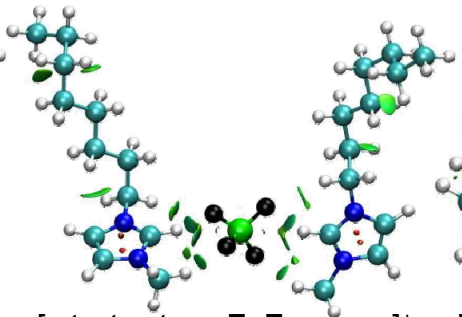

$[g_{-}tg_{+}t_2g\text{-}t;\mathbf{g_{+}cFcF};g_{-2}t_3g_{+2}]^{+}$
19.4, 13.6, - kJ/mol

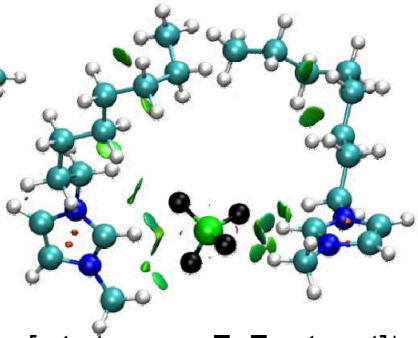

$[g_{-}tg_{-}t_2g_{+2};\mathbf{g_{-}cFcF};g_{+}t_3g_{+2}t]^{+}$
19.4, -, - kJ/mol

$[2C_8mim{:}BF_4]^{+}$

Figure S31.

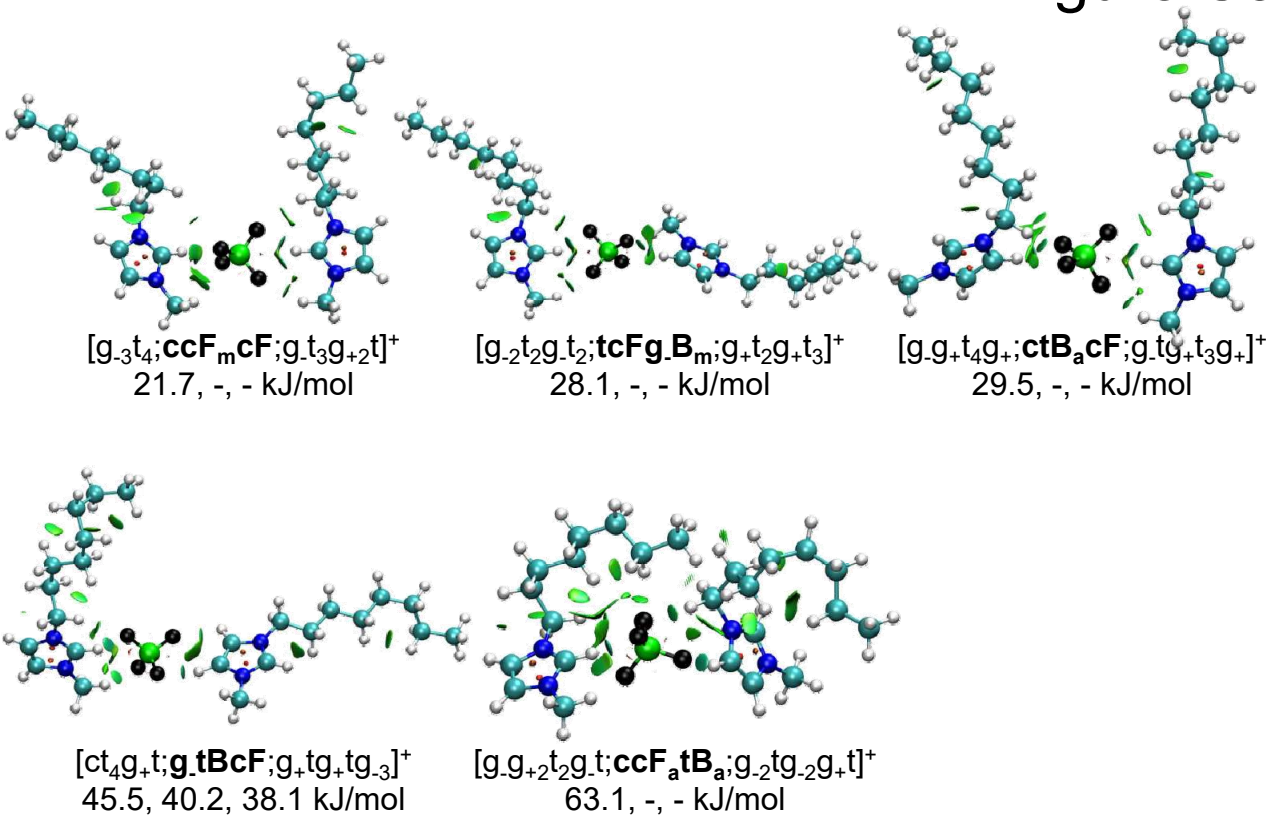

$[g_{-3}t_4;\mathbf{ccF_mcF};g_{-}t_3g_{+2}t]^+$
21.7, -, - kJ/mol

$[g_{-2}t_2g_{-}t_2;\mathbf{tcFg_{-}B_m};g_{+}t_2g_{+}t_3]^+$
28.1, -, - kJ/mol

$[g_{-}g_{+}t_4g_{+};\mathbf{ctB_acF};g_{-}tg_{+}t_3g_{+}]^+$
29.5, -, - kJ/mol

$[ct_4g_{+}t;\mathbf{g_{-}tBcF};g_{+}tg_{+}tg_{-3}]^+$
45.5, 40.2, 38.1 kJ/mol

$[g_{-}g_{+2}t_2g_{-}t;\mathbf{ccF_atB_a};g_{-2}tg_{-2}g_{+}t]^+$
63.1, -, - kJ/mol

$[2C_8mim{:}BF_4]^+$

Figure S32.

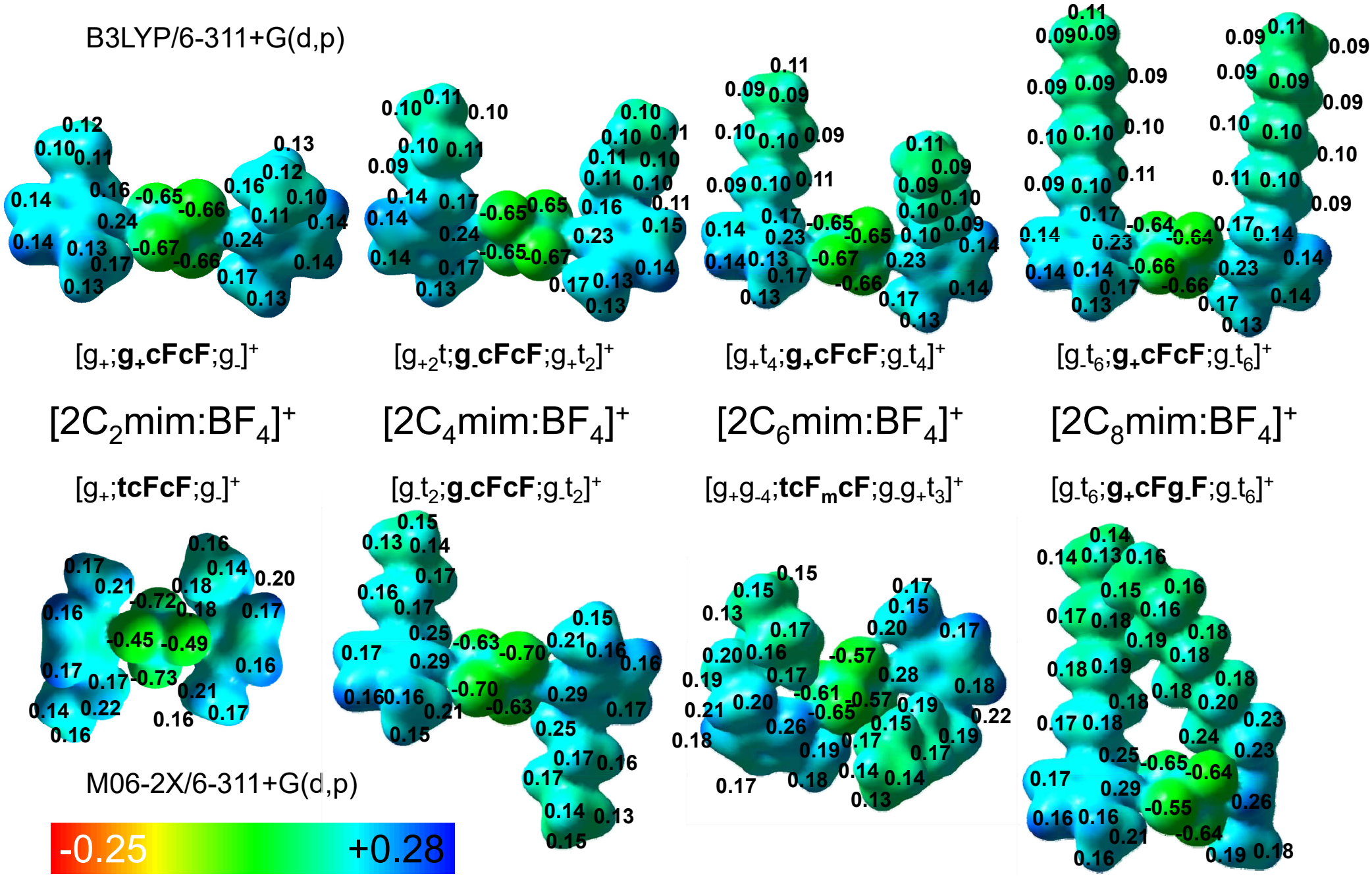
B3LYP/6-311+G(d,p)
[g+;g+cFcF;g-]+
[g+2t;g-cFcF;g+t2]+
[g+t4;g+cFcF;g-t4]+
[g-t6;g+cFcF;g-t6]+
[2C2mim:BF4]+
[2C4mim:BF4]+
[2C6mim:BF4]+
[2C8mim:BF4]+
[g+;tcFcF;g-]+
[g-t2;g-cFcF;g-t2]+
[g+g-4;tcFmcF;g-g+t3]+
[g-t6;g+cFg-F;g-t6]+
M06-2X/6-311+G(d,p)
-0.25
+0.28

Figure S33.

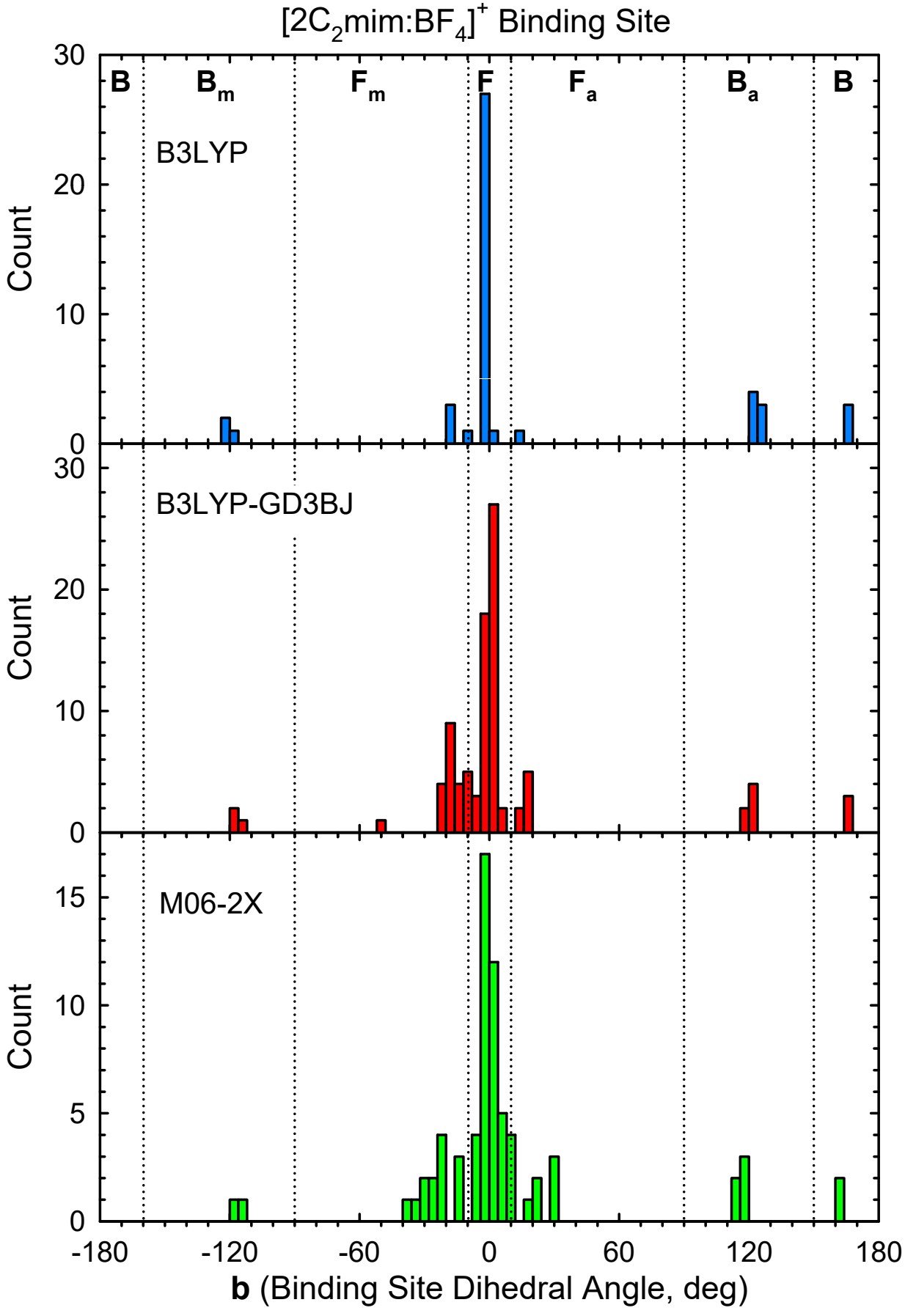
[2C2mim:BF4]+ Binding Site
B
Bm
Fm
F
Fa
Ba
B
B3LYP
B3LYP-GD3BJ
M06-2X
Count
b (Binding Site Dihedral Angle, deg)
-180
-120
-60
0
60
120
180

Figure S34.

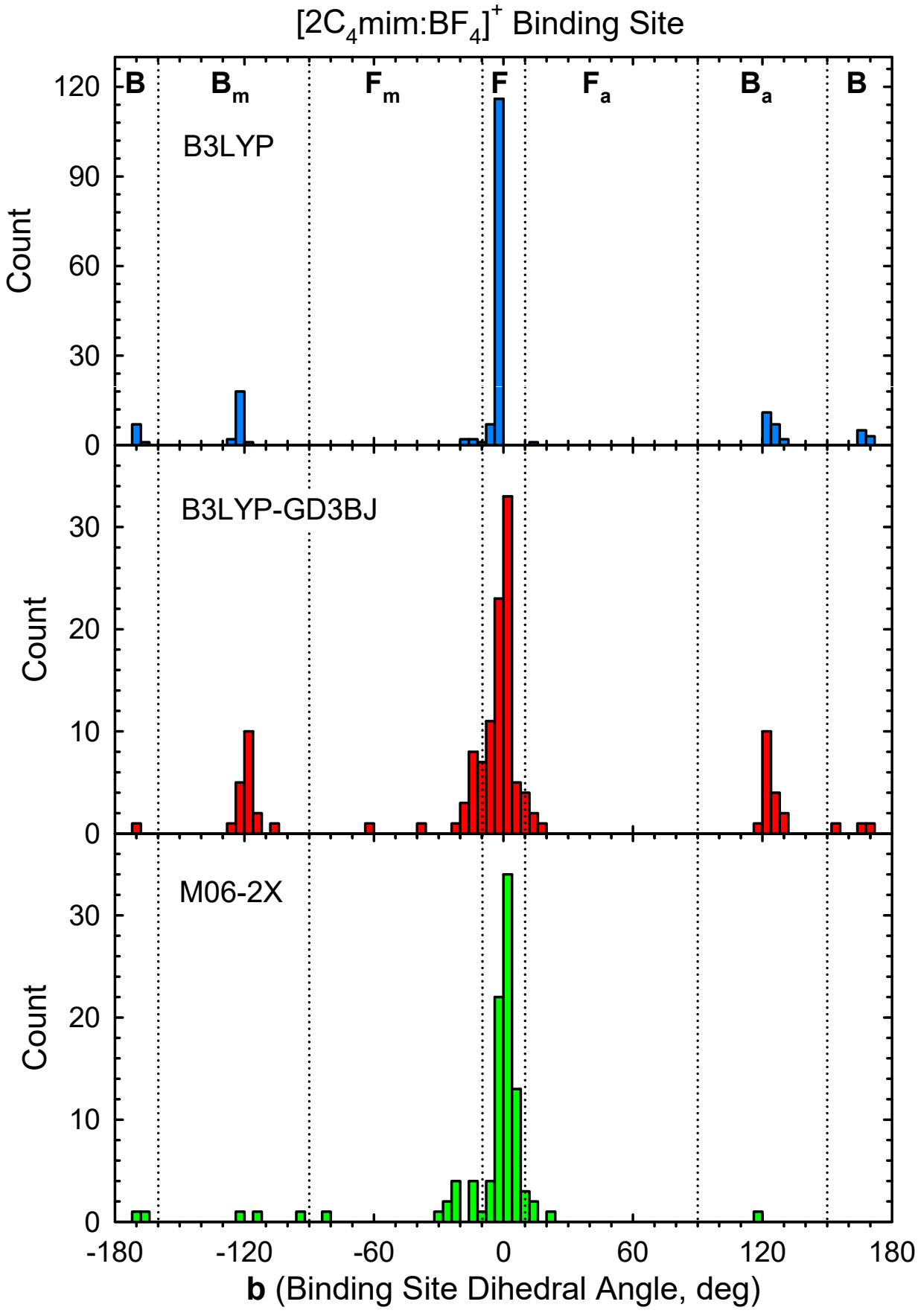
[2C4mim:BF4]+ Binding Site
B
Bm
Fm
F
Fa
Ba
B
B3LYP
B3LYP-GD3BJ
M06-2X
Count
b (Binding Site Dihedral Angle, deg)
-180
-120
-60
0
60
120
180

Figure S35.

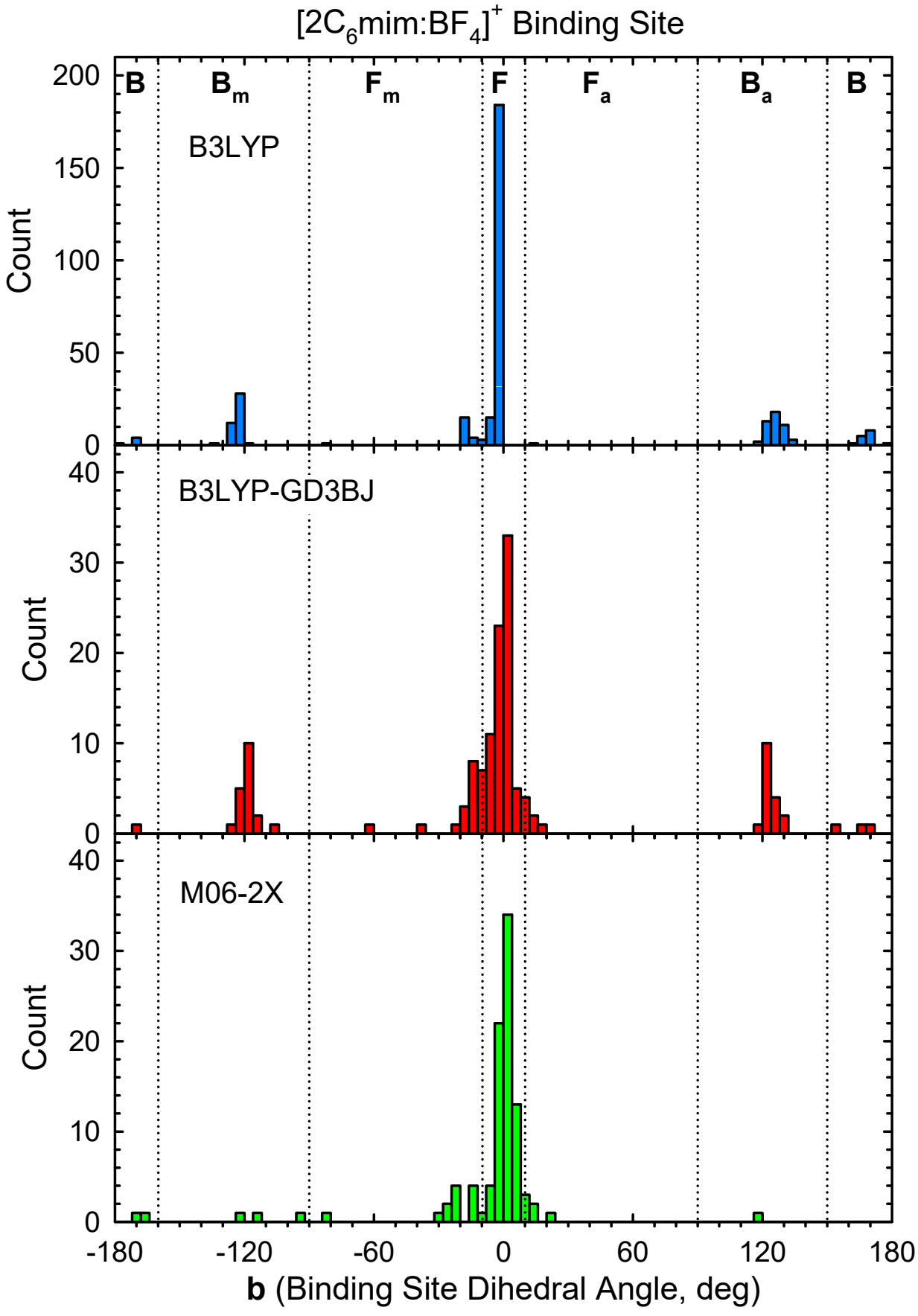
[2C6mim:BF4]+ Binding Site
B
Bm
Fm
F
Fa
Ba
B
B3LYP
B3LYP-GD3BJ
M06-2X
Count
200
150
100
50
0
40
30
20
10
-180
-120
-60
0
60
120
180
b (Binding Site Dihedral Angle, deg)

Figure S36.

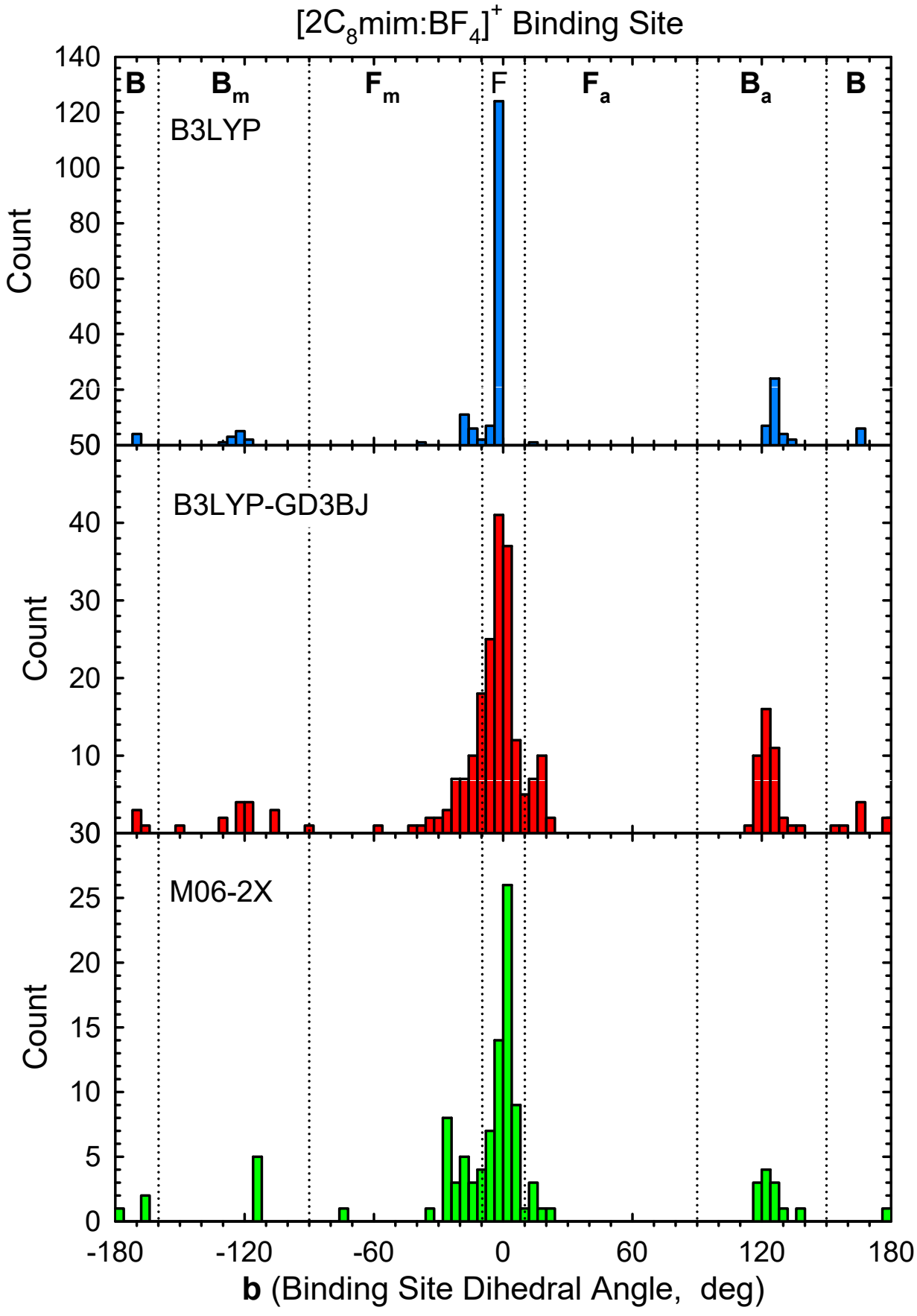
[2C8mim:BF4]+ Binding Site
B
Bm
Fm
F
Fa
Ba
B
B3LYP
B3LYP-GD3BJ
M06-2X
Count
Count
Count
140
120
100
80
60
40
20
50
40
30
20
10
30
25
20
15
10
5
0
-180
-120
-60
0
60
120
180
b (Binding Site Dihedral Angle, deg)

Figure S37.

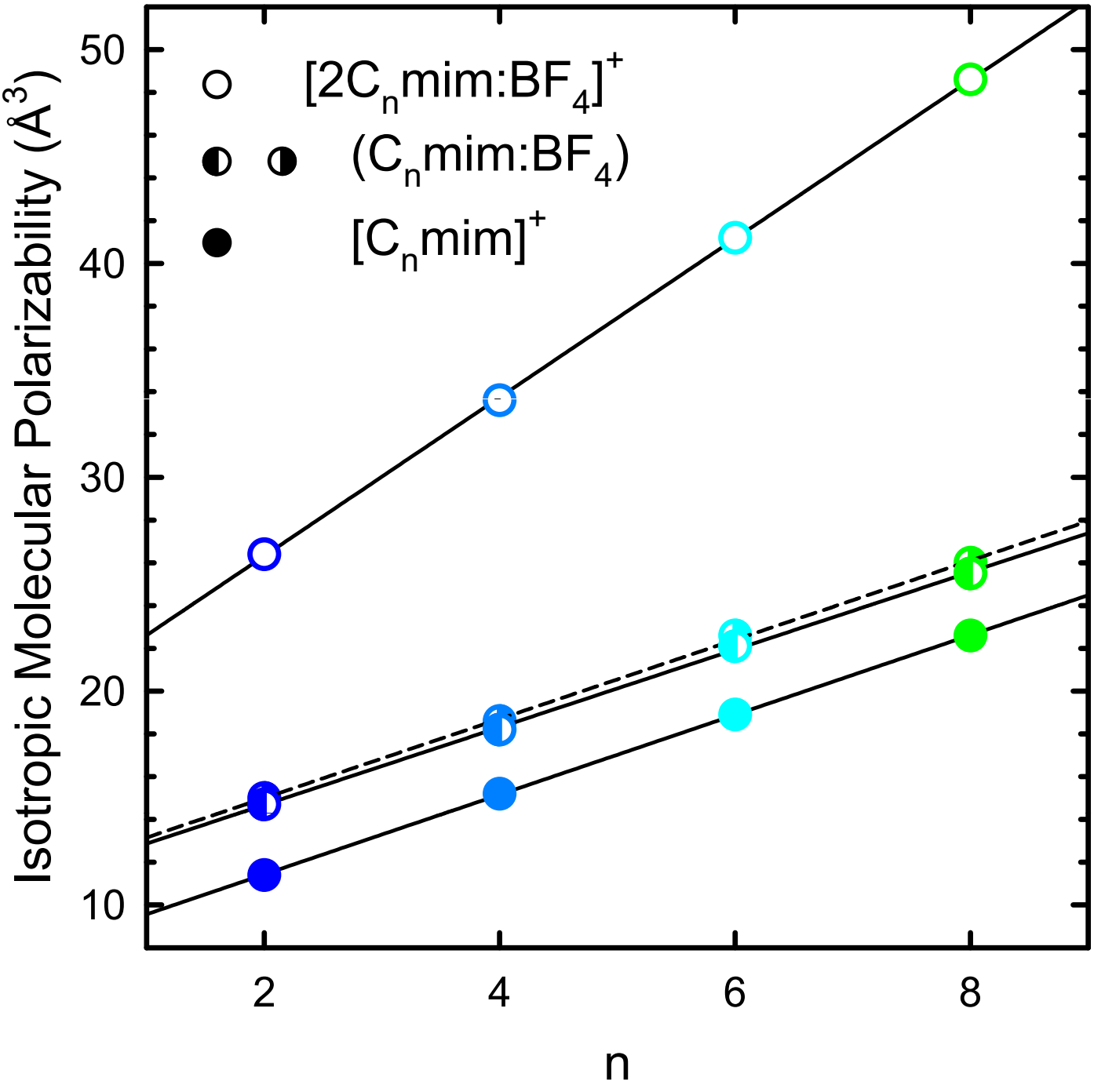
Isotropic Molecular Polarizability (Å^3)
n
$[2C_nmim:BF_4]^+$
$(C_nmim:BF_4)$
$[C_nmim]^+$
10
20
30
40
50
2
4
6
8

Figure S38.

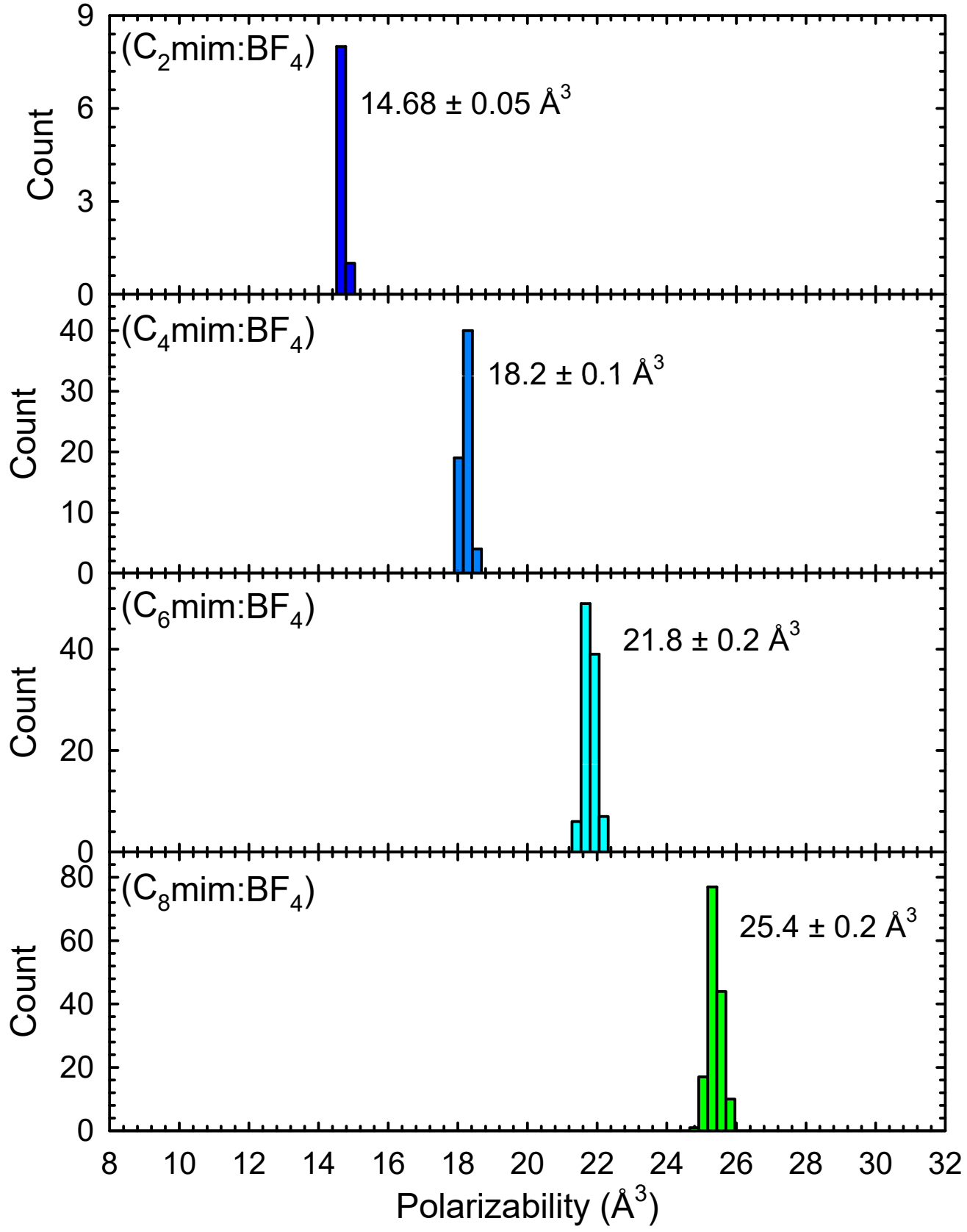
(C2mim:BF4)
14.68 ± 0.05 Å3
(C4mim:BF4)
18.2 ± 0.1 Å3
(C6mim:BF4)
21.8 ± 0.2 Å3
(C8mim:BF4)
25.4 ± 0.2 Å3
Count
Polarizability (Å3)

Figure S39.

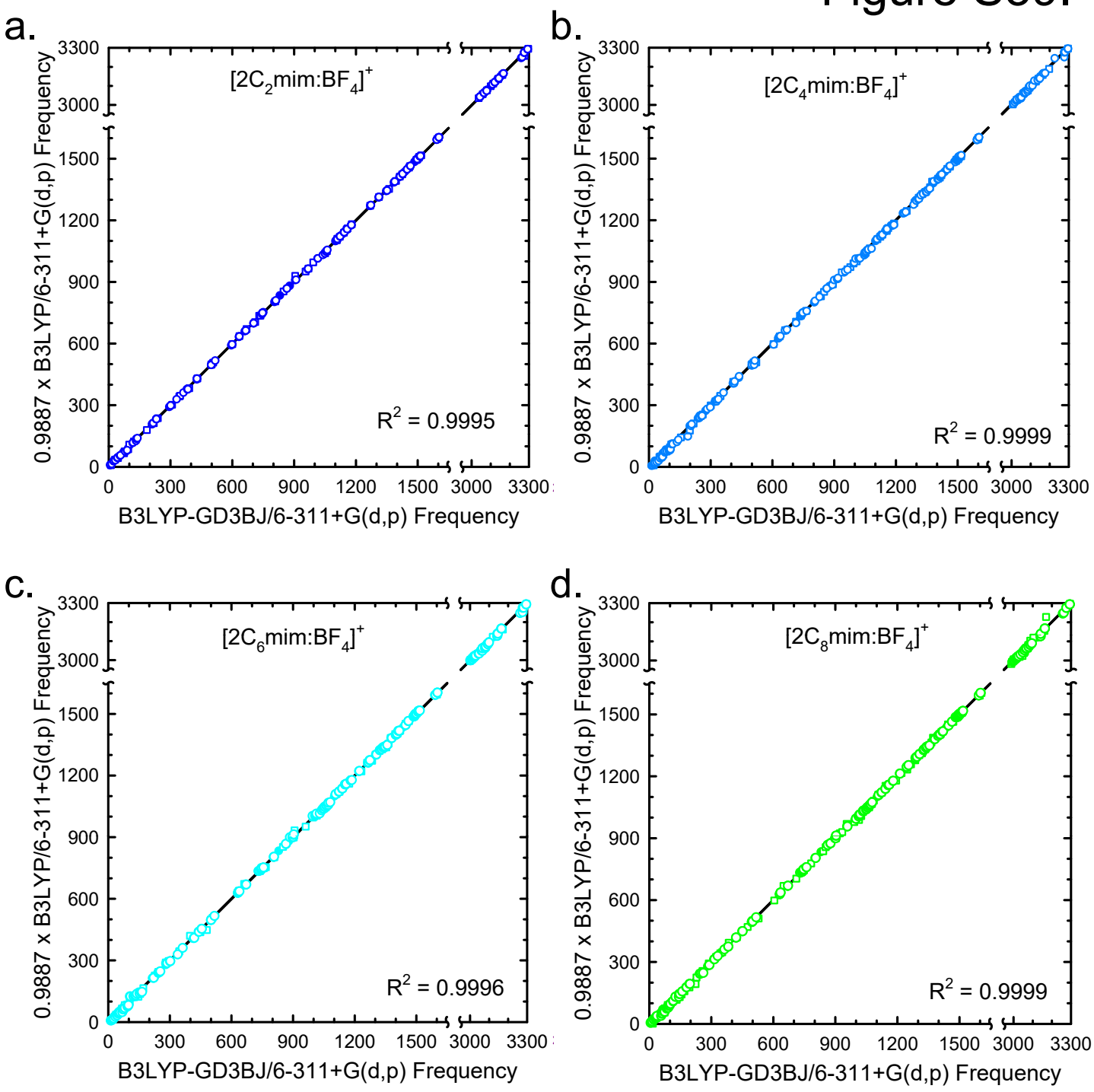
a.
[2C2mim:BF4]+
R2 = 0.9995
b.
[2C4mim:BF4]+
R2 = 0.9999
c.
[2C6mim:BF4]+
R2 = 0.9996
d.
[2C8mim:BF4]+
R2 = 0.9999
0.9887 x B3LYP/6-311+G(d,p) Frequency
B3LYP-GD3BJ/6-311+G(d,p) Frequency
0
300
600
900
1200
1500
3000
3300

Figure S40.

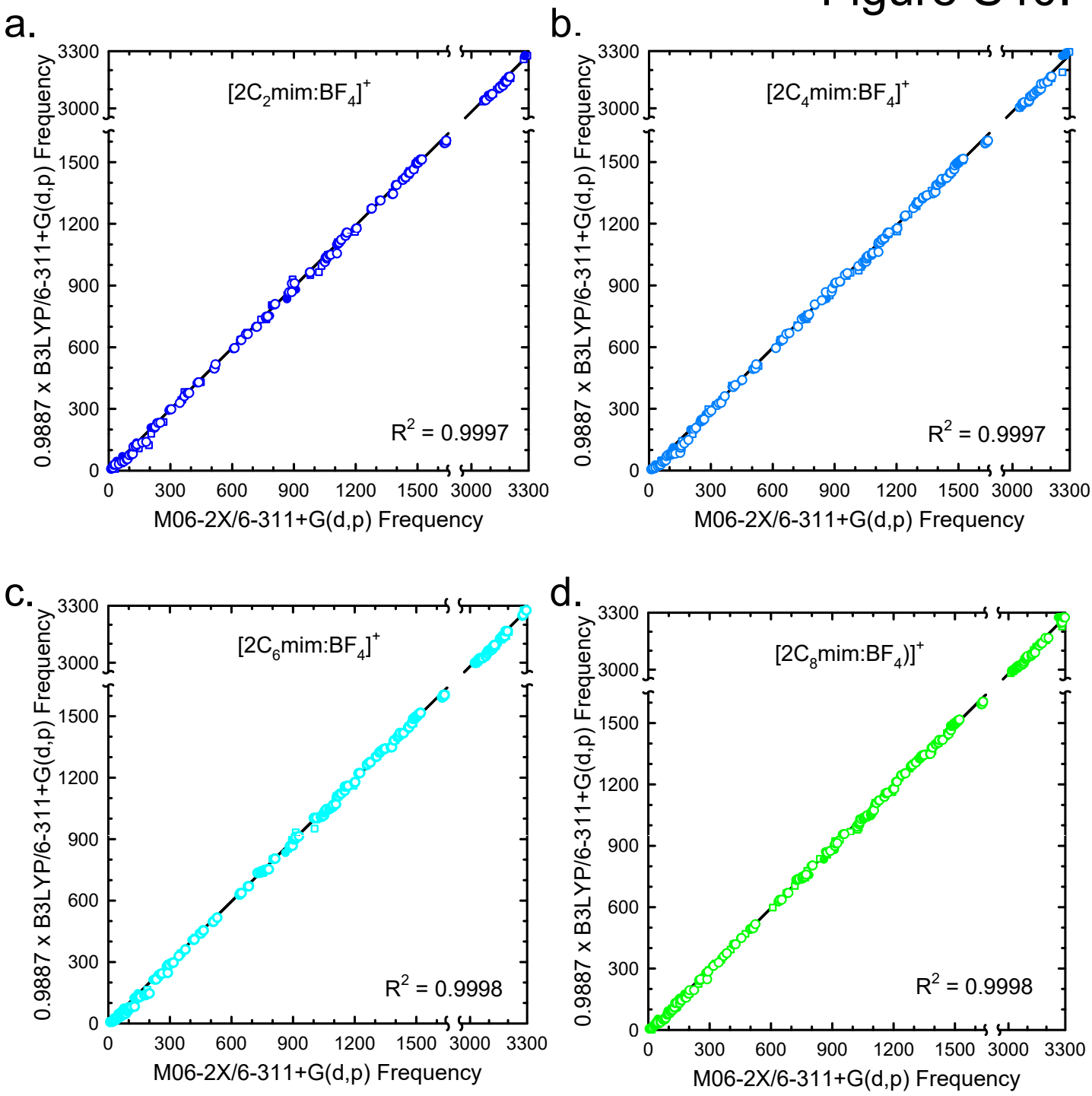
a.
[2C2mim:BF4]+
R2 = 0.9997
b.
[2C4mim:BF4]+
R2 = 0.9997
c.
[2C6mim:BF4]+
R2 = 0.9998
d.
[2C8mim:BF4)]+
R2 = 0.9998
0.9887 x B3LYP/6-311+G(d,p) Frequency
M06-2X/6-311+G(d,p) Frequency
0
300
600
900
1200
1500
3000
3300

Figure S41.

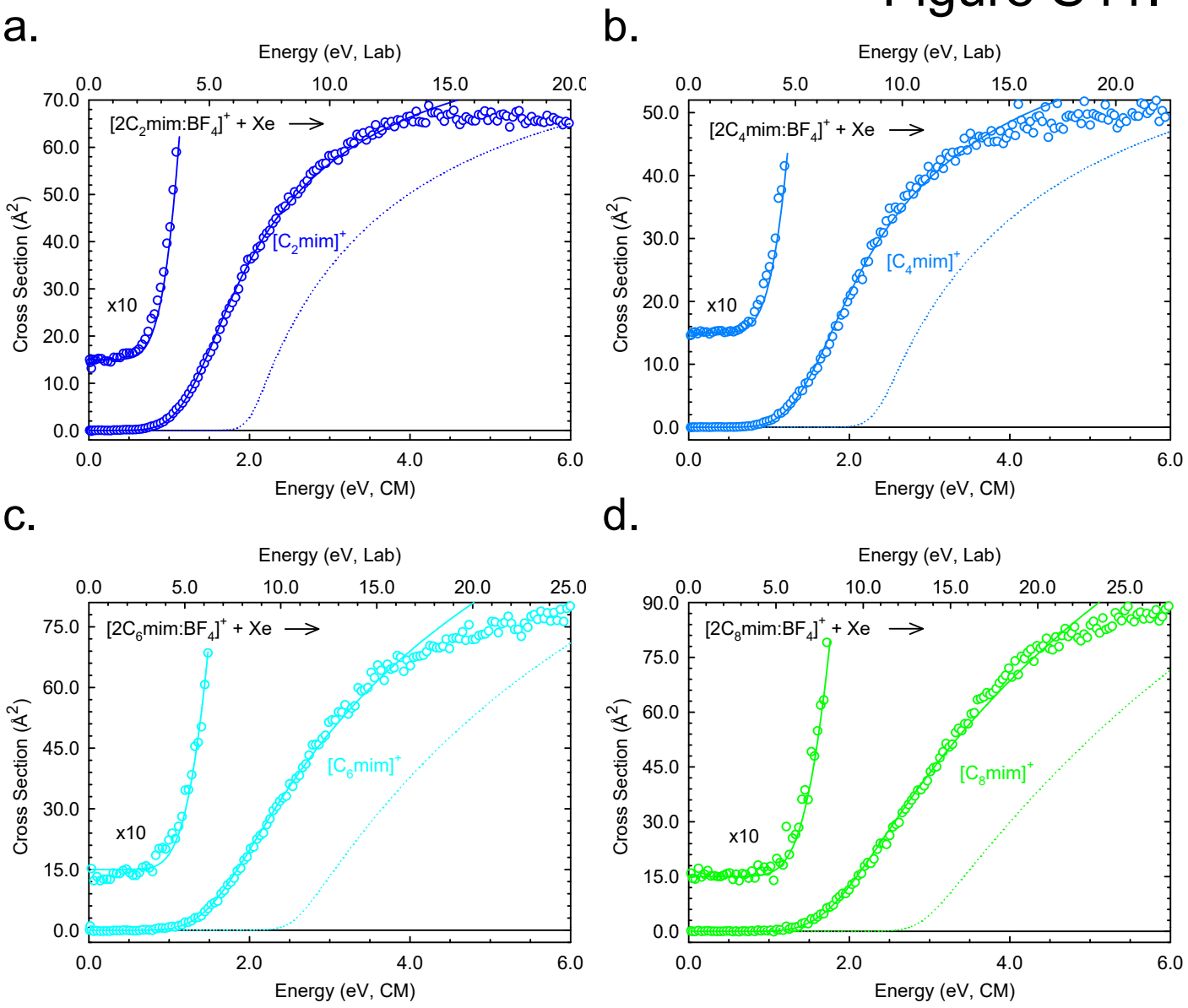
a.
Energy (eV, Lab)
[2C2mim:BF4]+ + Xe
[C2mim]+
x10
Cross Section (Å2)
Energy (eV, CM)
b.
Energy (eV, Lab)
[2C4mim:BF4]+ + Xe
[C4mim]+
x10
Cross Section (Å2)
Energy (eV, CM)
c.
Energy (eV, Lab)
[2C6mim:BF4]+ + Xe
[C6mim]+
x10
Cross Section (Å2)
Energy (eV, CM)
d.
Energy (eV, Lab)
[2C8mim:BF4]+ + Xe
[C8mim]+
x10
Cross Section (Å2)
Energy (eV, CM)

Figure S42.

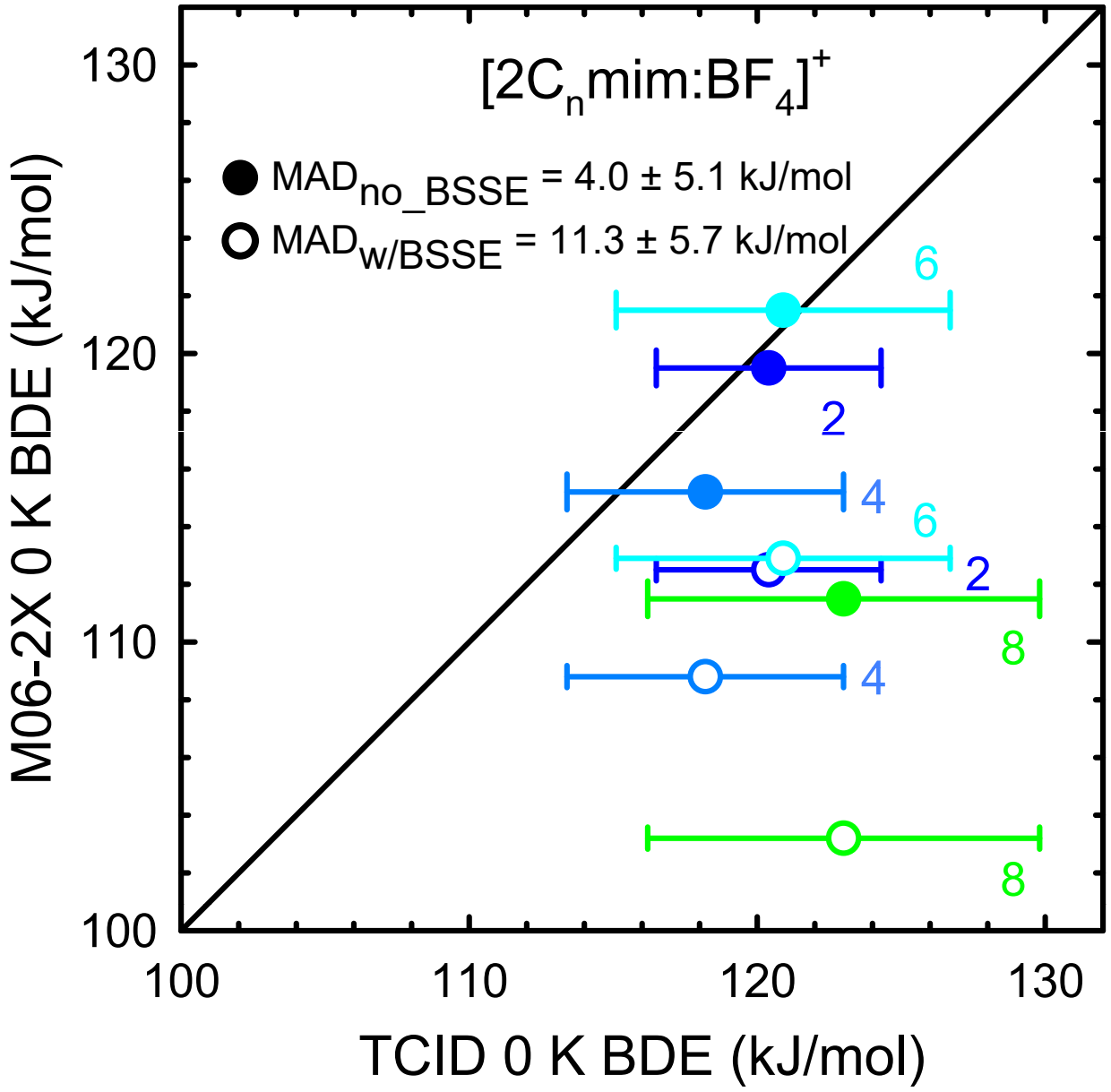
[2C$_n$mim:BF$_4$]$^+$
MAD$_{no_BSSE}$ = 4.0 ± 5.1 kJ/mol
MAD$_{w/BSSE}$ = 11.3 ± 5.7 kJ/mol
6
2
4
6
2
8
4
8
M06-2X 0 K BDE (kJ/mol)
TCID 0 K BDE (kJ/mol)
100
110
120
130

Figure S43.

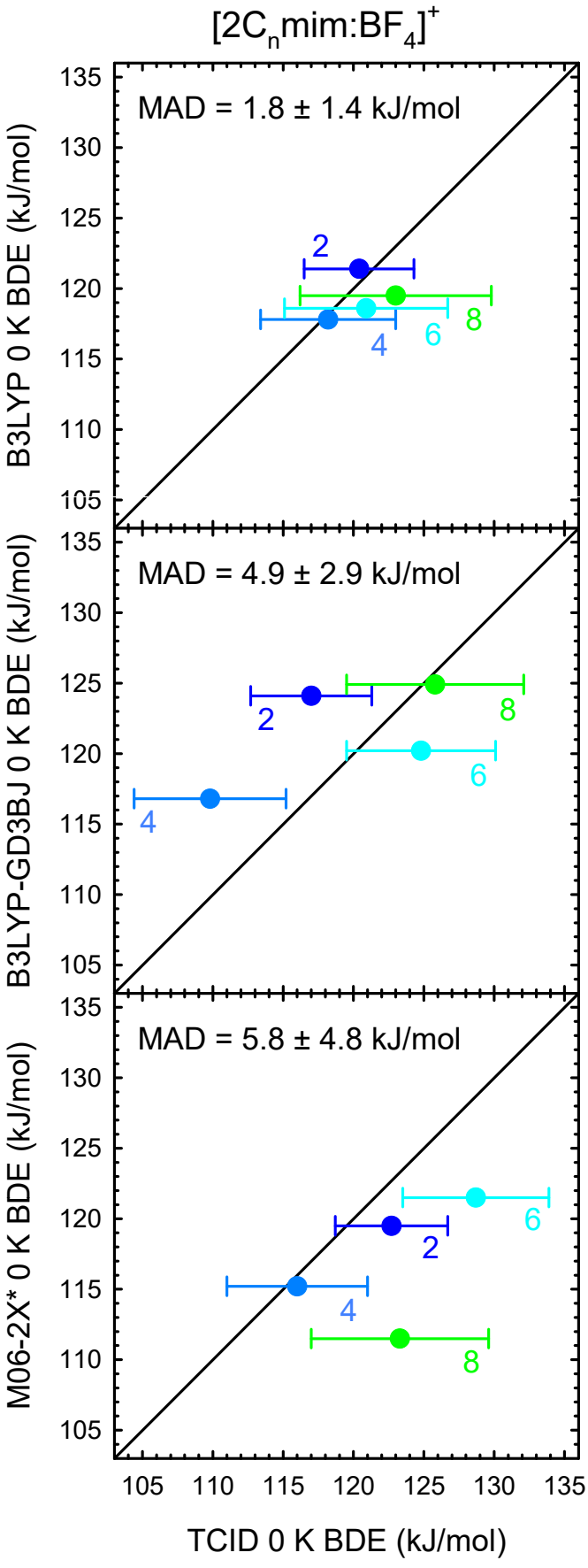
[2C$_n$mim:BF$_4$]$^+$
MAD = 1.8 ± 1.4 kJ/mol
MAD = 4.9 ± 2.9 kJ/mol
MAD = 5.8 ± 4.8 kJ/mol
B3LYP 0 K BDE (kJ/mol)
B3LYP-GD3BJ 0 K BDE (kJ/mol)
M06-2X* 0 K BDE (kJ/mol)
TCID 0 K BDE (kJ/mol)
105
110
115
120
125
130
135
2
4
6
8